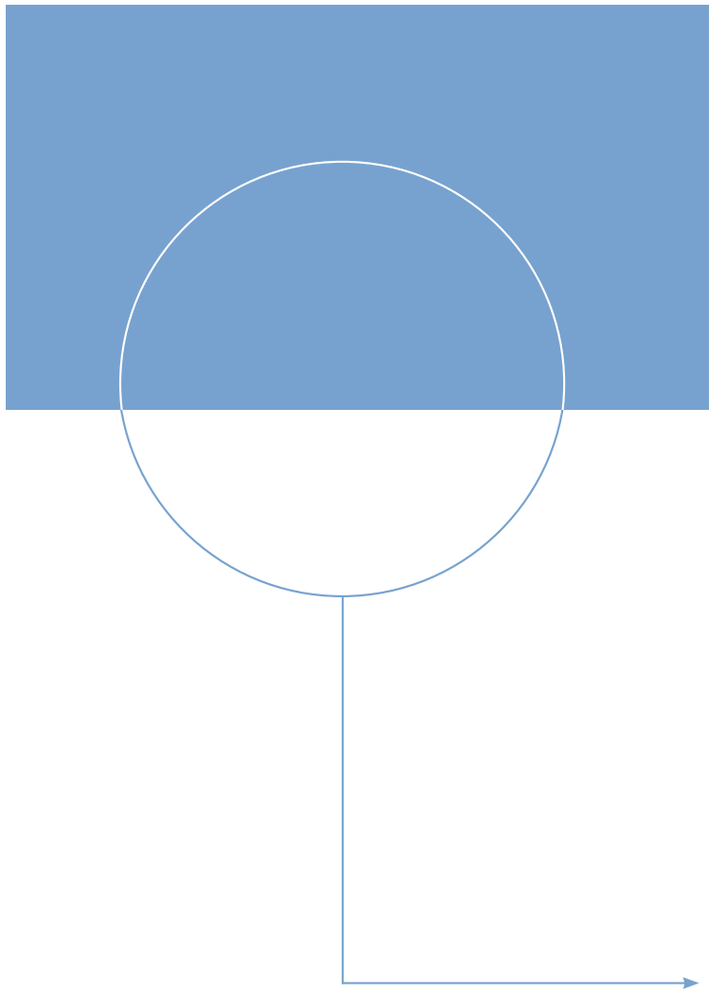

Master's thesis

2020

Anna Teetzmann

NTNU
Norwegian University of
Science and Technology
Faculty of Engineering
Department of Civil and Environmental Engineering

Anna Teetzmann

Influence of earth pressure coefficients on numerical simulations in RAMMS

June 2020

NTNU
Norwegian University of
Science and Technology

NTNU
Norwegian University of
Science and Technology

NTNU
Norwegian University of
Science and Technology

Influence of earth pressure coefficients on numerical simulations in RAMMS

Anna Teetzmann

Civil and Environmental Engineering
Submission date: June 2020
Supervisor: Rao Martand Singh
Co-supervisor: Hervé Vicari

Norwegian University of Science and Technology
Department of Civil and Environmental Engineering

Abstract

This thesis contains investigations of the effects of earth pressure coefficients in numerical simulations of debris flows. Debris flows consist of a mixture of soil, water and rock and can have several initiation causes. The debris flows can either have a dilatant or compressive behavior which is defined from the velocity gradient in the different phases of a flow. Depending on if a flow is dilating or compressing, an active or passive earth pressure coefficient is defined. The behavior can also be change in different directions and at different locations in the flow. This causes the behavior of the flow to be associated with different earth pressure coefficients in different directions at different locations and points in time. These earth pressure coefficients are included in the moment balance of a debris flow and can hence adjust the behavior in different phases of the flow.

Debris flows pose a significant threat to humans and infrastructure since their large velocities and forces combined with long runout distances can result in large destructions. In addition, the debris flows are hard to predict. It is therefore important to obtain good methods to realistically simulate such flows. By using numerical simulations that represent the event well, one makes it possible to design good countermeasures and in such a way help to protect both people and structures.

The effect of the earth pressure coefficient is investigated by modelling a debris flow in the numerical software RAMMS. The program has a separate module for debris flows. The program considers the debris flow as one material which moves as a continuum. Based on the properties of the debris flow, a rheology that defines the flow must be determined. RAMMS uses the Voellmy rheology which defines basal friction based on the parameters μ and ξ. They define a dry-Coulomb type of friction and turbulent friction respectively. The program also lets the user define an earth pressure coefficient during the simulation of a debris flow. This coefficient can either be set to an active or passive value and remains constant throughout a simulation in all phases of the flow. With a release volume from a given height and a terrain model which defines the flow path of the debris flow, RAMMS determines the course of the debris flow based on mass and momentum equations. The results show as an animation which contains information about the debris flow height and velocity at different locations. Based on these results, the effect of the earth pressure coefficient can be scrutinized.

The shape and length of runout is to a large extent affected by the earth pressure coefficients. The effect changes based on if the earth pressure is active or passive. The different earth pressure coefficients are in reality determined as a result of the velocity gradients, RAMMS however only lets the user set a constant value of the coefficient for the entire simulation. Both the active and the passive earth pressure coefficient affected the shape and length of the runout. The active earth pressure coefficient showed to have a controlling effect of the spread of the flow to some extent. Unfortunately, this coefficient results also in oscillations in the simulation results. The passive one showed to have an elongating effect on the flow. The most ideal situation would nevertheless be to be able to variate the earth pressure coefficient based on the gradient of velocity, to simulate best simulate the behavior of the debris flow. This is however not possible in RAMMS.

Sammendrag

Denne oppgaven innebærer undersøkelser av effekten som jordtrykkskoeffisienter har i numeriske modelleringer av flomskred. Flomskredene består av en blanding av jord, vann og stein og kan oppstå av ulike årsaker. Flomskred har en dilatant eller kontraktant oppførsel som defineres ut ifra hastighetsgradienten i ulike faser av et skred. Avhengig av om skredet dilaterer eller blir kompaktert, defineres henholdsvis en aktiv eller passiv jordtrykkskoeffisient. Oppførselen kan også være forskjellig i ulike retninger og i ulike deler av skredet. Dette medfører at oppførsel av et flomskred som kan assosieres med ulike jordtrykkskoeffisienter i ulike retninger ved ulike steder og tidspunkt. Disse jordtrykkskoeffisientene påvirker skredenes momentbalanse og kan dermed justere oppførselen i ulike faser av skredet.

Flomskred utgjør en betydelig risiko for mennesker og infrastruktur da dets store hastigheter og krefter kombinert med lange utløp kan resultere i omfattende ødeleggelser. I tillegg er denne skredhendelsen vanskelig å forutse. Derfor er det også viktig å finne gode metoder for å simulere disse skredene på en realistisk måte. Ved hjelp av numeriske simuleringer som godt illustrerer et flomskreds forløp, muliggjør man i større grad å kunne dimensjonere sikkerhetstiltak og dermed sikre både mennesker og materiell.

Effekten av jordtrykkskoeffisienten er undersøkt ved hjelp av det numeriske modelleringsprogrammet RAMMS. Dette programmet har en egen modul for flomskred. Programmet anser flomskredet som et materiale som beveger seg som et kontinuum. Derfor må det basert på flomskredets egenskaper, defineres en reologi som definerer strømmen av flomskredet. RAMMS bruker en Voellmy-reologi som definerer basal motstand basert på de to friksjonsparameterne μ og ξ, som henholdsvis definerer en tørr-Coulomb type friksjon og turbulent friksjon. Programmet lar en definere en jordtrykkskoeffisient under simuleringene av et flomskred. Denne kan enten settes aktiv eller passiv og forblir konstant gjennom hele simuleringen i alle faser av flomskredet. Med utslippsvolum fra en gitt utslippshøyde og en terrengmodell som definerer utløpssonen for flomskredet, beregner RAMMS forløpet av skredet basert på ligninger for masse og moment. Resultatet vises i en animasjon som inneholder informasjon om flomskredets høyde og hastighet ved ulike lokasjoner. Ut ifra resultatene kan effekten av jordtrykkskoeffisienten undersøkes.

Utløpsformen og lengden påvirkes i stor grad av jordtrykkskoeffisientene. Effekten er ulik avhengig av verdien er aktiv eller passiv. De ulike jordtrykkskoeffisientene skal egentlig bestemmes som et resultat av hastighetsgradienten, men RAMMS lar kun brukeren bestemme en konstant verdi for hele simuleringen. Både den aktive og den passive jordtrykkskoeffisienten gav utslag på formen til flomskredet. Den aktive jordtrykkskoeffisienten viste seg å ha en viss kontrollerende effekt av spredningen på flomskredet. Dessverre viser det seg samtidig at denne koeffisienten resulterer i oscilleringer av simuleringen. Den passive viste seg å ha en forlengende effekt på skredet. Det mest optimale hadde likevel vært å kunne variere jordtrykkskoeffisientene basert på hastighetsgradienten for å best mulig simulere oppførselen av denne typen skred, men dette lar seg ikke gjøre i RAMMS.

Forord

This thesis is written through the course TBA 4900 – Geotechnical engineering – Master's thesis at the in the study program of Civil and Environmental Engineering at NTNU. The thesis consists of investigating the effects of earth pressure coefficients on numerical modelling of debris flows in RAMMS. The thesis originally started out as a thesis concerning the physical modelling of debris flows with the use of an intermediate barrier. However, through the special events of the Covid-19 crisis from March 2020, the lab and school were closed, and it was hence not possible to go through with this objective. I still hope that some of the work conducted on the intermediate barrier can become useful in future experiments, and the work is hence presented. Due to this lock down, the thesis was rearranged to concern the effect of the earth pressure coefficient in numerical modelling, which has become the resulting thesis presented. The physical model in its entirety is still given as it is used for the basis for developing the numerical model.

First, I would like to thank Hervé Vicari who has provided continuous supervision of my work and invested valuable time in discussions and comments throughout this thesis. Further I would like to thank Professor Vikas Thakur and Professor Rao Martand Singh for their help in leading me in the right direction and for supervision through some challenging times. Thank you also to Professor Steinar Nordal for help with establishing contact with some of the right people. I also want to thank the lab technicians both who have helped me in first two months with developing the model to do the physical experiments, although we were not able to use it. Last, I want to thank my friends and family who have provided encouragement and support throughout this process.

Trondheim, 2020-09-06

Anna Teetzmann

Innhold

List of figures

List of tables

Abbreviations

DEM	Digital elevation model
DAN3D	Dynamic ANalysis of landslides in three dimensions
NTNU	Norges Teknisk-Naturvitenskapelige Universitet
RAMMS	Rapid Mass Movement System
SLF	Institut für Schnee und Lavinenforschung
WSL	Forschungsanstalt für Schnee und Landschaft

List of symbols

α – slope angle

α_c – centrifugal acceleration

β – angle of debris hitting bed after overflow of barrier

γ – unit weight

γ_d – unit weight of debris

γ_w – unit weight of water

$\dot{\gamma}$ – shear rate

δ – grain diameter

δ_1 – bed friction angle

θ – slope angle

θ_d – deposition angle

$\theta_d - \theta$ – net deposition angle

K – Hydraulic conductivity

κ – Hydraulic permeability

λ – earth pressure coefficient

λ_{act} – active earth pressure coefficient

λ_{pas} – passive earth pressure coefficient

μ – dry friction coefficient

μ_v – viscosity

ξ – turbulent friction coefficient

ρ – flow density

ρ_f – fluid density

ρ_s – solid density

σ – normal stress

σ' - effective stress

τ – Coulomb shear stress

φ – friction angle

φ_a – apparent friction angle

ϕ_g – solid grain friction angle

A_i – base area of boundary block

B_i – width of base of boundary block

C – solid concentration

C_x – correction factor of horizontal length

c – steady state undrained shear strength or cohesion

c_x, c_y – velocity shape profile

d_s – length of base of boundary block

E – compressive stiffness

e – restitution coefficient

F – centrifugal force

Fr – Froude number

f – centrifugal acceleration

g – gravitational acceleration

H, h - flow height

H_i – height of boundary block

h_0 – free field thickness

h_d – height of retained material

$\boldsymbol{K}$ – terrain curvature matrix

K – earth pressure coefficient

K_a, k_a - active earth pressure coefficient

KE_r – kinetic energy of remaining debris

K_p, k_p - passive earth pressure coefficient

L – length of flow

L_T – run-up distance behind barrier

m_r – mass of remaining debris after barrier

N – normal force

N_0 – yield stres

N_g – number of grains

N_{Bag} – Bagnold number

N_{Dar} – Darcy number

N_{fric} – friction number

N_{mass} – mass number

N_{Rey} – Reynolds number

N_{Sav} – Savage number

$\dot{Q}$ – mass production

R – correction factor

R_d – attenuation factor

S – basal shear resistance

S_f – frictional acceleration

S_g – gravitational acceleration

T – basal resistance

T_c – particle collision shear stress

$T_{f(i)}$ –fluid inertial stress

$T_{f(q)}$ – quasi-static fluid stress

T_{s-f} – solid fluid interaction stress

$T_{s(i)}$ – solid inertial stress

$T_{sq}, T_{s(q)}$ – quasi-static Coulomb friction stress

T_t – turbulent mixing stress

U – velocity vector

u – pore pressure

V_s – solid volume fraction

V_f - fluid volume fraction

v_f – velocity of fluids

v_i – velocity after impact

v_m – horizontal velocity at barrier crest

v_r – impact velocity

v_s – velocity of solids

x_i – horizontal trajectory path

z – depth of unstable material

z_d – debris flow thickness

1 Introduction

Debris flows consist of a mixture of water, rock and soil (Iverson, 1997b). The initiation of such a flow can happen as a consequence of slope failure (Iverson, 1997b). The process of initiation can occur due to a number of events such as landslides, short and heavy rainfalls or water runoff from collovium and bedrock (Coe et al., 2008; Hungr et al., 2014; Meyer & Wells, 1997). The flows occur when poorly sorted sediment, saturated with water is set into movement and starts to surge down a flowpath such as a hillside (Iverson, 1997b). The motion of such flows is influenced by the solid and fluid forces, distinguishing it from other similar phenomena (Iverson, 1997b).

Debris flows are a phenomenon that can happen with little warning. They pose a significant hazard through their combination of high velocity, impact forces, long runout distances and difficulty in predicting the phenomenon. Their highly destructive power is a result of the interaction of solid and fluid forces in such flows (Iverson, 1997b).

The events are highly gravity driven and can hence increase their hazard while travelling down the flow path. The debris flows are able to entrain material along their paths (Hungr et al., 2014). This way the debris flows can increase their volume and hence their destructive power (McDougall & Hungr, 2005).

With the increased climate changes, enhanced percipitation and flood water exposure, debris flows have become more frequent events. Therfore it is a vital factor for the environment to study how one can reduce effects on society due to the actions of a debris flow. The difficulty to prevent the event itself, makes it important to understand the phenomenon and to be able to counteract its hazardous impacts. Different measures such as the use of rigid intermediate barriers, deflection dams and nets (Takahashi, 2007, p. 336; Wendeler, 2016) are proposed to counteract either the further advancement of a flow by reducing the possible impact forces as material is detained, or hindering a large impact force in hitting a weaker structure.

Tools such as numerical softwares hence become important for investigating the forces acting in a flow and how the debris flow will develop and behave. Numerical tools can e.g. be used to predict debris flow runouts, velocities and flow heights. By using these outputs, assumptions and estimations can be made on their desctructive potential. The softwares however still struggle to predict the natural event in its entirety as debris flows have both highly variable properties and behavior. The challenge then becomes to simulate the right behavior to the right stage of the flow.

The western part of Norway is prone to steep terrain and high degree of percipitation. Considering the NVE hazard map (NVE, n.d.) for these costal areas, it can be obtained that the density of possible debris flow exposed areas is quite large. Both the topography and the geology, as well as the climate facilitate the region for hazard of this event. The assessment of the destructive power of the debris flows, is therefore a matter of interest when wanting to devlop new infrastructure in such areas. This is therefore a motivation to assess a debris flow motion more accurately through numerical simulations, as it will provide a better tool to predict the hazards and damages it poses. More accurate numerical simulations could give aid in designing potenital countermeasures to prevent accidents and securing infrastructure.

Problem formulation

The objective of this thesis concerns the understanding of the influence of the earth pressure coefficients on the numerical simulations performed in the software RAMMS. The basis of the simulations is an already existing physical model used in previous experiments of small-scale debris flows. Through establishing a terrain model based on the previous physical model, the effect of the earth pressure coefficient on flow properties such as flow height, velocity and runout is wanted to scrutinize.

Structure of the thesis

Section 2 of this thesis concerns a literature study on the debris flow phenomena. Some general definitions, common properties and frameworks are defined. Further on the basics of barrier design and theory of earth pressure coefficients are presented before the numerical models and state of the art experiments are given. Section 3 and 4 contain the description of the physical and numerical model and the general experimental setup both for the numerical simulations and the physical experiments. Section 5 presents the results of the numerical simulations performed based on flow heights, velocity and runout. Section 6 discusses the results presented in Section 5 and makes explanations for the experienced behavior for the different flow properties and dynamics. Some general theoretical concepts are revisited here. Lastly, Section 7 gives conclusions based on the results obtained in this thesis compared to the problem formulation given in the introduction. The Appendix (Section 8) contains additional figures on the simulation results which are of importance to this thesis.

2 Literature

This section discusses some of the general theory concerning debris flows and physical and numerical modelling of the phenomena. First the debris flow event and its hazards are described, giving definition from literature and how to classify a debris flow in some well-known classification schemes. Further the details on stresses and mechanisms occurring in a flow are discussed involving which stresses that are defined in such a flow and what can be common properties. The event of basal erosion is also visited. Debris flow barriers are presented as a countermeasure to debris flows and some design principles are described in the following. Further the details of numerical modelling are described. Two different main categories of numerical models are visited: the lumped mass models and the continuum mechanical models. The numerical software is also discussed. In a numerical simulation, one can change the earth pressure coefficients, to take account for effects that happen for the real phenomena. The effect of earth pressure coefficients in a debris flow is discussed and some approaches on the use of these is established. Finally, this section concerns some earlier experiments that have been performed. These give relevant information on the simulations of this thesis.

2.1 General on debris flows

In general, debris flows are gravity driven and contain a mixture of coarse material, such as rocks, granular soils and water (Iverson, 1997b). Takahashi (2007, p. 6) described the debris flows as a mix of mud, water and debris, where the particles are dispersed in a slurry. The debris flows can be described by a heterogenous fluid that is formed by water and solids, and where there is no distinct separation of the phases (Davies, 1990). Hungr et al. (2014) defines the unsorted and mixed debris material as having low plasticity, and distinguishes between dry, saturated and partly saturated debris. The flowing mixture is irreversibly deformed and can thereafter flow with a free surface (Iverson, 1997b).

Debris flows are common in steep terrain, and the flow travels along distinct, pre-established paths (Hungr et al., 2014). The initiation of such a flow can be due to several reasons. There may be an initiating slide that causes the flow, but also avalanches, rock fall or sudden loss of stability in a stream bed can induce such an event (Hungr et al., 2014). One often states that debris flows are rainfall induced, and Hungr et al. (2014) supports this by stating that the flows often happen at the same time as flooding in an area. Snow- and ice-melting can give the same effects, the same yields for the event of a dam break or lake outbursts. This indicates that the debris flows can also happen during a period of good weather, which can e.g. induce melting of ice and snow. The initiation can also be described as a liquefaction of the deposits of sediment due to the occurrence of a mass movement (Iverson, 1997b).

The definition by Takahashi (2007, p. 6) focuses on the interaction between sediment and water in the flow:

> *"Debris flow is a flow of sediment and water mixture in a manner as if it was a flow of continuous fluid driven by gravity, and it attains large mobility from the enlarged void space saturated with water or slurry."*

According to Hungr et al. (2014, p. 183), the debris flows are defined as follows:

"Very rapid to extremely rapid surging flow of saturated debris in a steep channel. Strong entrainment of material and water from the flow path."

These definitions clearly indicate the rapidity of the event and that entrainment of debris and water along the flow path affects the phenomena.

Several areas in the world are prone to debris flows. The debris flows act as a danger to established communities and people. The damages of the flows are both environmental, such as loss of housing facilities, infrastructure and spills into nature of some kind, and human activity (Jakob & Hungr, 2005). Debris flows can, if they are large, exceed a total volume of $10^9\ m^3$ and have a release of potential energy of larger than $10^{16}\ J$ (Iverson, 1997b). There is a need to build enough understanding for predicting and preventing of the threat that a debris flows poses, to be able to deal with this hazardous event. The interaction of solid and fluid forces in a debris flow, results them in having a high destructive power (Iverson, 1997b). The hazard of the phenomena is a result of a combination of velocity, impact forces, large runout distances and difficulty to predict the event (Jakob & Hungr, 2005). Debris flows can initiate with little warning (Iverson, 1997b). The debris flows are also prone to high mobility due to the effect of buoyancy on the flowing material (Takahashi, 2007, p. 6), vibrational kinetic energy of the solid grains and pore pressures (Iverson, 1997b), among others. Vibrational kinetic energy of the grains and pore pressure enable the debris flow in having a higher mobility, due to easing the motion of grains past each other (Iverson, 1997b).

2.2 Classification methods

There are several different approaches in classifying landslides. The most well-known classification approach was proposed by Varnes (Varnes, 1978) and modified by himself and Cruden in 1996 (Hungr et al., 2014). The slope movements classifications proposed are given in Table 1. There are five different types of slope movements defined: Fall, topple, slide, spread and flow. Also, three different types of material are given: rock, debris and earth. Cruden and Varnes (1996) suggested that any slope motion can be described by two nouns: the first one giving the type of material, and the second one giving the type of movement. Hence, debris flows are set together of the material type: debris, and the movement type: flow.

Table 1 The modified classifications of slope movements given by Varnes and Cruden (Cruden & Varnes, 1996).

	Type of Material		
Type of		Engineering Soils	
Movement	Bedrock	Predominantly Coarse	Predominantly Fine
Fall	Rock fall	Debris fall	Earth fall
Topple	Rock topple	Debris topple	Earth topple
Slide	Rock slide	Debris slide	Earth slide
Spread	Rock spread	Debris spread	Earth spread
Flow	Rock flow	Debris flow	Earth flow

In the well-known classification scheme of Cruden and Varnes (1996), the term debris flow allowed for different phases of different landslides to be classified as debris flows (Jakob & Hungr, 2005, p. 10). Their definition of debris material is that there should be a volume of gravel or coarser material larger than 20 %, but less than 80 % (Cruden & Varnes, 1996). Hungr et al. (2001) suggested a more distinct description of this material

with the aim of easing the application of the term. According to Hungr et al. (2001) debris is defined as a low plasticity material that is unsorted. The material occurs in an area as a product of different processes including e.g. weathering or human activity (Hungr et al., 2001).

A *flow* is a movement type that has a very short-lived shear surface which is often not preserved throughout the landslide (Cruden & Varnes, 1996). A schematic drawing of the movement can be seen in Figure 1. Flows can be rapid to extremely rapid movements (Cruden & Varnes, 1996; Hungr et al., 2014) as they have a high mobility and move down steep slopes. Extremely rapid movement has a lower velocity boundary of 5 m/s as its typical velocity (Cruden & Varnes, 1996; Hungr et al., 2014). As the flow travels downslope as something similar to a liquid, it gains speed (Cruden & Varnes, 1996).

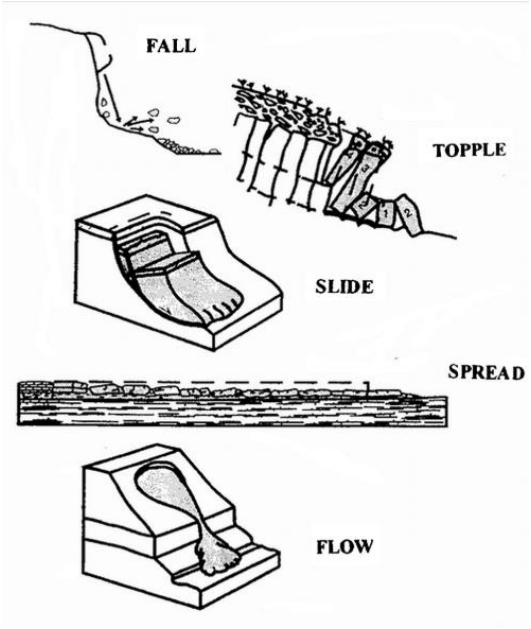

Figure 1 The different types of movements of a landslide (Cruden & Varnes, 1996).

According to the classification scheme in Hungr et al. (2001), debris flows are defined as extremely rapid events consisting of saturated debris, travelling through an already established channel. Debris flows are possible reoccurring events as opposed to debris avalanches of the same material type (Hungr et al., 2001). What separates them from the debris avalanches is mainly that the avalanches lack the confinement in a channel (Jakob & Hungr, 2005, p. 15). Debris floods on the other hand can also, like the debris flows, flow in a channel, but these floods consist of a flow of water that surges downhill, heavily charged with debris (Jakob & Hungr, 2005, p. 15). It is important to be able to distinguish between the different types of events, to be able to provide good prevention measures.

Pierson and Costa (1987) also did classification work based on the rheology of a flow and fitting this with existing nomenclature. This method of classification is discussed through rheology used in numerical modelling in section 2.5.3.

2.3 Debris flow mechanisms and mechanics

2.3.1 Event development

Iverson (1997b) states that the debris flows typically originate from close to rigid sediment masses. According to Jakob & Hungr (2005, p. 16), the debris flows may initiate spontaneously if there is a steep slope with a slope angle ranging from $20°$ to $45°$. Slopes that are flatter, may lack the potential energy to induce a spontaneous debris flow, and slopes that are steeper don't have sufficiently large enough layers of debris, to be able du induce a continuous sliding movement (Jakob & Hungr, 2005, p. 17). According to Iverson (1997b) debris flows can initiate from several reasons, e.g. as a result of melting snow and ice, undermining by abrupt floods and failure of the rigid sediment masses. The slope failure initiation process is the most dominating of the suggestions (Iverson, 1997b). To initiate the rigid masses into a flow, a few requirements need to apply almost simultaneously (Iverson, 1997b): first, the masses need to fail, either by a single slope failure or by several small consecutive failures. Second, there needs to be enough water content to saturate these masses. In most cases, this water already exist in the mass before failure (Iverson, 1997b). Third, enough potential energy must transform into kinetic energy, to go from smaller localized deformation to extensive deformations which are associated with a flow (Iverson, 1997b).

The restraints against the initiation movement comes from the contact friction between grains (Mitchell & Soga, 1994). In some cases, cohesion strength can also play an important role, but during failure it is adequate to set the cohesive strength to approximately zero (Skempton, 1964), this is because the bonds in the soils are broken. One could argue that the resistance against failure, could be described by the Coulomb criterion:

$$|\tau| = \sigma' * \tan(\phi) + c \qquad (2.1)$$

The Coulomb criterion also covers the fact of resistance due to the grain friction as mentioned before, through the bulk friction angle, ϕ. The effective normal stresses, σ', are given as the difference between the total stresses and the pore pressures. Also, Iverson (1997) states that there during failure occurs shear displacement, that causes the debris flow material to contract. This can in turn lead to liquefaction of the sediment mass (Ellen & Fleming, 1987). But the mass failure can also occur without the contraction if there is enough available energy to stir the mass that can fail (Iverson, 1997b).

Jakob and Hungr (2005, p. 17) describe that the initiated material, regardless of the mechanism inducing it, can continue downslope as a debris avalanche if it is not confined. Further, they describe that the avalanche can enter channels or gullies that are already established and hence form a debris flow. The middle part in the travelling of a debris avalanche is also called the transportation zone (Jakob & Hungr, 2005, p. 17). Entering of such a channel does not cause any reduction of velocity of the pre-existing slide. Iverson (1997b) describes that the debris flows occur as a surge of poorly sorted sediment, which is agitated and saturated with water and moves down a slope as an effect of gravity. The debris flows are different from other sediment prone water floods, due to the dual effect of both solid and fluid forces on the motion (Iverson, 1997b).

The initiated debris flow is travelling as is acting in surges (Iverson, 1997b). Davies (1990) states that assuming uniform flow for such an unsteady and pulsing phenomena

is highly inappropriate. The debris flows can consist of one single surge or many consecutive ones (Davies, 1990; Iverson, 1997b; Jakob & Hungr, 2005, p. 17). These surges of waves determine the hazard of the flow as they carry sediment which can cause large damages upon impact. Between the waves, the debris flow can cease entirely (Davies, 1990). The height and speed of the waves determines how large the damage might get (Davies, 1990). According to Iverson (1997b), measurements performed at the base of experimental debris flows, show a difference in the pore pressures of the surges, depending on the flows being coarse- grained or finer grained. Surge fronts in a coarse-grained flow show either little or no fluid pressure, while the finer grained ones is near to liquefied by such a pore fluid pressure (Iverson, 1997b). The head of the surge is what usually carries large sediments and items such as for example trees (Iverson, 1997b). Even though the coarse fronts have a high permeability, it seems like pore fluid does not come through the seemingly dry flow front (Iverson, 1997b).

Coarse material is moved to the flow front by two main mechanisms (Iverson, 1997b): incorporation of material as the flow moves downwards, and kinetic sieving, due to smaller grains moving through voids (Iverson, 1997b). Figure 2 shows a schematic drawing of how the surges are built up, with the coarse flow front and tail. As grains are agitated the ability of grains to move past each other increases (Iverson, 1997b). This agitation results in increased mobility of the debris flow. In addition, pore pressure will play a vital role in the mobility of debris flows. The mobility increases with increased pore fluid pressures, due to less resistance (Iverson, 1997b), which is also an effect covered by the Coulomb criterion in equation (2.1).

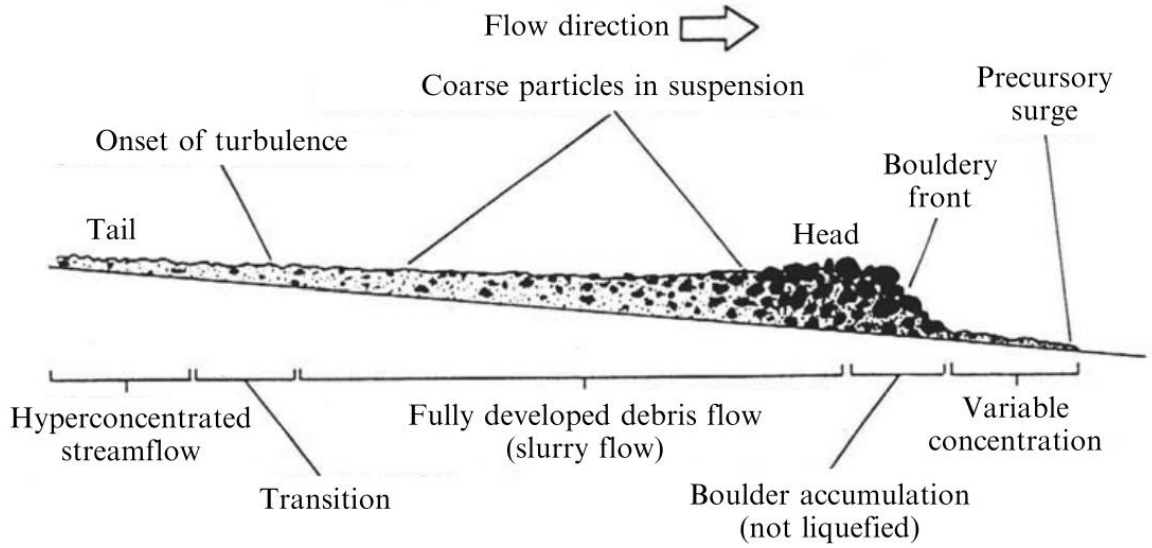

Figure 2 Debris flow surge with the coarse flow front and more fine-grained tail (Pierson, 1986).

The paths of the flow channel are often covered with loose material (McDougall & Hungr, 2005). According to McDougall & Hungr (2005), the momentum induced by the debris flow may cause this material to fail, hence resulting in the mass of the debris flow to increase. Jakob and Hungr (2005, p. 137) explain that debris creates a drag on the bed material, causing more material to be entrained than in a flow consisting of water only. As bed material is entrained, the debris flow develops a growing surge (Hungr et al., 2014). This surge will continue downstream in the slope, causing undermining of banks and further erosion of bed sediments, causing the surge to grow even bigger. This process of building surges is a result from sorting of the material along the longitudinal

axis (Jakob & Hungr, 2005, p. 137). When banks are undermined, there can happen a shallow landslide of the material going into the surge as an immediate response or there can be a delay, integrating the material in the next surge (Jakob & Hungr, 2005, p. 138). As the sediments are set into motion, the channel bed experiences undrained loading (Sassa, 1985). This happens relatively quickly, and as a result the bed material can liquefy, thereby enabling erosion of the channel bed (Hungr et al., 2014). The entrainment of material will have an effect on the bulk volume of the flow (Berger et al., 2011; Hungr et al., 2014), since a huge part of the material involved in a debris flow will come from the entrainment process (Jakob & Hungr, 2005, p. 135). This erosion effect, which causes the debris flow mass to increase, results in a debris flow being an even more hazardous phenomena compared to if the volume was constant. The hazard increase happens due to the influence that the entrained material has on the debris flow dynamics (Berger et al., 2011), as the initially small flow transforms into a larger one through the entrained material. Entrainment should therefore be considered when doing hazard assessments, as gravity affecting a larger mass results in greater forces exhibited by the flow.

The deposition process if debris flows can happen when all its energy has degraded to irrecoverable forms (Iverson, 1997b). The surges that are mentioned earlier, can grow as long as they are confined in a flow channel, but as soon as the confinement is lost, the flow will spread out (Hungr et al., 2014). The spread out debris will deposit in a fan on the runout surface (Hungr et al., 2014). Major (1997) stated through his experience with physical tests in a 95 meter long flume channel of 31°, that the sediments transported by surges are deposited as a progressive deposition, rather than the entire phenomena depositing *en masse*. The previously coarse flow fronts will in most cases determine the perimeter of the deposition area as they deposit quite quickly (Hungr et al., 2014; Iverson, 1997b). However, if the flow is more wet, the debris has higher mobility, and the tail of the flow can hence overflow some of the already deposited debris or breach the dam of deposited material (Iverson, 1997a). The more dilute material can in such a manner convert into debris flood surges. According to Iverson (1997b), the runout distance is positively influenced by debris flow entraining material due to the increased volume it causes.

2.3.2 Stresses in a debris flow

The vital interaction between fluid and solid forces in a debris flow, separates them from other similar phenomena (Iverson, 1997b). Different characteristics define a debris flow, due to both the fluid and solid contents. Among those are the sediment concentration, grain size distribution, flow front speeds, shear strengths and shear rates (Iverson, 1997b). According to Iverson (1997b), it is important to consider both the solid and fluid effects separately and their interactive effects. Wendeler (2016) describes that debris flows that consist mainly of rocks and blocks are considered as granular flows, while mudflows consist of finer material.

The differentiation between different types of flow, can be of a challenge. There are five different processes of building stresses in a flow (Iverson, 1997b; Takahashi, 2007, p. 24). These are presented through equations (2.2) to (2.6) below.

In a debris flow there are stresses occurring due to the interaction between the coarse particles. As particles collide, shear stresses are able to develop (Iverson, 1997b; Takahashi, 2007, p. 24). Iverson (1997b) describes these as solid inertial stresses:

$$T_{s(i)} \sim v_s \rho_s \dot{\gamma}^2 \delta^2 \quad (2.2)$$

Here v_s is the velocity of solids, ρ_s is the solid density, $\dot{\gamma} = \frac{v}{\delta}$, is the shear rate where δ is the grain diameter. h is the flow height given as the product of number of grains and the grain diameter.

The fluid inertial stress are a result of turbulent mixing of the fluid (Takahashi, 2007, p. 25). These inertial stresses in the fluid can be compared to Reynold stresses developing in a turbulent fluid (Iverson, 1997b):

$$T_{f(i)} \sim v_f \rho_f \dot{\gamma}^2 \delta^2 \quad (2.3)$$

The parameters of this expression are defined as for equation (2.2) above, only here the f in subscript indicate that these are the parameters representing the fluid.

Stresses also occur as a result of grains in contact (Iverson, 1997b; Takahashi, 2007, p. 25). These stresses build due to the friction between the particles that are in contact. The quasi-static Coulomb friction stress describes these contact stresses (Iverson, 1997b):

$$T_{s(q)} \sim N_g v_s (\rho_s - \rho_f) g \delta \tan(\phi) \quad (2.4)$$

The equation utilizes some additional parameters which yield: N_g gives the number of grains for the depth, from a layer given and upwards, g is the gravitational acceleration and $\tan(\phi)$ is the friction coefficient between particles. A similar expression to this equation has been given by using the solid concentration instead of number of grains and velocity of solids (Takahashi, 2007, p. 25).

Fluid stresses occur due to deformation of the fluid within the flow (Takahashi, 2007, p. 24). These deformations result in a shearing stress. Utilizing Newtons law of viscosity, which gives that the shear stresses and shear strains are proportional with viscosity, μ_v, as the proportionality constant (Crowe et al., 2009, p. 19), the expression for the quasi-static fluid stresses is given as (Iverson, 1997b):

$$T_{f(q)} = v_f \dot{\gamma} \mu_v \quad (2.5)$$

Since a debris flow consists of both a fluid and solid phase, it is natural that stresses can occur due to the interaction of these two phases. The stresses building because of this interaction, result from the relative motion of the two (Iverson, 1997b). These interaction stresses are a result of the permeability of void space, the fluid flow on a grain-size scale, which cause a buffer of the interaction between particles (Iverson, 1997b; Takahashi, 2007, p. 24). The interaction stresses are hence given as (Iverson, 1997b):

$$T_{s-f} \sim \frac{\dot{\gamma} \mu_v \delta^2}{\kappa} \quad (2.6)$$

Where the expression also includes the viscosity, μ_v and the permeability κ.

Dimensionless numbers may be used to indicate and describe flow behavior (Iverson, 1997b; Takahashi, 2007, p. 25) by the stresses defined prior in this section. Examples of these dimensionless numbers are given in Table 2 below. The dimensionless numbers give an indication of the dominance of one stress over the other, and in this way, they can say something about how the fluid will act.

Table 2 Dimensionless numbers to describe flow behavior (Iverson, 1997b).

Dimensionless number	Name	Description
$N_{Sav} = \frac{T_{s(i)}}{T_{s(q)}} = \frac{\dot{\gamma}^2 \rho_s \delta}{N(\rho_s - \rho_f) g \tan(\phi)}$	Savage number (modified to take friction into account)	Gives the domination of the inertial solid grain stress, $T_{s(i)}$, to the quasi-static solid stress, $T_{s(q)}$.
$N_{Bag} = \frac{T_{s(i)}}{T_{f(q)}} = \frac{v_s}{1 - v_s} \cdot \frac{\rho_s \delta^2 \dot{\gamma}}{\mu}$	Bagnold number	The Bagnold number is large in an inertial debris flow (Takahashi, 2007).
$N_{mass} = \frac{T_{s(i)}}{T_{f(i)}} = \frac{v_s}{1 - v_s} \cdot \frac{\rho_s}{\rho_f}$	Mass number	Describes the dominance of inertial solid grain stress, $T_{s(i)}$, to initial fluid stress, $T_{f(i)}$
$N_{Dar} = \frac{T_{s-f}}{T_{s(i)}} = \frac{\mu}{v_s \rho_s \dot{\gamma} k}$	Darcy number	The solid-fluid interaction stress, T_{s-f}, over the inertial solid grain stress, $T_{s(i)}$. Indicates the buffering against interaction between grains by help of the pore pressure.
$N_{Rey} = \frac{N_{Bag}}{N_{mass}} = \frac{\rho_f \dot{\gamma} \delta^2}{\mu}$	Reynolds number	The Bagnold number over the mass number. The Reynolds number can classify a flow as turbulent or laminar (Crowe et al., 2009, Chapter 10.1).
$N_{Fric} = \frac{N_{Bag}}{N_{Sav}} = \frac{v_s}{1 - v_s} \cdot \frac{N(\rho_s - \rho_f) g \delta \tan(\phi)}{\dot{\gamma} \mu}$	Friction number	The Bagnold number over the Savage number, indicating the dominance of shear stress due to grain contact over the viscous shear.

2.3.3 Some simple frameworks

Iverson (1997b) also mentions some experiments that show correlations of the dimensionless numbers and motions of the debris flows. In a dry granular flow, if the Savage number is greater than 0.1, the flow will act in a state that show that grain collision stresses will be dominant over the grain friction stresses (Savage & Hutter, 1989). If the Savage number is small, the dominating stress is due to the frictional actions (Savage & Hutter, 1989). And if the Savage number is large, the particles are prone to fluctuations, resulting in collisions and generation of grain collisional stresses (Savage & Hutter, 1989).

Experiments performed by Bagnold (Bagnold, 1954) show relations of the dimensionless Bagnold number. The transition zone of the Bagnold number, when grain inertial stresses

transmitted by grain collisions start to dominate the viscous stresses, happens around Bagnold numbers of 200 (Bagnold, 1954; Iverson, 1997b).

Other experiments have been performed to give the indication of a range of the domination of fluid interaction stresses through the Darcy number. If the Darcy number ranges between 1000 and 6000, the interactions of the soil and fluid are strong (Iverson, 1997b; Iverson & LaHusen, 1989).

The friction number is defined as the ratio of the Bagnold and the Savage number (Iverson, 1997b). It expresses the ratio of the shear collisional stresses to the viscous shear stresses. The transition zone for the friction number when frictional behavior overtakes the domination on the viscous behavior happens for $N_{fric} > 1400$ (Iverson & LaHusen, 1993).

Based on the dimensionless numbers, Iverson (1997b) proposes a framework to classify debris flows from the following dimensionless numbers: The Savage number (N_{Sav}), the Bagnold number (N_{Bag}) and the Darcy number (N_{Dar}). It is these three dimensionless parameters that are used for the purpose of this framework, since they are defined as most likely to deviate between different flows. They are therefore good parameters for separating different flows from each other (Iverson, 1997b). Figure 3 shows the debris flows defined as a shaded area. Extreme values of the dimensionless Bagnold number, Savage number or Darcy number will lead to debris flows transforming into other types of motion like a dry rock avalanche, a muddy water flow or an earthflow respectively. The shaded field considers the different variable cases of debris flows, like the triangle from dynamic debris flows in Figure 4. This framework is however very simplified.

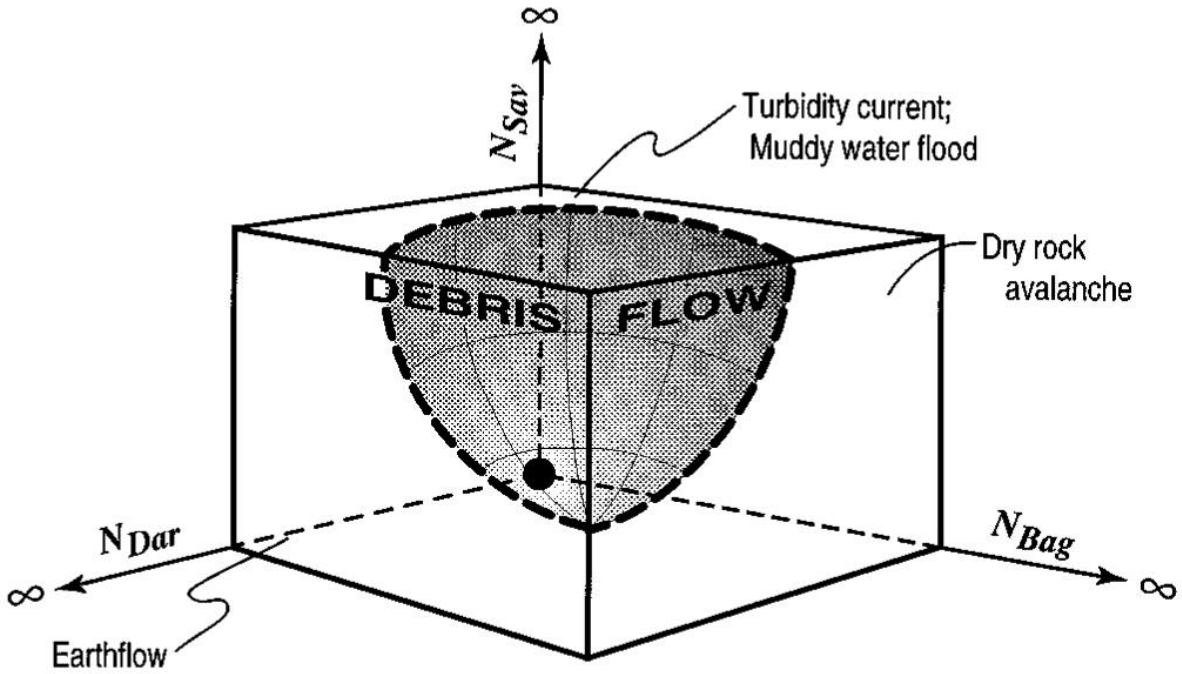

Figure 3 Classification scheme which gives indication on debris flow motion based on the Darcy number, the Bagnold number and the Savage number (Iverson, 1997b).

Takahashi (2007, p. 27) used these stresses and dimensionless numbers to build a framework to define debris flow motion. This framework is depicted in Figure 4. Takahashi (2007, p. 27) however uses slightly different notations: The T_c parameter is defined as the shear stress due to particle collision and is similar to the solid inertial stress, $T_{s(i)}$, from equation (2.2). T_t is defined as the stress occurring as a result of turbulent mixing and can be compared to the inertial stresses of the fluid, $T_{f(i)}$, in equation (2.3). T_{sq} is the quasi static Coulomb friction stress similar to $T_{s(q)}$ given in equation (2.4). Takahashi (2007, p. 25) also gives a shear stress building as a result of the fluid deformation, which is comparable to the quasi-static fluid stress of Iverson (1997b) in equation (2.5). These can hence be seen presented in the framework of Figure 4.

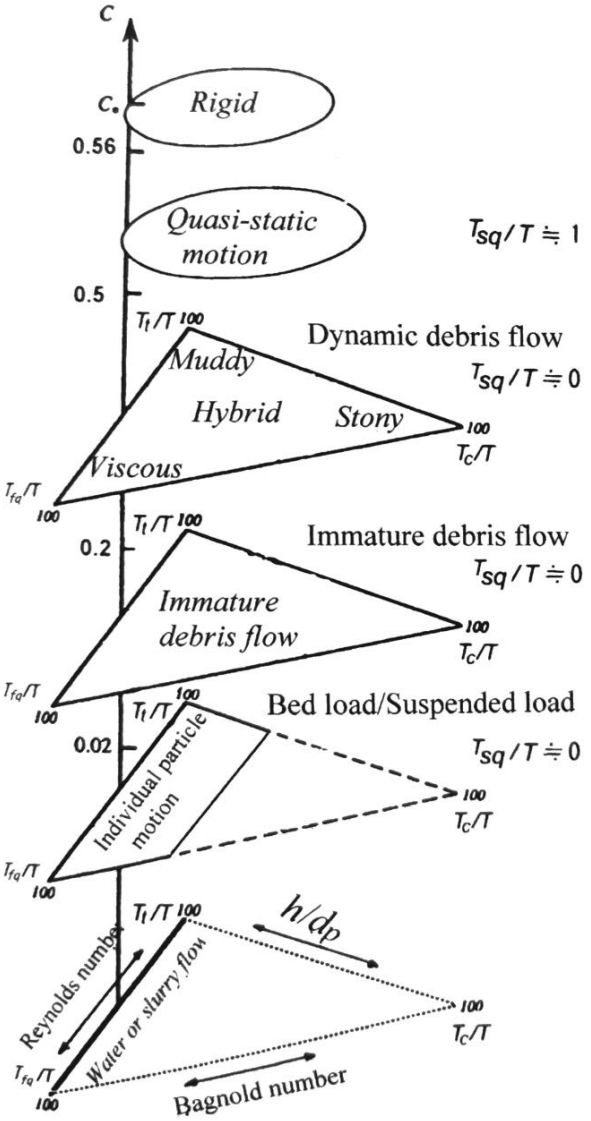

Figure 4 Different criteria for the motions of the solid and fluid mixtures (Takahashi, 2007, p. 27).

A debris flow can either be quasi-static or dynamic (Takahashi, 2007, p. 26). The first kind is dominated by frictional stresses while the second type can be divided into three subcategories (Takahashi, 2007, p. 26). The three categories can be obtained from the uppermost triangle in Figure 4. They are: muddy, stony and viscous debris flows. The three categories of dynamic debris flows are defined based on which stresses that

dominate. The muddy debris flows, also called turbulent-muddy type, are dominated by the turbulent mixing stresses, T_t (Takahashi, 2007, p. 26). The stony kind of debris flows are defined as where the stresses due to grain collisions dominate (Takahashi, 2007, p. 26). For the last type, the viscous debris flows, the dominating stress is quite obviously, are the viscous stresses such as the shearing stress due to fluid deformation, T_{fq}, dominates (Takahashi, 2007, p. 26). One can see, that this matches well with the definitions at the tip of the triangle.

The placing along the vertical axis in the model in Figure 4 is dependent on the solid concentration, C. This vertical axis contains some threshold values, for the different motions. The threshold value that determines the difference between dynamic and quasi-static debris flows, depends on when the Coulomb friction stresses will dominate, which is when the solids concentration is larger than about 0.5 (Takahashi, 2007, p. 26). Another threshold is for the distinction between quasi-static and rigid motion. This is when the debris flow material can become rigid and neither of the two prior motions described are possible. This threshold is given as a solid concentration of 0.56 for a beach sand (Bagnold, 1966; Takahashi, 2007, p. 26). There is also another threshold value indicated, which is a dynamically determined threshold giving at which point particles are dispersed over the entire height of a debris flow, but it is not defined by the debris flow contents (Takahashi, 2007, p. 26).

What has been mentioned until now, only covers the top part of the framework in Figure 4. The model also covers the existence of immature flows, when the flow contents are bed load or suspended load, and when the flow does not include coarse particles and the flow becomes water or slurry flow. The last one is dominated by shear, viscous and turbulent Reynold stresses, and since it has no coarse particles, it is located at the bottom of the vertical axis (Takahashi, 2007, p. 26). The next to last one, with contents of bed load or suspended load, is moved further up along the vertical axis, as there is some solid concentration, but less than the threshold of 0.02 (Takahashi, 2007, p. 27). Between a solid concentration of 0.02 and 0.2, the debris flow is immature and stresses that dominate are the collision stress, but only in the lower layer (Takahashi, 2007, p. 27). Each tip of the triangle, indicates when the all of the shear stress is equal to the respective stresses (Takahashi, 2007, p. 27). The dimensionless numbers are also included in the framework through the distance between to tips of a triangle. This distance represents the ratio between the stresses that dominate at the tips, giving different distances to be the Bagnold number, the Reynolds number and the relative depth (which is additional to two of the dimensionless numbers).

The aim of this framework is to be able to compare different characteristics of debris flows, using different physical parameters of the flows (Takahashi, 2007, p. 24). The other dimensionless numbers, that are not included in this framework, could still help characterizing a debris flow, since they describe other stresses that can affect such a flow, and which of the stresses that dominate, indicating the different mechanisms of momentum transport.

2.3.4 Flow behavior according to the Froude number

The Froude number is an indicator of a relative force in the fluid (Crowe et al., 2009, p. 261). This number, is useful in gravitational driven flows, where the gravity influences the pattern of flow (Crowe et al., 2009, p. 259). The Froude number is a dimensionless number for a general geometry. It is a ratio of the kinetic force to the gravitational force (Crowe et al., 2009, p. 258).

$$(2.7) \qquad Fr = \frac{Kinetic\ force}{Gravitational\ force} = \frac{v}{\sqrt{gL}}$$

v is the velocity of the flow, $L\ is$ the length of the flow, while g is the gravity acceleration.

The value of the Froude number can also be used to classify a flow. A non-uniform flow changes its velocity in different sections (Crowe et al., 2009, p. 511). A debris flow is therefore a highly non-uniform flow, since the velocity will change from section to section. It is also stated in Crowe et al. (2009, p. 524) that a Froude number equal to 1, describes a critical flow. A critical flow is described as when the flow has minimum specific energy for a given amount of discharge, see Figure 5. From Figure 5, it is obtained, that if flow depths are less than the depth of a critical flow, the flow is characterized as *supercritical*. Also, if flow depths are larger than the critical depths, the flow is characterized as *subcritical*.

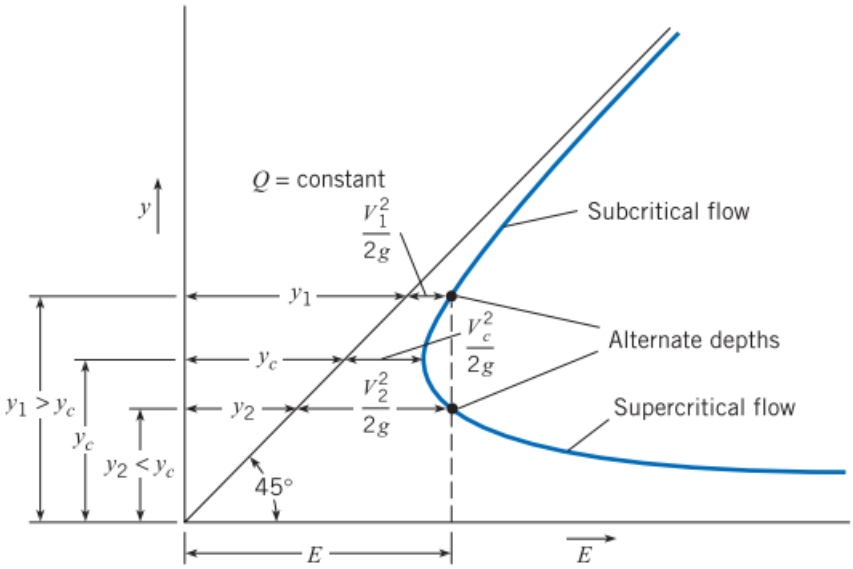

Figure 5 The relation between the specific energy of a flow, and the flow depth (Crowe et al., 2009, p. 523).

The condition of critical flow is very unstable (Crowe et al., 2009, p. 527), as can be seen from Figure 5: a tiny change in the specific energy, will result in a large change in the flow depth. Looking at the formula for the Froude number in (2.7), it is obtained that the Froude number decreases for a larger flow depth. Hence, as the flow depth increases, the Froude number will decrease, giving that a Froude number less than 1 indicates a subcritical flow. The same reasoning can be done for the decrease of flow height, resulting in an increase in the Froude number, which in such case relates to a supercritical flow. Summarized this becomes (Crowe et al., 2009, p. 546):

- Fr = 1 indicates a critical flow
- Fr < 1 indicates a subcritical flow
- Fr > 1 indicates a supercritical flow

Scheidl et al. (2013) stated that Froude numbers in small scale tests, mainly have higher values compared with observations to real scale. Reasons for this are that small-scale tests have smaller depths while simultaneously having large velocities, resulting in quite high Froude numbers. In the master thesis of Vicari (2018), the obtained Froude numbers are between 4 and 8.

2.3.5 Properties

The dimensionless numbers given in the previous sections in addition to some general, essential properties for a debris flow are given values for in Table 3 and Table 4 below. Some properties can be determined when the material is in a fixed state, while others, such as the bulk density, must be determined during motion (Iverson, 1997b). Iverson (1997b) presents some typical values of the basic physical properties of a debris flow mixture, both separate parameters for the solid and fluid phases, and properties of the entire mixture, these are presented in Table 3.

Table 3 Some physical properties of the debris flows (Iverson, 1997b).

Property	**Symbol**	**Typical values**
Solid grain properties		
Mass density, $\mathbf{kg/m^3}$	ρ_s	2500-3000
Mean diameter, m	δ	10^{-5}-10
Friction angle, deg	ϕ_g	25-45
Restitution coefficient	e	0.1-0.5
Pore fluid properties		
Mass density, $\mathbf{kg/m^3}$	ρ_f	1000-1200
Viscosity, Pa s	μ_v	0.001-0.01
Mixture properties		
Solid volume fraction	V_s	0.04-0.8
Fluid volume fraction	V_f	0.2-0.6
Hydraulic permeability, $\mathbf{m^2}$	κ	$10^{-13} - 10^{-9}$
Hydraulic conductivity, m/s	K	$10^{-7} - 10^{-2}$
Compressive stiffness, Pa	E	$10^{3} - 10^{5}$
Friction angle, deg	ϕ	25-45

Some dynamic properties of the debris flows, such as velocities and flow heights are given in Table 4 below. Table 4 also gives some indications of the values of the dimensionless parameters. Values are given for the experimental flow of the USGS experiments and for three natural events. From Table 4 it can be seen that the experimental flows seem to for example underestimate the flow heights and the friction number, while overestimating the Savage and Bagnold number.

Table 4 Dimensional and dimensionless parameters that influence stresses in debris flows (Iverson, 1997b).

Parameter	USGS Flume experiments on Sand-Gravel	Oddstad debris flow	South Toutle River	Osceola Mudflow
Dimensional parameters				
δ, m	0.001*	0.001*	0.001*	0.001*
h, m	0.1	1	5	20
v, m/s	10	10	20	20
$\dot{\gamma}$, 1/s	100	10	4	1
ρ_s, kg/m^3	2700	2700	2700	2700
ρ_f, kg/m^3	1100	1100	1100	1200
μ, Pa s	0.001	0.01*	0.01*	0.1*
g, m/s^2	9.8	9.8	9.8	9.8
k, m^2	10^{-11}	10^{-11}*	10^{-12}	10^{-12}
E, Pa	10^4*	10^4*	10^4*	10^4*
v_s	0.6	0.6	0.6	0.6
v_f	0.4	0.4	0.4	0.4
ϕ, deg	40	30	30	30
Dimensionless parameters				
N_{sav}	0.2	$2*10^{-4}$	$6*10^{-6}$	$1*10^{-7}$
N_{Bag}	400	4	0.2	0.4
N_{mass}	4	4	4	4
N_{Dar}	600	60,000	$2*10^6$	$6*10^7$
N_{Rey}	100	1	0.04	0.01
N_{fric}	$2*10^3$	$2*10^4$	$3*10^4$	$4*10^5$

2.3.6 Entrainment in debris flows

As presented in prior, in section 2.3.1, debris flows may pick up material along its path. This erosion mechanism, can cause flows that are initially small, to grow larger and become the rapid, hazardous phenomena that is referred to earlier (Berger et al., 2011). According to Hungr et al. (2014), the moving of the debris flow in a channel, can cause the bed material to liquefy or experience an increase of pore pressure. This will then in turn lead to entraining of material into a surge that grows. Travelling of the surges down the channel, the erosion of the flow can undermine banks and continue to pick up material (Hungr et al., 2014; Jakob & Hungr, 2005, p. 135).

The basics of the entrainment process can be illustrated by Figure 6 obtained from (Jakob & Hungr, 2005, p. 139). The debris flow flows over a bed material with no cohesion. The thickness of the flow is given by z_d and the angle of the slope is given by β. The forces acting on a given column at some point in the debris flow, are shown in the right illustration in Figure 6. When the debris of a height z_d overrides the bed material, the bed becomes unstable to a depth given by z from the original terrain. The weight of the unit column given to the right in Figure 6 is a sum of the unit weight of the bed

material, γ, multiplied by the erosion depth, and the unit weight of the debris, γ_d, multiplied by the flow height.

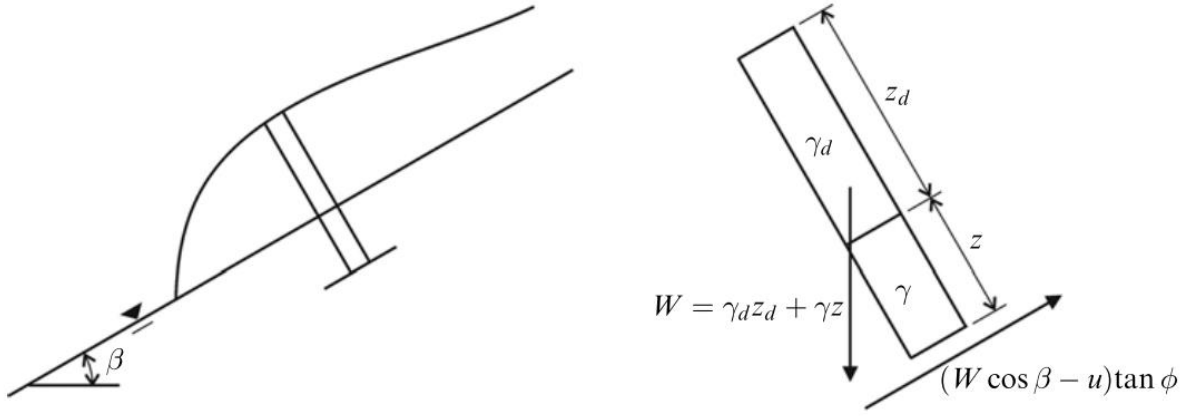

Figure 6 A schematic illustration of the entrainment process in a debris flow (*Jakob & Hungr, 2005).*

Based on the weight of the unit column, the stresses on the base are given to be (Jakob & Hungr, 2005, p. 140):

$$\sigma = Wcos\beta$$

$$\tau = Wsin\beta$$

Using basic mechanics, σ is the stress normal to the base, while τ represents the shear stress along the column base.

To start an analysis of the bed material the simple assumptions of seepage parallel to the slope, uniform flow and instant drainage can be made. This is not consistent with the case for a debris flow at all but useful to start scrutinizing the bed material entrainment. By making these assumptions the pore fluid is caused to follow a hydrostatic rule and steady state regime (Jakob & Hungr, 2005, p. 140):

$$u = \gamma_w(z_d + z)\cos(\beta)$$

The stresses together with the pore pressure then results in the shear resistance of the bed material given by the Coulomb equation to be:

$$S = (\sigma - u)\tan(\phi)$$

Where ϕ is the friction angle. This now represents the resistance of the bed material. At failure the shear strength, S, is equal to the shear stress, τ. This gives an expression for the possible erosion depth, z, for the given assumptions (Jakob & Hungr, 2005, p. 140):

$$z = z_d \left[\frac{\frac{\gamma_d}{\gamma}\left(1 - \frac{\tan\beta}{\tan\varphi}\right) - \frac{\gamma_w}{\gamma}}{\frac{\gamma_w}{\gamma} - (1 - \frac{tan\beta}{tan\varphi})} \right]$$

As stated, prior it is highly unlikely that debris flows experience a steady state seepage. A more likely condition achieved is assumed to be that the entire bulk weight of the flow

is shifted to the pore water through undrained loading. The bulk weight of the debris flow is set to: $\gamma_d z_d$. Hence pore pressure is given as (Jakob & Hungr, 2005, p. 141):

$$u = (z_d\gamma_d + z\gamma_w)cos\beta$$

The possible erosion depth z based on these assumptions becomes (Jakob & Hungr, 2005, p. 141):

$$z = z_d\left[\frac{-\frac{\gamma_d}{\gamma}\left(\frac{\tan\beta}{\tan\varphi}\right)}{\frac{\gamma_w}{\gamma} - (1 - \frac{tan\beta}{tan\varphi})}\right]$$

The erosion depth will increase as a result for increased bulk density of a debris flow.

The theory of this is simple but the true reality is not as easily presented. Pore pressures are unlikely to predict as easy as they are highly variable, and it can be difficult to know the strength and depth of the bed material (Jakob & Hungr, 2005, p. 141). However, these equations may give some indications on the extremities of the possible unstable depth in a flow.

How much material is entrained is also a result of the flow properties and the bed material properties (Jakob & Hungr, 2005, p. 176), these can determine how much resistance the flow experiences, and hence the ability to pick up material. Also affecting the erosion, is the geometry of the channel (Jakob & Hungr, 2005, p. 176).

2.4 Debris flow countermeasures

2.4.1 Proposed framework

To reduce the hazardous consequences of debris flows, countermeasures are introduced. A suggested countermeasure is the building of barriers. Barriers can be placed in slopes with natural channels to hinder the granular flows (Ng et al., 2018). Mitigation measures can be divided into structural and non-structural countermeasures (Proske et al., 2011; Takahashi, 2007, p. 336), in which rigid barriers count as structural. Also, the mitigation measures can be either active or passive, where active ones directly influence the process of a debris flow by preventing or dampening the event (Proske et al., 2011). Other examples of structural barriers are check dams, baffles or even the planting of trees (Takahashi, 2007, p. 336). In the following, only the use of intermediate rigid barriers will be discussed. In particular, the use of one single intermediate barrier. According to Kwan (2015), the barrier acts in a way that when the debris flow hits the barrier, a portion of the debris will be held back by the barrier. As a result of the barrier retaining debris, the debris flows loose some of its kinetic energy (Kwan et al., 2015). Also, the barriers can induce a time delay on the flow front, which results in a slightly longer travel time (Kwan et al., 2015).

Kwan et al. (2015) proposed a framework in which they present a method on assessing the design of multiple intermediate barriers to intercept the debris flows. In their research, they conducted a debris mobility analysis, which took the effect of obstruction of the debris flows due to multiple intermediate barriers into account. These analyses resulted in the noting of several parameters for a debris flow overflowing barriers. The parameters can be obtained from Figure 7 and are further discussed later.

The mobility assessment (Kwan et al., 2015) considers the debris piling up behind a barrier and launching into a ballistic flight after the overflow of the barrier crest. The

assessment also considers the energy dissipation upon impact with the channel bed. These features are shown in Figure 7. When the zone behind the barrier is fully filled, the debris that remains in the flow is launched into a ballistic flight (Kwan et al., 2015). From the crest of the barrier, the remaining debris will then carry the kinetic energy of the remaining landslide (Kwan et al., 2015). It should also be noted that if a barrier is filled prior to the debris flow, e.g. by an earlier debris flow, the capacity of the barrier can be neglected for calculation purposes (Kwan et al., 2015).

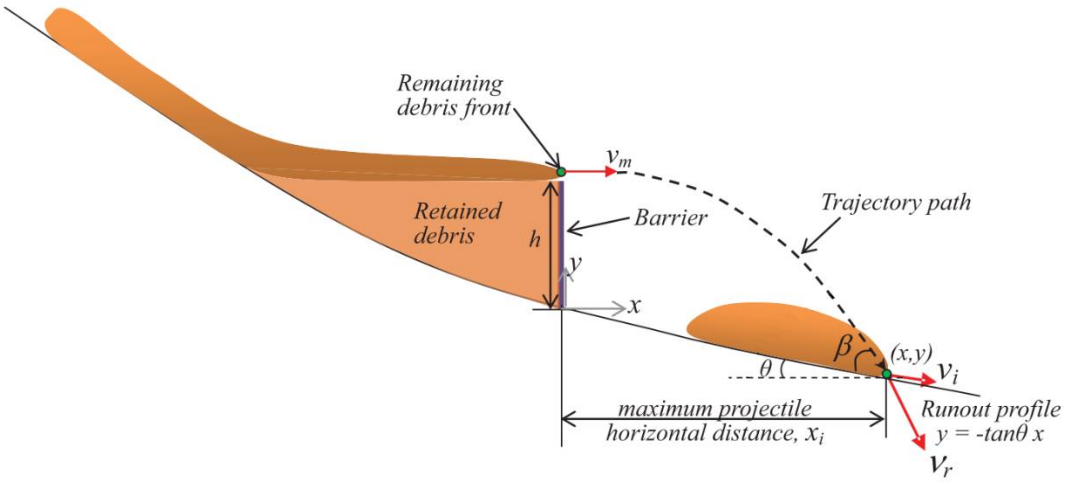

Figure 7 The flow path of a debris flow hitting a barrier and the parameters determining the dynamics of the debris flow path (Kwan et al., 2015).

Koo et al. (2017) studied the effect on barrier impact loads, by taking the effect on debris attenuation into consideration, with the help of physical modelling. As a result of this work, they proposed an impact load model which takes the change of momentum flux due to the interaction with a barrier into account. The model that is proposed, is stated to be valid for use on granular flows (Koo et al., 2017). It uses a staged run-up behavior of the flow behind the barrier, which is illustrated in Figure 8.

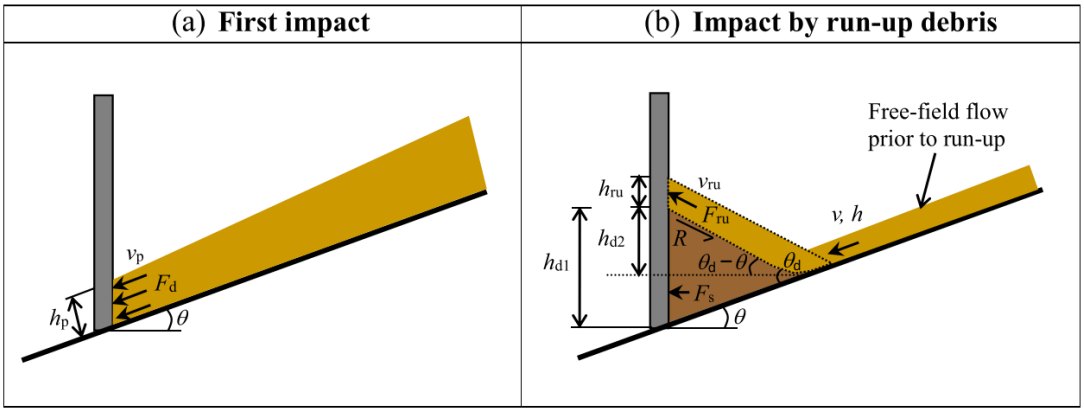

Figure 8 The impact mode, showing a schematic diagram for the impact of the barrier (Koo et al., 2017).

Ng et al. (2019) uses the work of both Kwan et al. (2015) and Koo et al. (2017), and suggests a new analytical framework for the design of multiple rigid barriers. They use physical experiments to evaluate and validate the framework. The experiments consisted of different flows impacting a barrier. The findings of Ng et al. (2019) are in general that the framework estimates the attenuation of the velocity during impact of the barrier, the

overflow velocity and landing distance quite well. The tests conducted by Ng et al. (2019) verify this. The overflow distance of the barrier is also given in the model, and the final recommendation is that the actual barrier spacing should be larger than the calculated overflow distance (Ng et al., 2019).

Figure 7 shows the debris flow hitting a barrier and how the debris is retained. Further the figure shows the debris front launching into a ballistic flight and how it will follow the trajectory path. The material can be seen to hit at an angle, β, at which point the debris flow has a new initial speed.

2.4.2 Barrier design according to framework

The main challenge in designing a barrier is due to the requirement for the barrier to resist quite a large impact velocity (Kwan et al., 2015). According to Kwan (2015), the intermediate barriers should be placed at wide positions that are flat parts of the drainage line. These conditions are favorable for decreasing the hazard of a rapid flow, by slowing it down (Kwan et al., 2015). Due to the launch of ballistic flight over the crest of the barrier, the height of the barrier should be optimized and not excessive (Kwan et al., 2015).

Ng et al. (2019) and Kwan (2015) present the framework for the design of rigid barriers shown in Figure 9. The framework proposed by Ng et al. (2019), consists of three parts: the impact model, the overflow trajectory and the landing model. The path of the ballistic flight is determined by the height of the barrier the debris material is launched from (Ng et al., 2019). When the ballistic flight comes to an end, at the end of the trajectory path, the velocity is reduced at impact between the debris flow material and the channel bed (Kwan et al., 2015). The velocity reduces, due to the energy dissipation of the flow material as it collides with the channel bed at an angle (Ng et al., 2019).

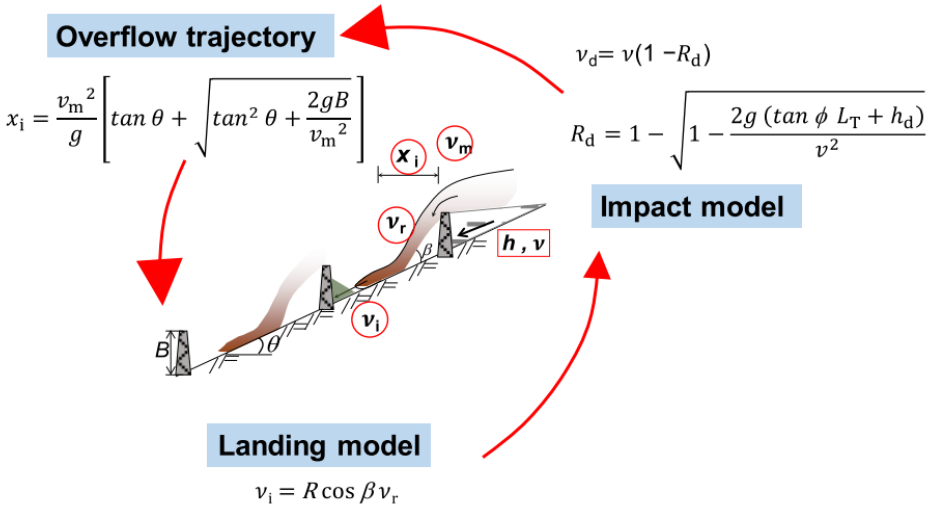

Figure 9 The framework of multiple barrier design (Ng et al., 2019).

Kwan (2015) presents the design equations for assessing the dynamic motion of the landslide debris overflowing a barrier. Figure 7 in the previous section presents the parameters in the model. x_i represents the horizontal length projected by the debris flow trajectory path. v_m is the horizontal velocity of the debris flow launched from the crest of the barrier. v_r is the velocity of the debris material right before impact with the channel bed. The velocity is given at an angle to the slope. v_i gives the velocity after impacting

the channel bed. This velocity is parallel with the slope. θ represents the angle of inclination of the channel and h is the height of the barrier.

The trajectory path projection, x_i, is obtained from energy conservation principle and is given by the following formula (Kwan et al., 2015):

$$x_i = \frac{v_m^2}{g} \cdot [tan\theta + \sqrt{\tan^2\theta + \frac{2gh}{v_m^2}}] \quad (2.8)$$

The debris flow velocity prior to landing is from Kwan et al. (2015) derived based on the kinetic energy of the debris and the kinetic energy that is gained from a drop in height:

$$v_r = \sqrt{\frac{2[KE_r + m_r g(h + C_x x_i tan\theta)]}{m_r}} \quad (2.9)$$

In this equation, KE_r, represents the kinetic energy of the remaining debris after the first barrier. C_x is a correction factor for the horizontal length of the trajectory path and m_r is the mass of the remaining debris after passage of the first barrier. g is the gravitational acceleration.

The velocity parallel to the slope after impact with the channel bed is given by Kwan et al. (2015) as follows:

$$v_i = v_r \cos\beta \quad (2.10)$$

Where β is given as

$$\beta + \theta = \tan^{-1}\sqrt{\frac{m_r g(h + C_x x_i tan\theta)}{KE_r}}]\} \quad (2.11)$$

R represents the velocity correction factor and the value is correlating with the material used at the channel base. All other parameters are previously described.

Combining equations (2.10) and (2.11), the final expression for this velocity is obtained:

$$v_i = R v_r \cos\{[\tan^{-1}\sqrt{\frac{m_r g(h + C_x x_i tan\theta)}{KE_r}}] - \theta\} \quad (2.12)$$

Figure 9 contains also a model for the impact on the barrier, in addition to the overflow trajectory and landing model. As some of the material starts to arrest behind the barrier, the rest of the material has to climb upon it, resulting in a drag between the resting and flowing material (Ng et al., 2019). The event of attenuation is hence described by Koo et al. (2017) with help of the run-up velocity, v_d, and factor of attenuation, R_d:

$$v_d = v(1 - R_d) \quad (2.13)$$

$$R_d = 1 - \sqrt{1 - \frac{2g(tan\phi L_T + h_d)}{v^2}} \quad (2.14)$$

L_T represents the travel distance of the debris flow in the run-up behind the barrier. ϕ is described by Ng et al. (2019) as the angle of repose, and is in Koo et al. (2017) described as the internal friction angle of the retained material. h_d is the height of the retained granular material behind the barrier. Ng et al. (2019) present a modified figure of the depositing mechanism behind the barrier, see Figure 10. The original one is presented in Koo et al. (2017).

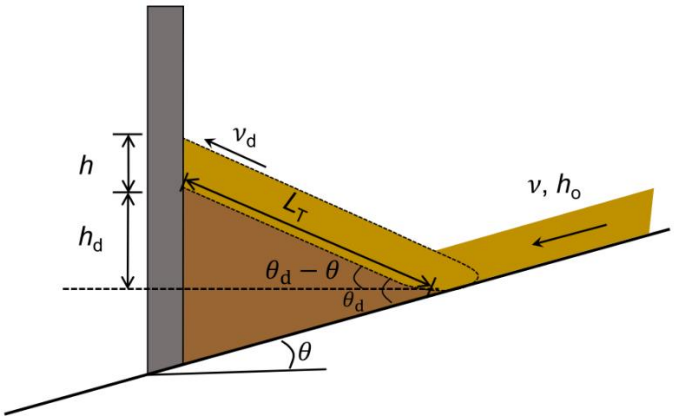

Figure 10 Parameters of the retained material behind the barrier (Koo et al., 2017; Ng et al., 2019).

θ_d is the deposition angle of the material, which makes $\theta_d - \theta$ the net deposition angle. v is the free flow velocity and h_o is the free field thickness. Lastly, h is given as the run -up thickness (Koo et al., 2017).

2.5 Numerical modelling

Numerical models can provide information to the users on debris flow heights, velocities and runout distances. This can in turn provide useful information in the assessment of e.g. countermeasures and mapping of hazard areas.

Many types of numerical models exist. Two categories among the dynamic models are:

1. Lumped mass models
2. Continuum based models

2.5.1 Lumped mass models

The lumped mass models use a single rigid block to represent the potential sliding mass on the inclined surface to predict the debris flow motion through a path (Pirulli, 2005). Since the mass moves as a single block, the lumped mass model is not able to predict any internal deformations of the flow. In addition these models are also not able to predict the distribution of the height and velocity of the flow (Pirulli, 2005). The lumped mass models are able to give some approximations on how the center of gravity of the sliding mass moves downslope (Hungr, 1995). However they are no able to estimate the motion of the flow front (Hungr, 1995).

The debris flow mass initially has a potential energy due to its elevation. As it moves downslope it loses its potential energy to other forms, such as kinetic energy. Kinetic energy increases as a function of the debris flow mass travelling downslope. The energy at any given point along the slope can be found from an energy balance (Vicari, 2018). Resistance in the sliding mass is exerted through friction between the block and the sliding surface of these models (Hungr, 1995; Pirulli, 2005). This friction acts when the inclination angle is sufficiently low. If the inclination angle is above this limit, Newtons second law rules the acceleration of the mass (Pirulli, 2005). Total energy loss will also be dependent on any resisting forces acting against the motion. According to Pirulli (2005), the most well-known lumped mass models use the center of mass approach combined with the ideas of Voellmy (1955). The ideas suggest a turbulent flow resistance based on the square of the velocity (Voellmy, 1955).

The use of lumped mass models has declined in favor of numerical simulations based on continuum mechanics, in addition using historical data (Pirulli, 2005).

2.5.2 Continuum mechanics models

The most commonly used approaches to model debris flows is the use of continuum-based models. The continuum-based models allow the given mass of a debris flow geometry and velocity to change through the path of the flow. In these models the granular material of a debris flow which in reality consists of a variety of particles, is treated as a one phase continuum (Pirulli, 2005). The continuum models are associated with a rheological model (Hungr, 1995).

The continuum-based models use conservation equations of mass and momentum. These equations describe dynamic motion of the debris flow (Quan, 2012). The rheological model defines the behavior of the flowing debris. Since the material is treated as a continuum, the thickness of the sliding mass is larger than several particle diameters (Savage & Hutter, 1989). Solving the governing equations, properties of the debris flows can be obtained (Quan, 2012).

Integration of the internal stresses in e.g. the direction normal to the bed is used in many cases to simplify the continuum models from three dimensions to two. Since the most appropriate flow laws are not clearly given and basal friction is dependent on several factors, depth-averaged models which do not require precise input of the mechanical behavior of the flow can be useful to assess the flow dynamics of granular flows (Pirulli, 2005; Savage & Hutter, 1989).

This single-phase flow approach uses global rheological properties for the entire flow. Although the flows in this model are described as in a single phase, effects of the interstitial fluid may not be neglected (Takahashi, 2007, p. 35). Hence, it becomes important to set properties to the fluid that can simulate a realistic bulk behavior of the flowing mass (Pirulli, 2005; Vicari, 2018). To ensure suitable characteristics of the apparent fluid, one must use a rheological model that describes the relationship between the shear stress and the rate of shear strain realistically (Takahashi, 2007, p. 38).

2.5.3 Rheology

As stated above, continuum mechanical models are associated with a rheology model. By integrating the rheological relationship of the equivalent single phase fluid, the basal resisting force is obtained as a function of the flows mean velocity, density and depth (Hungr, 1995; Pirulli, 2005). Rheological models used in debris flows adopt the concept of fluid flows to use on granular masses (Yifru, 2014).

Viscosity is defined as the ratio of applied shear stress to the rate of shear strain (Pierson & Costa, 1987). Based on the viscosity some definitions of the fluids can be made, these are also given in Figure 11. The resistance of forces associated with the rheology are acting inside the flow and in the contact surface between the flow and surface of the bed (Quan, 2012). The basal flow resistance T assumes a linear increasing shear stress with depth to give a relation between the resistance and the other parameters of the flow (Hungr, 1995).

A Newtonian fluid is described as a fluid that flow independently of increasing or decreasing shear stress for a constant temperature. Viscosity is constant. (Pierson & Costa, 1987; Yifru, 2014). When viscosity is decreased as a function of increasing shear strain, the flow exhibits a shear-thinning behavior and is called pseudoplastic (Pierson &

Costa, 1987; Yifru, 2014). The opposite behavior is shown for the dilatant fluid, which exhibits a shear-thickening behavior as viscosity increases with the rate of shear strain.

In some cases, there is no flow happening until a certain threshold value is reached given by the upper three curves of Figure 11. This may happen for some naturally occurring materials (Pierson & Costa, 1987). First when this yield strength is exceeded, the material can flow. In a Bingham fluid, the viscosity is constant after hitting the yield stress, making the rate of shear strain proportional to the shear stress (Pierson & Costa, 1987; Yifru, 2014). There are also versions of the previously described dilatant fluid and pseudo-plastic fluid which exhibit a certain yield strength.

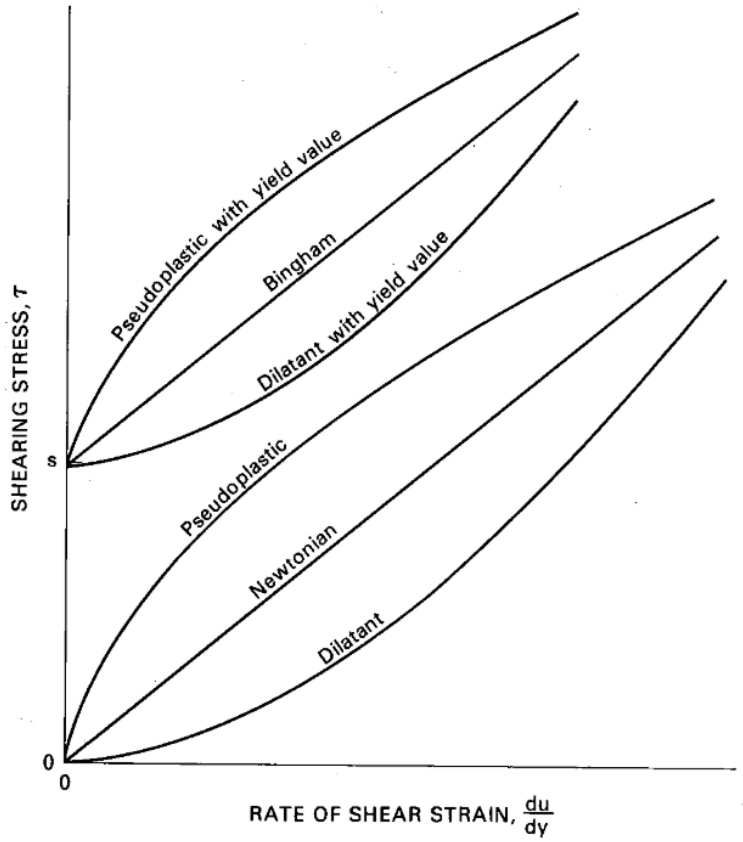

Figure 11 Flow curves of different rheologic behavior (Pierson & Costa, 1987).

Debris flows are multi-phase and consist in general of phases of solid and water. The distribution of the solid and fluid components together with the grain size distribution and physical and chemical properties of the solid phase, will affect how the flow responds to shear stress (Pierson & Costa, 1987). Pierson and Costa (1987) propose that the rheologic response of a mixture of sediment and fluid is given primarily by the concentration of sediments. The two other effects on the response to shear stress become less important compared to this (Pierson & Costa, 1987). Figure 12 shows the variation in rheology and classification of the flow based on velocity and solid concentration. Granular flows are at the higher end of the sediment concentration, giving a non-Newtonian behavior. When particles start to interact, the flowing fluid obtains a yield strength introducing this behavior (Pierson & Costa, 1987).

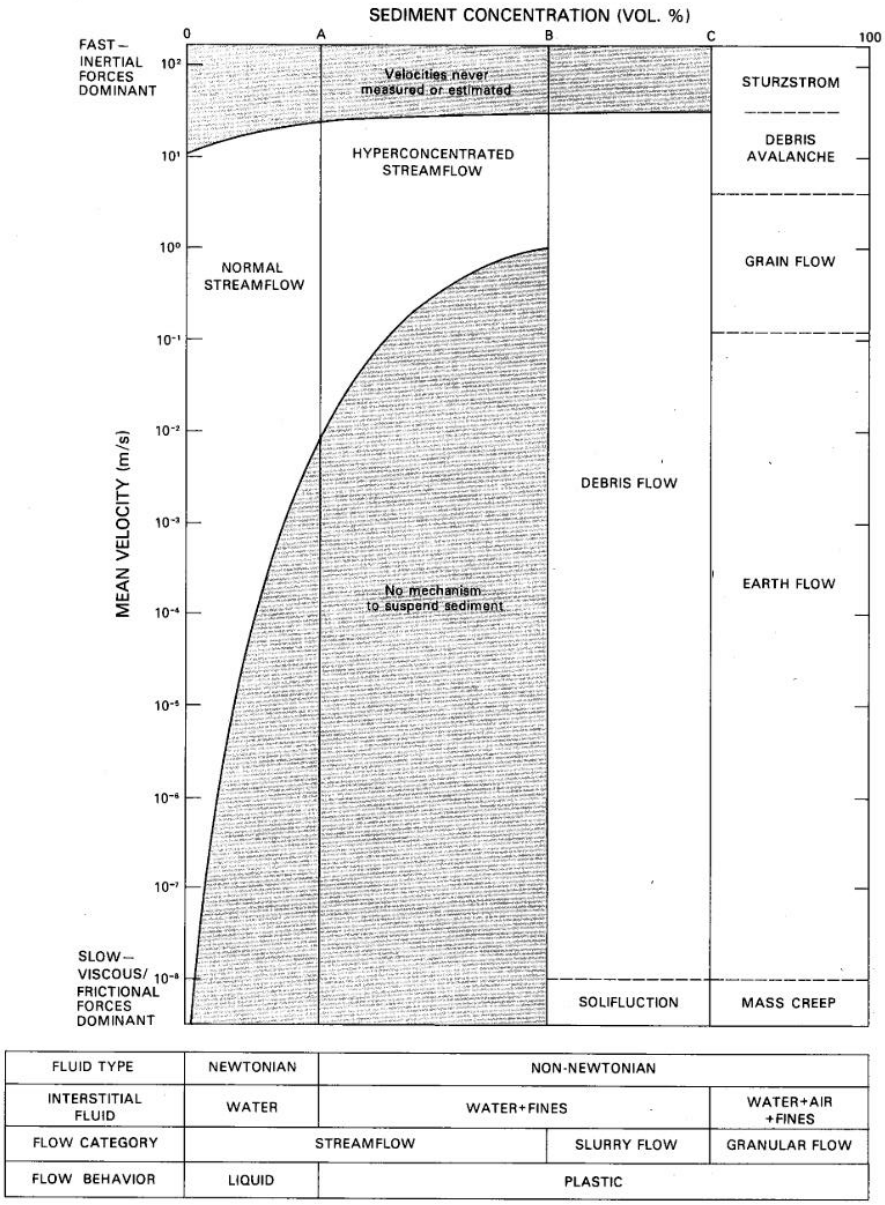

Figure 12 Classification scheme based on rheological behavior and existing nomenclature (Pierson & Costa, 1987).

The basal resistance of the flow called T, is dependent on which rheology that is used for the material (Hungr, 1995). A_i is the base area of the boundary block and is given as the product of length of the base d_s and the width B_i.

According to Pierson and Costa (1987) the term debris flow is the most appropriate for both the behavior of a viscous slurry flow and an inertial slurry flow. A viscous slurry flow is characterized by viscous forces controlling the flow. Viscous forces can control the flow when the values of shear rates, mean grain diameter, grain density and water content are low (Bagnold, 1954; Pierson & Costa, 1987). Bingham model is stated to be appropriate in the kinds of flow where the intergranular fluid consists of clay, silt and water (Major & Pierson, 1992). This model has been used for numerous debris flows (Takahashi, 2007, p. 40). The resistance of this model is given by solving the third degree equation for the mean flow velocity as given in Hungr (1995):

$$v_i = \frac{H_i}{6\mu_v}\left(\frac{2T}{A_i} - 3\tau + \frac{\tau^3 A_i^2}{T^2}\right)$$

The resting force is hence given dependent on the flow depth, velocity, the constant yield strength τ, and the Bingham viscosity μ_v.

However, when the pore fluid has low viscosity and the shear rate, grain diameter and grain density are high, the opposite of the beforementioned case, the dominating forces are different. For this case, the inertial forces dominate the flow behavior and hence, momentum transfers as particles collide (Pierson & Costa, 1987). These inertial slurry flows can be modelled by a dilatant fluid model with a yield strength (Takahashi, 2007). Takahashi (2007, p. 42) uses the dilatant model on what he calls stony type of debris flows.

Another rheologic model given in Hungr (1995) is the Voellmy rheology. This model was originally introduced for snow avalanches (Voellmy, 1955). The model concerns a friction term and a coefficient concerning the turbulence of the flow given the Greek letter ξ. Hungr (1995) justified the use of this rheological model by showing to the results of (Bagnold, 1954). As the granular material is sheared the strength of the material will increase with a function of the squared strain rate (Bagnold, 1954; Hungr, 1995). The friction resistance of a landslide would hence increase proportionally the velocity squared (Salm, 1993). The resistance force of the Voellmy rheology is as given in Hungr (1995):

$$T = A_i[\gamma H_i\left(\cos(\alpha) + \frac{a_c}{g}\right)\tan(\phi) + \frac{\gamma v_i^2}{\xi}$$

The slope angle is expressed as α in this case. Additionally, a_c defines the centrifugal acceleration. The Voellmy rheology is discussed more in the next section.

2.5.4 Numerical modelling in RAMMS

RAMMS::Debris flows, is a numerical software that simulates rapid mass movements and is developed by SLF, which is the Institute of Snow and Avalanche research in Switzerland. The application of this software concerns the hazard analyses of debris flows and is a two-dimensional dynamic modelling tool. By considering the hazards of the debris flow phenomena, this software can be used as an aid to provide information in the design of preventive measures. One can use this software to look at different aspects of avalanches, since it has been thoroughly calibrated with real-life events from Switzerland (Fischer et al., 2012). The simulations look at different effects of debris flow runout and has the possibility to investigate both flow heights and velocities. In such a way, one can analyze large scale events or parameters that can influence these events.

RAMMS uses a an Eularian reference frame for solutions (Yifru, 2014). The program requires different kinds of input concerning the data for the region of interest, the physical properties of the debris flow, properties of material prone to erosion and barrier geometrics and locations, if there are any. The program is based on a continuum mechanical Voellmy model which uses the two parameter Voellmy rheology (Bartelt et al., 2017; Quan, 2012). Other programs such as e.g. DAN 3D allow for the use of several different rheology for modelling the debris flows while RAMMS is solely based on this rheology (Quan, 2012).

The geographic area is described by topographic data, through a Digital Elevation Model (DEM). The area is restricted by some given boundaries. According to the RAMMS::Debris flow Manual (2017), there are two methods that define the release mechanism of the

debris flows: Block release and input hydrograph. Each of these has its own advantages. The debris flows are put in either of two categories: unchanneled and channelized debris flows (2017). Unchanneled debris flows are in the manual (Bartelt et al., 2017, p. 14) described as:

"Hillsope debris flows or shallow landslides."

Channelized debris flows given by the manual (Bartelt et al., 2017, p. 14) as:

"…develop in regions where torrents limit the flow paths and the debris material mainly follows the torrent channel."

For the case of unchanneled debris flows, it is recommended to use the block release mechanism, while it is suggested to use hydrograph input for the channelized flows (Bartelt et al., 2017). The input in these release mechanisms, strongly influences the results (Bartelt et al., 2017). Block release allows for the entire mass to be released from a given area at an initial height, while hydrograph allows for constraining of the quantity of debris material into the domain (Bartelt et al., 2017).

In the DEM, the elevation of the model is given as a function of the possible mass movement directions. Hence, the height of the surface is expressed through x-, y- and z-coordinates where z=z(x,y) (Christen et al., 2010; Quan, 2012). The vector of the gravitational acceleration of the flow becomes $g=(g_x, g_y, g_z)$ and time is expressed as *t.* The two main flow parameters in RAMMS are the flow height and mean velocity. The two parameters are in Christen et al. (2010) given as:

- Flow height

$$H(x,y,t)$$

- The mean velocity

$$\boldsymbol{U}(x,y,t) = \begin{bmatrix} U_x(x,y,t) \\ U_y(x,y,t) \end{bmatrix}$$

  Where U_x and U_y are velocities in x and y directions respectively.

Magnitude and direction of the flow are given through the norm of the mean velocity $\boldsymbol{U}$ and unit vector of $\boldsymbol{U}$, respectively.

Since RAMMS uses the Voellmy-Salm model, mass and momentum balance are given as (Christen et al., 2010):

$$\partial_t H + \partial_x(HU_x) + \partial_y(HU_y) = \dot{Q}(x,y,t) \tag{2.15}$$

$$\partial_t(HU_x) + \partial_x\left(c_x HU_x^2 + g_z k_{\frac{a}{p}} \frac{H^2}{2}\right) + \partial_y(HU_x U_y) = S_{gx} - S_{fx} \tag{2.16}$$

$$\partial_t(HU_y) + \partial_x(HU_x U_y) + \partial_y\left(c_y HU_y^2 + g_z k_{\frac{a}{p}} \frac{H^2}{2}\right) = S_{gy} - S_{fy} \tag{2.17}$$

Where the first equation is the mass balance and the second and third equations give the momentum balance in x and y direction respectively. $\dot{Q}(x,y,t)$ in the mass balance equation describes mass production and will show entrainment for values greater than zero and depositions for values less than zero. In the momentum balance equation, the c-factor is a shape profile of the velocity profile. And $k_{\frac{a}{p}}$ represents the earth pressure coefficients which are described in the next section. The S-terms in the momentum balance express the gravitational and frictional acceleration respectively. Gravitational acceleration is given as the product of the gravitational constant g in the respective

direction and the flow height H. The basal resistance, S_f, is explained in the next paragraph.

The rheological model uses an additional resistance is proportional to the squared of the velocity. According to the RAMMS::Debris flow manual (2017), these two frictional resistances can be described as, the dry Coulomb type of friction and the velocity-squared type of friction, with parameters μ and ξ relatively. Based on expressions given in Salm (1993), the RAMMS software uses the following relation in describing the frictional resistance in a debris flow:

$$S = \mu N + \frac{\rho g \mathbf{u}^2}{\xi},\ N = \rho h g cos(\phi) \qquad (2.18)$$

In the formula, S is the total frictional resistance given in Pa, N is the normal stress on the travelling surface of the debris flow, μ is the dry friction coefficient, ξ is the velocity squared drag coefficient, ρ is the density of the flow, g is the gravitational acceleration, **u** is the velocity vector, h is the flow height and ϕ is the slope angle. The velocity vector contains the velocity components in x and y direction, $\mathbf{u} = (u_x, u_y)^T$.

This rheology model models the complex behavior of the two-phase material using a one phase rheology. The dry Coulomb type of friction for the solid phase is expressed with the parameter μ and the turbulent friction associated with the squared velocity is given through the parameter ξ (Bartelt et al., 2017). The behavior of the debris flow can hence be expressed using the friction coefficients. When the flow is slowing down, the dry friction μ is dominating the motion, while the turbulent friction ξ dominates the motion if the flow runs fast (Bartelt et al., 2017).

The simulations in RAMMS also allow for the implementation of the yield stress in materials. Materials have no linear relation of the dry friction, hence the software introduces cohesion through a modification in the Voellmy rheology (Bartelt et al., 2017). By introducing the parameter N_0, the yield stress is implemented in the relation of the frictional resistance, and equation (2.18) now yields:

$$S = \mu N + \frac{\rho g \mathbf{u}^2}{\xi} + (1-\mu)N_0 - (1-\mu)N_0 e^{-\frac{N}{N_0}} \qquad (2.19)$$

The use of cohesion in the friction resistance of the Voellmy rheology, ensures that as the normal stresses reduces towards zero, the friction is reduced towards zero.

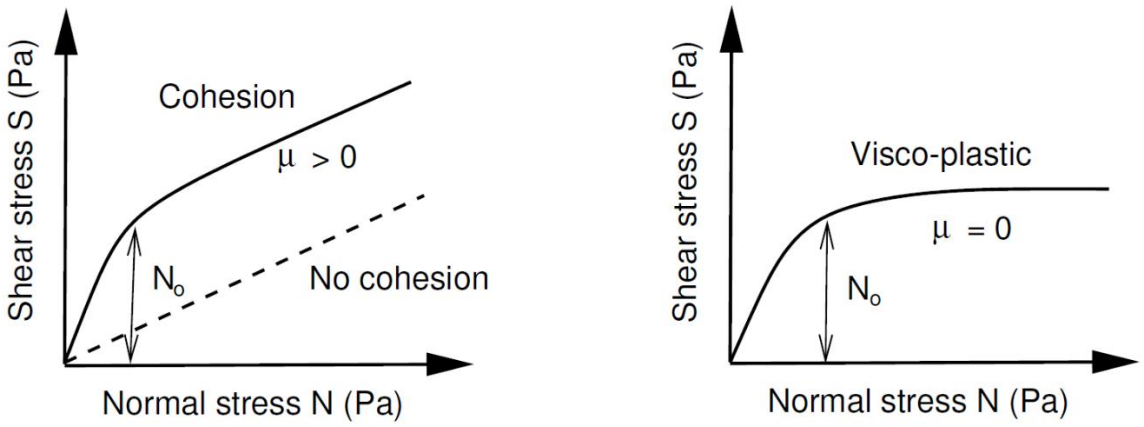

Figure 13 Figures that show the relation between shear stress and normal stress with the effect of cohesion. If there is no cohesion, the behavior is visco-plastic as shown in the right figure (Bartelt et al., 2017).

The RAMMS software was physically and mathematically improved by Fischer et al. (2012). As a result, the software can include effects of curvatures in the topography. Curvature effects show to introduce a substantial contribution to the dynamics of the debris flows. The effects are considered through adding a centrifugal force the normal force N (Bartelt et al., 2017; Fischer et al., 2012). The centrifugal force arises from decomposing the velocity dependent friction into two terms: first term depending on the topography which considers a rise in Coulomb friction due to curvature. The second term is independent of the topography. The centrifugal forces are a result of the centrifugal acceleration which is described as a product of the velocity and the terrain curvature (Fischer et al., 2012). The terrain curvature is given through a matrix $\boldsymbol{K}$. The centrifugal acceleration hence becomes:

$$f = \boldsymbol{u}\boldsymbol{K}\boldsymbol{u}^T$$

Which results in the centrifugal force:

$$F = \rho h f$$

Where ρ and h have been defined previously.

According to the RAMMS manual (2017), this force will often lead to increased friction along the flow path. This extended model has the ability to reduce to the prior model if there is no curvature (Fischer et al., 2012).

RAMMS enables the possibilities of taking erosion and barriers along the flume into account when modelling a debris flow. The erosion module of RAMMS is based on experimental results performed in Illgraben in Switzerland. The experiments investigated the timing and magnitude of erosion along the channel bed of three debris flows (Berger et al., 2011). Berger et al. (2011) state that significant amount of erosion can be expected as a result of the debris flows being confined into a channel.

RAMMS also can implement the active and passive earth pressure coefficients (λ) when running a simulation. The software only allows for a constant λ in the longitudinal direction throughout a given simulation. And as a result of $\lambda \neq 1.0$ the numerical scheme is reduced to first order.

2.6 Earth pressure coefficients

According to Bartelt et al. (1999) the flowing masses will experience considerable strains in the longitudinal direction. Savage and Hutter (1989) studied the flow and spreading of a given volume of granular cohesionless mass. The granular material was considered incompressible and basal sliding of the mass is hence given through a dry Coulomb friction law. Sliding occurs mainly in a thin confined layer at the base (Savage & Hutter, 1989). The stress states appearing in the longitudinal direction and normal to the inclination in a sliding mass can be related through an earth pressure coefficient (Bartelt et al., 1999; Savage & Hutter, 1989):

$$p_{xx} = k_{act/pas} \cdot p_{zz} \tag{2.20}$$

Where p_{xx} describes the stresses parallel to the inclination of the slope and p_{zz} the stresses perpendicular to the slope. The earth pressure coefficient is given with the letter *k* above but is in literature also defined with the use of the Greek letter λ (Bartelt et al., 1999).

For a given stress state it is possible to have two Mohr's circles that satisfy both the basal sliding law and internal yield criterion simultaneously as shown in Figure 14. If the stress in the longitudinal direction is larger than the overburden stress at the base, the behavior is regarded as passive and the movement is compressional (Savage & Hutter, 1989). If the stress parallel to the slope is less than the overburden pressure at the base, the masses have an active behavior, which associates with dilatational motion based on the hypothesis of Savage and Hutter (1989). Hence the earth pressure coefficients can be either active or passive depending on the behavior of the avalanching masses.

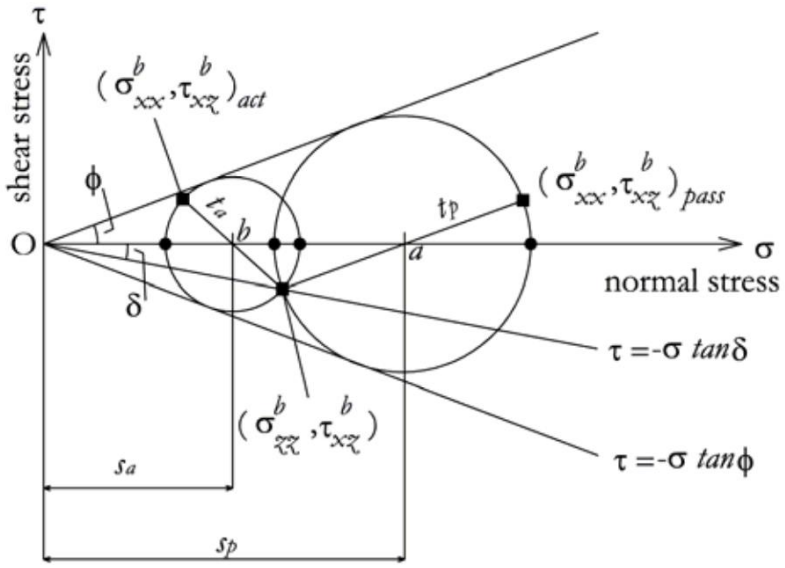

Figure 14 A Mohr circle showing the yield Coulomb criterion ($\tau \cdot tan(\delta)$), the friction angle (φ) and the active and passive stress states.

If the motion is active or passive is dependent on the gradient of the velocity (Gray et al., 1999). If the gradient of the velocity is larger than or equal to zero, the earth pressure becomes active, while a velocity gradient less than zero is associated with a passive state. The longitudinal earth pressure coefficient is hence defined as follows:

$$K_{x,act}: \frac{\partial u}{\partial x} \geq 0$$

$$K_{x,pas}: \frac{\partial u}{\partial x} < 0$$

The different mechanisms imposed by the active and passive pressure coefficient in a sliding mass are by Bartelt et al. (1999) given through Rankine's active and passive pressure coefficients, through the use of the internal friction angle φ. Their work focused mainly on snow with a common internal friction angle in the range of $20°$ to $40°$, giving a range for the active pressure coefficient between 0.2 and 0.5 and a range for the passive pressure coefficient between 2.0 and 4.6.

$$\begin{matrix}\lambda_{act} \\ \lambda_{pas}\end{matrix}\} = \tan^2(45° + \frac{\varphi}{2}) \qquad (2.21)$$

Earth pressure coefficients can be defined in both longitudinal and lateral direction. By using geometric relations and the Mohr circle in Figure 14 however, the earth pressure coefficients in the longitudinal and lateral direction are determined to be expressed through the bed friction angle (δ_1) and the internal friction angle (ϕ) (Hutter et al., 1993; Savage & Hutter, 1989).

The earth pressure coefficients are hence defined to be the following for direction parallel to the slope (Iverson & Denlinger, 2001; Savage & Hutter, 1989):

$$k_{x,act/pas} = 2 \cdot \frac{1 \mp \sqrt{1 - \cos^2(\varphi)[1 + \tan^2(\delta_1)]}}{\cos^2(\varphi)} - 1 \qquad (2.22)$$

The "+"-sign results in passive state and the "-"-sign results in the active coefficient.

In the lateral direction the earth pressure coefficients are given as (Hutter et al., 1993):

$$k^{x}_{,y,act/pas} = \frac{1}{2}(K_x + 1 \mp \sqrt{(K_x - 1)^2 + 4\tan^2(\delta_1)}) \qquad (2.23)$$

The lateral coefficients are given as a function of the longitudinal coefficients and can according to Pirulli (2005) be derived as four different earth pressure coefficient following the formula given by Hutter et al. (1993). One active and passive lateral coefficient ($k_{y,act/pas}$) for each active and passive coefficient in the longitudinal direction ($k_{x,act/pas}$). These earth pressure coefficients are given based on if the behavior in the lateral and longitudinal direction is active or passive:

$$K^{x,act}_{y,act}: \frac{\partial u}{\partial x} \geq 0, \frac{\partial v}{\partial y} \geq 0$$

$$K^{x,act}_{y,pas}: \frac{\partial u}{\partial x} \geq 0, \frac{\partial v}{\partial y} < 0$$

$$K^{x,pas}_{y,act}: \frac{\partial u}{\partial x} < 0, \frac{\partial v}{\partial y} \geq 0$$

$$K^{x,pas}_{y,pas}: \frac{\partial u}{\partial x} < 0, \frac{\partial v}{\partial y} < 0$$

The earth pressure coefficients presented in the Savage and Hutter theory (Hutter et al., 1993; Savage & Hutter, 1989) are more general than those of the classical Rankine theory (Iverson & Denlinger, 2001). The earth pressure coefficients mentioned in equations (2.22) and (2.23) are derived for a state where there is Coulomb failure is happening along the base and in the overlaying sediment simultaneously (Iverson & Denlinger, 2001). These relationships hence take the bed friction angle (δ_1) and the internal friction angle (φ) into account. For a special case of the bed friction angle being equal to zero, these relations will be reduced to the classical Rankine relations. If the internal friction angle is equal to the bed friction angle, Iverson and Denlinger (2001) present a much simpler expression for the active and passive coefficient:

$$k_{act/pas} = \frac{1+\sin^2(\varphi_{int})}{1-\sin^2(\varphi_{int})} \quad (2.24)$$

This indicates that no divergence or convergence occurs only if these two angles are equal.

Gray et al. (1999) describe the development of an avalanche with help of four earth pressure coefficients in downslope and cross-slope direction from release to runout. They performed experiments with on a parabolic inclined slope of $40°$ with a cylindrical shaped transition zone and a runout zone of $0°$. Total length of the inclined zone is 175 cm, the transition zone was 40 cm long and total length of runout zone was equal to 320 cm. The released material on the slope was quartz chips with a mean diameter between 2 and 4 mm. The internal friction angle of this material, $\varphi = 40°$ and the bed friction angle, $\delta_1 = 30°$. The development is shown in Figure 15 for the downslope earth pressure coefficient and in Figure 16 for the cross-slope coefficient.

According to these experiments, high velocities at the flow front makes the flow elongate in the downslope slope direction. Hence, the mass motion becomes divergent in this direction. This introduces the active earth pressure coefficient at t=0.51 s in Figure 15. The cross-slope behavior transitions from divergence to compression due to the curved slope, which introduces some active and some passive coefficients in Figure 16.

In the next phase at t=1.00 s, the avalanche has extended to span over the entire slope. At this point in time, all down slope and cross-slope earth pressure coefficients are introduced. The avalanche nose touches the horizontal plane while continuing to diverge in the downslope direction. The part of the avalanche in the transition zone shows compressional motion which associates with the passive coefficient longitudinally. The avalanche mass still on the inclined slope also shows a divergent motion. The lateral confinement of the channel ceases in the runout zone, giving the avalanche room to expand. The earth pressure coefficients will change accordingly to the change in motion.

When the avalanche nose has come to rest at t=1.51 s, the entire motion is compressional. However, since there are no lateral channel walls anymore, the avalanche is free to expand laterally, giving a cross-slope diverging motion. In this direction only the end of the tail of the avalanche experiences compression.

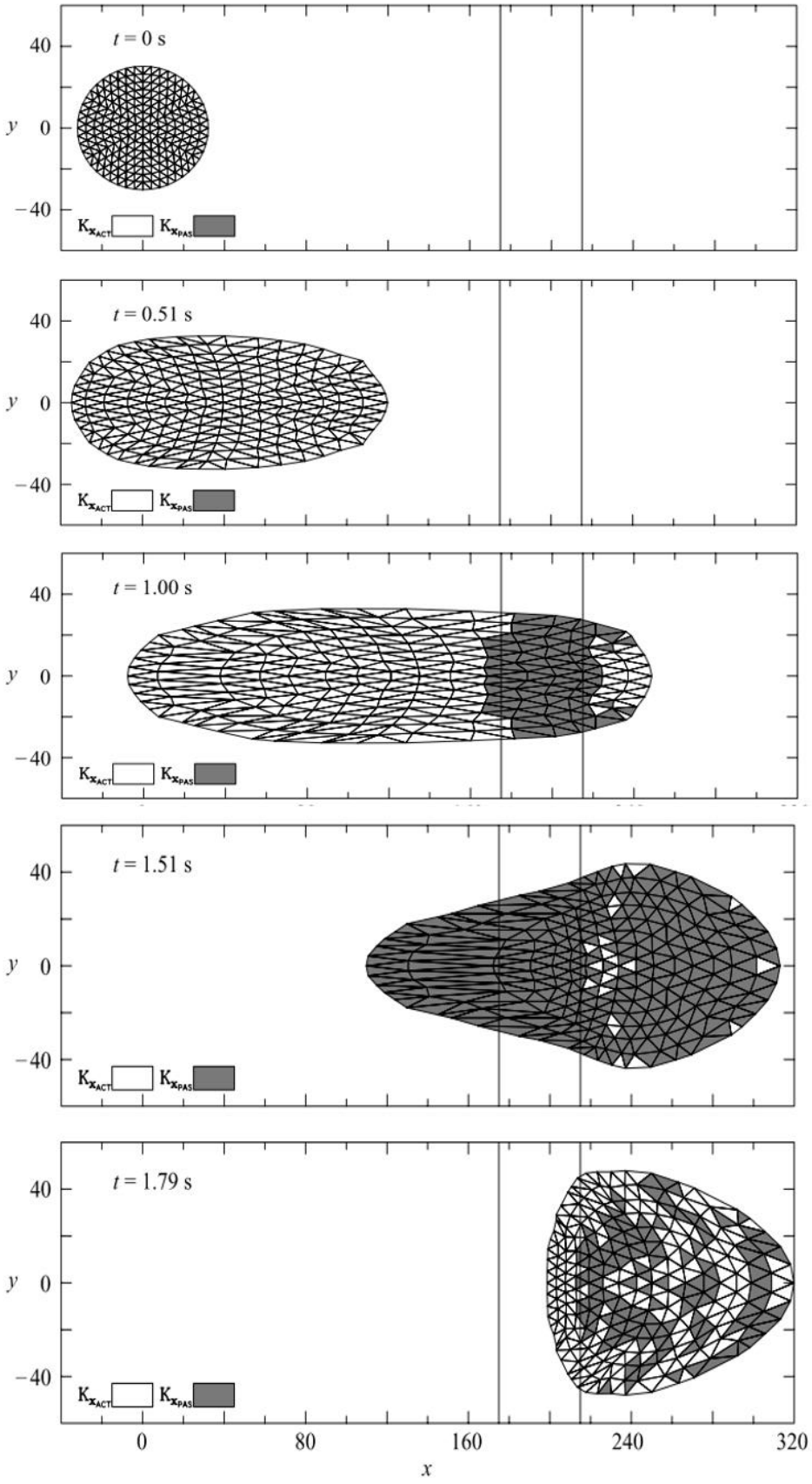

Figure 15 The development of the longitudinal earth pressure coefficients. Active earth pressure coefficients are white and passive coefficients are shaded (Gray et al., 1999).

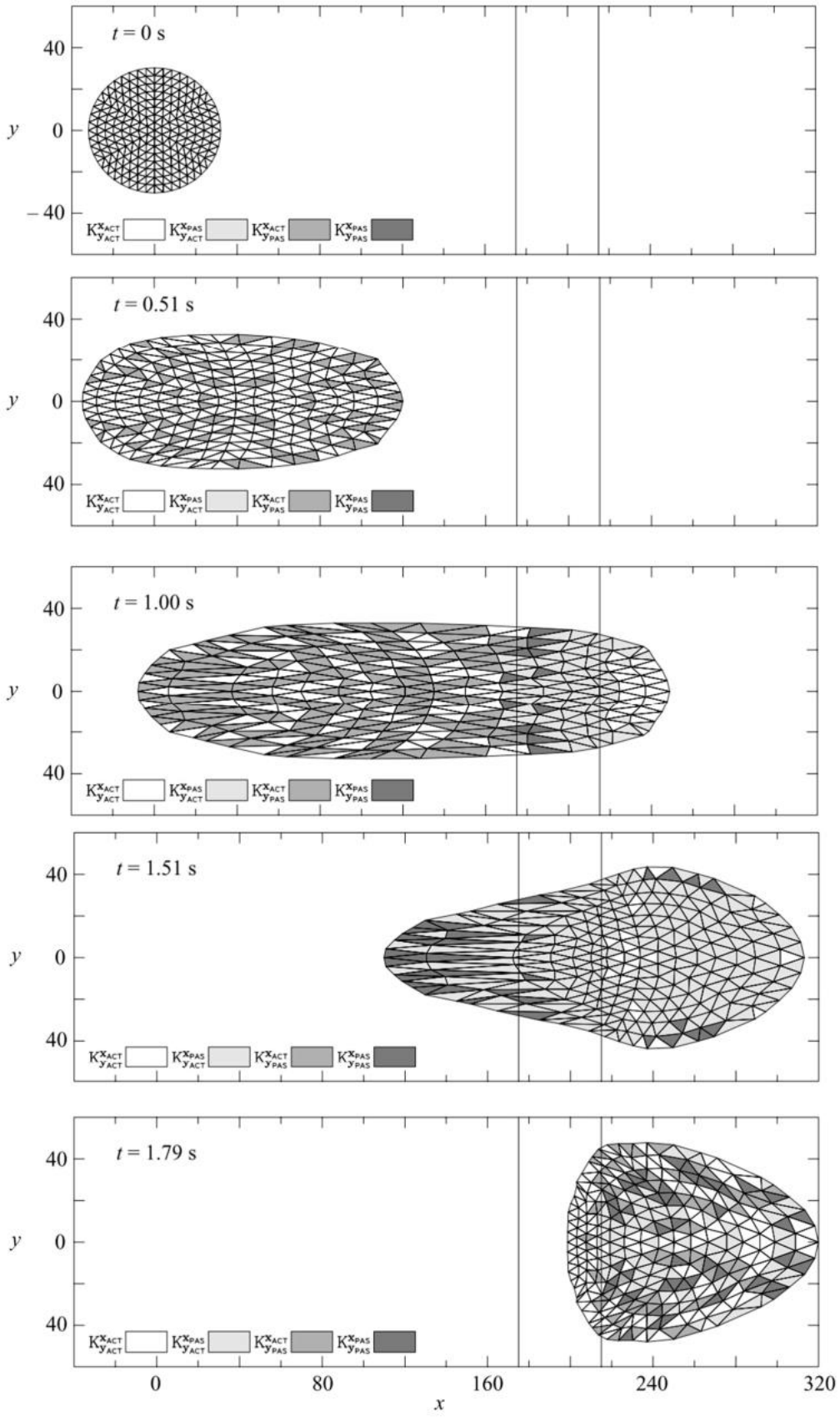

Figure 16 Development of the lateral earth pressure coefficients (Gray et al., 1999)

Pirulli (2005) describes two approaches for the modelling of the anisotropic earth pressure coefficient: the case of two coefficients where one is active and one is passive and the case of four earth pressure coefficients. The first approach shown in Figure 17, considers two earth pressure coefficients. This limits the flow to either converge or dilate simultaneously in x and y direction. Hence a passive or an active state applies in both directions. This is dependent on the velocity gradient as defined in prior. Second, the anisotropy hypothesis proposes the use of 4 values of the earth pressure coefficient, allowing for express opposite behavior in downslope and cross-slope direction, see Figure 18. This is also dependent on the velocity gradient.

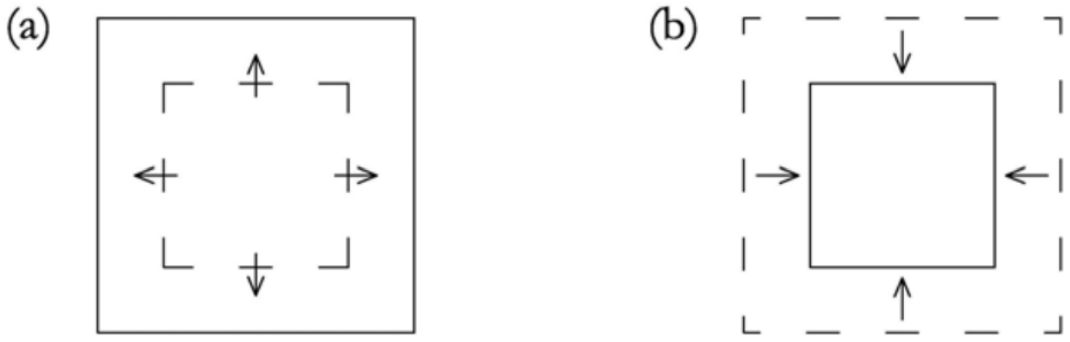

Figure 17 Simultaneously longitudinal and lateral (a) divergence or (b) compression in both directions (Pirulli, 2005).

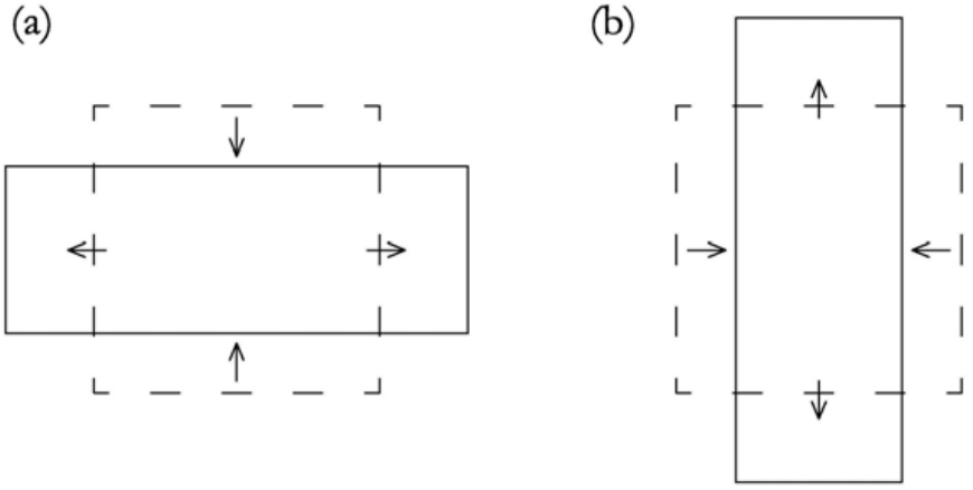

Figure 18 (a) Longitudinal divergence and lateral compression and (b longitudinal compression and lateral divergence (Pirulli, 2005).

The different position in time in the experiments of Gray et al. (1999) can be described as follows (Pirulli, 2005):

- **t=0.51 s**
  As this point in time associates with divergent motion of the downslope mass the gradients are assumed to be:

$$\left|\frac{\partial u}{\partial x}\right| > \left|\frac{\partial v}{\partial y}\right| \; ; \frac{\partial u}{\partial x} > 0$$

Meaning that the absolute value of the gradient is larger in the downslope than cross-slope direction and that there is divergence in the downslope direction. By using two earth pressure coefficients to give anisotropic state of stresses an active coefficient can be applied in both downslope and cross-slope direction. However, if four earth pressure coefficients are used to describe anisotropy it is possible to define an active or passive coefficient in the cross-slope direction depending on the motion.

- **t=1.00 s**
  Here three different phases of the flow are defined as the velocity gradient changes in the position in the flow:
  - Slope: the avalanching mass still left on the inclined slope shows a divergent motion in the longitudinal direction and convergence laterally: $\left|\frac{\partial u}{\partial x}\right| > \left|\frac{\partial v}{\partial y}\right|$; $\frac{\partial u}{\partial x} > 0$, $\frac{\partial v}{\partial y} < 0$, $\partial_x u + \partial_y v > 0$
  - Transition zone: the mass converges in the downslope direction and diverges in the cross-slope direction. The absolute value of gradient in the longitudinal direction is still greater than the gradient in the lateral direction: $\left|\frac{\partial u}{\partial x}\right| > \left|\frac{\partial v}{\partial y}\right|$; $\frac{\partial u}{\partial x} < 0$, $\frac{\partial v}{\partial y} > 0$, $\partial_x u + \partial_y v < 0$
    In Figure 15 and Figure 16, both active and passive coefficients are present, but the presence of active coefficients in the longitudinal direction and passive coefficients in the lateral direction is the greatest. The allowing of only two earth pressure coefficients would here not consider the different convergence and divergence longitudinally and laterally.
  - Horizontal plane: the avalanching nose touches the horizontal plane and diverges in the downslope direction and cross-slope direction: $\frac{\partial u}{\partial x} > 0$, $\frac{\partial v}{\partial y} > 0$; $\partial_x u + \partial_y v > 0$
- **t=1.51 s**
  As the entire motion is coming to rest, the behavior is compressional in the downslope direction.
  $$\left|\frac{\partial u}{\partial x}\right| > \left|\frac{\partial v}{\partial y}\right| ; \frac{\partial u}{\partial x} < 0$$
  If only two earth pressure coefficients are used, a passive coefficient is applied in both directions. Using four coefficients, the longitudinal earth pressure coefficient stays passive while an active coefficient is introduced laterally. This active coefficient can help to reduce the width of the runout.

For the remainder of this thesis, earth pressure coefficients are referred to as λ.

2.7 Previous testing and earlier models

Previous numerical modelling performed in RAMMS on physical models are given in Yifru (2014) and Vicari (2018).

The work of Yifru (2014) concerned the assessment of rheological models looking at the Voellemy friction parameters effect on runout distance in modelling of sensitive clay slides. Yifru (2014) introduces the modelling of laboratory tests in the numerical softwares RAMMS and DAN3D and gives indications of the input parameters and how to setup such a model in RAMMS.

Vicari (2018) conducted physical modelling of debris flows and numerical assessments of the Voellmy rheology parameters. The testing was conducted in a model allowing for

different configurations of the slope angles and release of the debris flow happening from a mixer. The angle configuration in these experiments was set to 17.5°. The effects of the Voellmy friction parameters were investigated in RAMMS based on the same model and back calculating the physical tests for calibration of these parameters. Further details on the model used for these physical experiments can be obtained from the next chapter, as the same model is applied for this thesis and a lot of the details still apply. A key result in this paper is that it can be hard to calibrate the friction parameters solely on the flow height and velocity, as the dry friction parameter μ and the turbulent friction parameter ξ, affect all three of those to a lesser or greater extent. A comment is made that one could compare the different parameters in the flume channel based on dimensionless numbers such as the Froude number (Fr), the Bagnold number (N_{Bag}), the friction number (N_{fric}) and the Savage number (N_{Sav}). It was proposed to use simplified dimensionless numbers to investigate the results in the numerical simulations, which only considered the dynamic components of the debris flow. These numbers deviate from the originals presented in Table 2 in section 2.3.2 (Vicari, 2018):

$$N_{sav} = \frac{\dot{\gamma}}{h} \quad (2.25)$$

$$N'_{bag} = \dot{\gamma} \quad (2.26)$$

$$N'_{fric} = \frac{h}{\gamma} \quad (2.27)$$

Where $\dot{\gamma}$ is the shear rate dependent on the velocity and grain size diameter, and h is the debris flow height. Iverson (1997b) obtained the shear rate $\dot{\gamma}$ as the flow velocity over the flow depth.

The results also show that deposition shape was hard to replicate with use of isotropic earth pressure coefficients and second order numerical scheme in the simulations. The deposition shape on this slope angle, resulted in runout of too wide lateral spread in the numerical simulation. It was suggested that the use of correct earth pressure coefficients could simulate the correct deposition shape.

Teetzmann and Shrestha (2019) investigated the effects of different flow parameters on erosion in a box through use of the same physical model as the thesis of Vicari (2018). The main difference in model setup for these experiments was that the slope angle was set to $30°$ instead of $17.5°$ and that the possibility for erosion in the flow was implemented in the model. The reference tests here was a volume of 25 L on a slope angle of $30°$. An erosion box was set in the channel at -0.4 m to -0.9 m from the end of the flume and start of the runout zone. This box is also described in more detail in Chapter 3. No numerical modelling was conducted for these experiments. It is noticeable for the results of these tests and also for the tests of Vicari (2018), that the Froude numbers in general are high and not in compliance with nature.

3 Experimental and numerical setup

The original plan was to study the effect of entrainment of bed sediments in a debris flow with an intermediate rigid barrier as a countermeasure in the channel. The use of a single barrier was already calculated for and planned into the model when labs were shut down. Due to the special events of March to May of 2020, it was not possible to go through with the physical modelling. Numerical modelling was hence used instead to study the effect of the use of an earth pressure coefficient in the simulation of debris flows in the software RAMMS instead. Even though the physical model was not directly used for experiments in this thesis, it is a still a central part of the numerical simulations. The physical model is used as the basis for the terrain model in the numerical simulations, hence it will be defined in detail in this section.

The barrier design is not implemented in the numerical model, as the two-dimensional equations in the software experiences numerical issues with overflow of a barrier. By still presenting the design of the barrier in this thesis, it is hoped to be helpful for use in later work.

The erosion box is also presented in this section as it was a part of the model for the tests of Teetzmann and Shrestha (2019) which is used as a reference case here. The effect of erosion will be discussed for the later part of this section but is not implemented in the numerical model.

Lastly, this chapter explains the choosing of the approaches for input in the design of the single intermediate barrier. The barrier was designed according to the framework presented in the literature.

3.1 The current model – experimental setup

This section concerns the design of the model that originally was supposed to be used in this thesis. It now makes out the basis for the numerical model. The current physical model is located at the hydraulics laboratory at NTNU, in the Department of Civil Engineering. It was established in 2018 by Ashenafi Yifru, and has previously been used for experiments both by himself and Hervé Vicari (Vicari, 2018; Yifru et al., 2018). This model contains improvements on an earlier model used at NTNU (Christiansen, 2013; Fiskum, 2012; Heller & Jenssen, 2009; Laache, 2016; Pradhan, 2017). The improvements are described in Vicari (2018): The flume channel has been elongated from 3.25 m to 5 m, it was also made narrower. The width is now 0.3 m instead of 0.6 m. The purpose of narrowing the channel is to allow a creation of a thicker debris flow. The new model also allows users to change the slope angle from a minimum of $17.5°$ to $30°$. The release mechanism was also improved for this model, changing it to a mixer, which mixes the debris flow material and takes account for previous problems with segregation of the material. For the specialization project of Teetzmann and Shrestha (2019), an entrainment box was also added in the flume channel to investigate the effects of entrainment in the debris flows.

The model setup which was planned for the testing in this thesis consists of several parts. A principal drawing can be seen from Figure 19. The setup consists of a release zone, where debris is released from a mixer, a channelized flow zone with a width of 30

cm and a runout path of 396 cm. In the principle drawing in Figure 19, the slope angle is set to 30°. The runout area slopes 2°. Prior to channelizing in the 30 cm wide channel, the debris flow travels through a channel of a wider cross-section of 60 cm. Debris material which travels longer than the length of the runout, dumps into a box at the end of the runout zone. If nothing else is stated, the slope angle of this thesis is fixed to 30°.

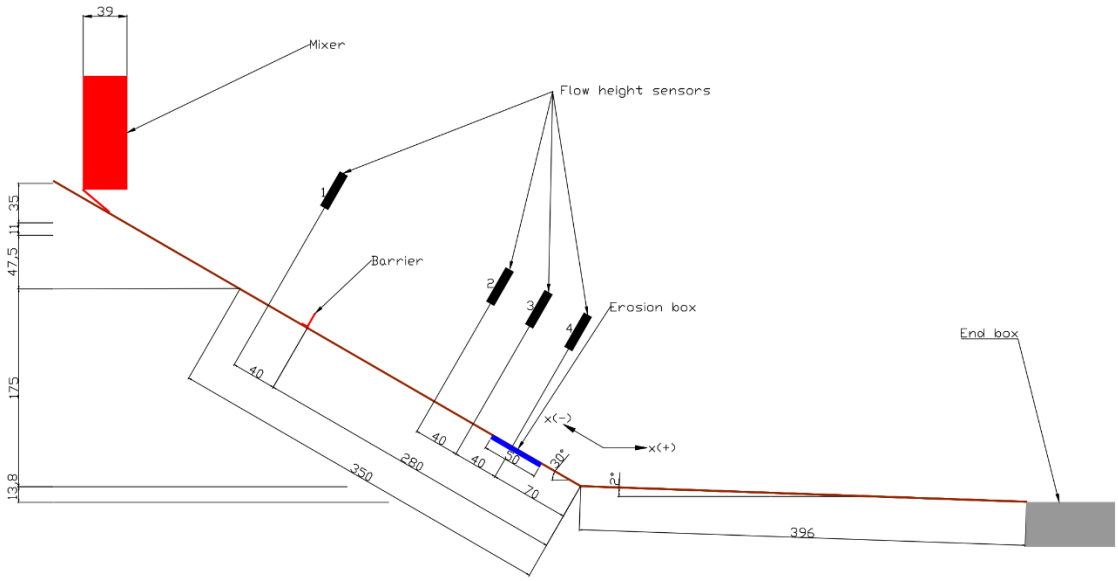

Figure 19 A principal drawing of the model in profile view. Dimensions are given in cm.

A considerable change from the tests conducted by Vicari (2018) to the model used in the specialization project of Teetzmann and Shrestha (2019), is the implementation of an erosion box in the channel. This box is placed from x = -0.4 m to x = -0.9 m in the channel. The aim of using this box, was to investigate the erosion happening during a debris flow. In each test, 12 columns of screws are fastened to the base of the box, containing 13 nuts each. In the tests, the erosion box is filled with bed material. The bed material is then added in layers, and loosely compacted. After the bed material is added, the screws are carefully removed, leaving 12 columns of 13 nuts in the soil. The nuts will after the passing of the debris flow, give an indication of how much erosion the bed material has experienced. The geometry of the erosion box is given in Figure 20. The height of this box is 40 mm, and the edge of the box is aligned with the channel base, so there will be no danger of the box interacting with the flow itself. The box is also taped along the edges to avoid any leakage or disturbance of the flow, see Figure 21.

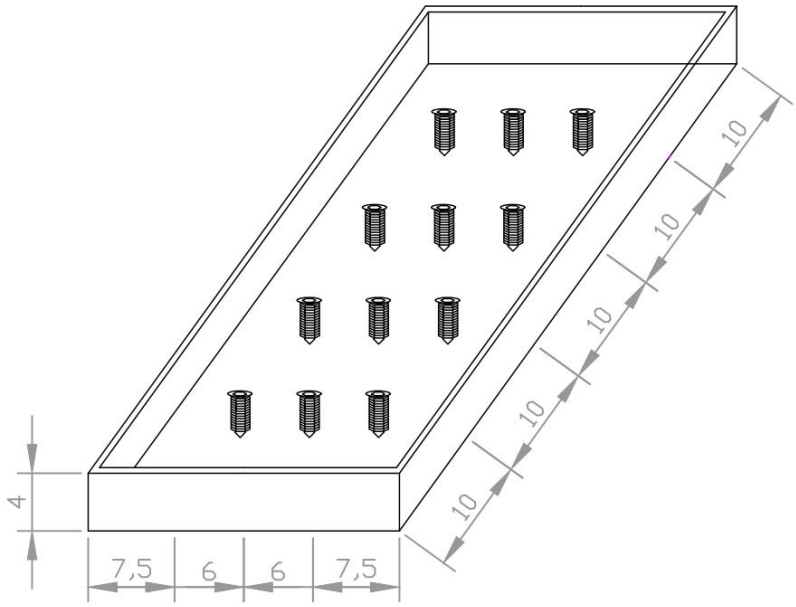

Figure 20 The erosion box consisting of 12 screws containing 13 nuts each, with the aim of recording the erosion in each test. Dimensions are given in cm.

Figure 21 Picture of the erosion box in place in the channel.

A barrier of 140 mm was made and was planned to place at a distance of x = -2.8 m from the end of the channelized flow zone, see Figure 19. This is an addition to the model compared to the model used in Teetzmann and Shrestha (2019) but was however never put in use due to the lockdown in March 2020. The barrier is designed such that it is

attached with two screws and can be dismounted. The geometry of the planned barrier can be obtained from Figure 22.

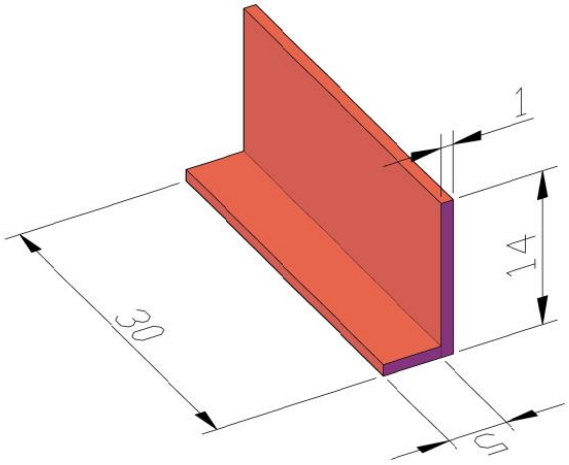

Figure 22 The barrier and its dimensions. The barrier was attached to the channel with two screws through the channel and into the channel base. Dimensions are given in cm.

Four flow height sensors were planned to be placed above the flume, numbered from 1 to 4 in Figure 19. The sensors are ultrasound sensors and give the opportunity to measure flow heights at wanted locations. The first sensor was planned to be placed prior to the location of the barrier at x = -3.2 m, to ensure low interference of flow height results with the mechanisms happening behind the barrier. The second and third sensors are already placed at x = -1.5 m and x = -1.1 m, where values of the flow heights are given after the ballistic flight of the material has ended and before the flow enters the erosion bed. The last sensor is located at x = -0.7 m, which gives values for the flow heights at the middle of the erosion box. The three last flow height sensors were also present in the experiments of Teetzmann and Shrestha (2019).

In addition to the flow height sensors, two different sets of cameras are used to describe the debris flow velocity and movement. Two GoPro cameras were planned to be used for the tracking of the velocity. The first GoPro camera was planned to overlook the barrier, hence giving the possibility to obtain the velocity coming into the barrier at the same location as the first flow height sensor gives the flow height. The second GoPro camera is placed in such a way, that it is possible to calculate the velocity at the same three locations as flow height sensors 2 to 4. This way the GoPro's and flow height sensor will act together in determining flow parameters at four different locations along the channel. The first GoPro location was planned to be added to the flume for the tests of this thesis.

In the tests of Teetzmann and Shrestha (2019) a high-speed camera was used to look at the shape of the debris flow travelling over the erodible bed. This gave indications on how the debris flow interacted with the bed material. For the use of the intermediate barrier, a second high-speed camera was planned to install to investigate the debris flow flowing over the barrier, how material is deposited behind the barrier and the launching of the debris into a ballistic flight.

The velocities are estimated by help of the Tracker software. Tacker is a video analysis and modelling tool, which can log a moving mass with help of a video shot by e.g. a GoPro camera. When the mass is logged, the software can return results on velocity and position. The setup of the software is shown in Figure 23, were the mass is tracked through the channel to obtain velocities for x =-1.5m. To obtain the results, the position

of the mass in time is tracked from x = -1.5 $\pm$ 0.2 m. This also yields for the other locations relevant for tracking mentioned earlier.

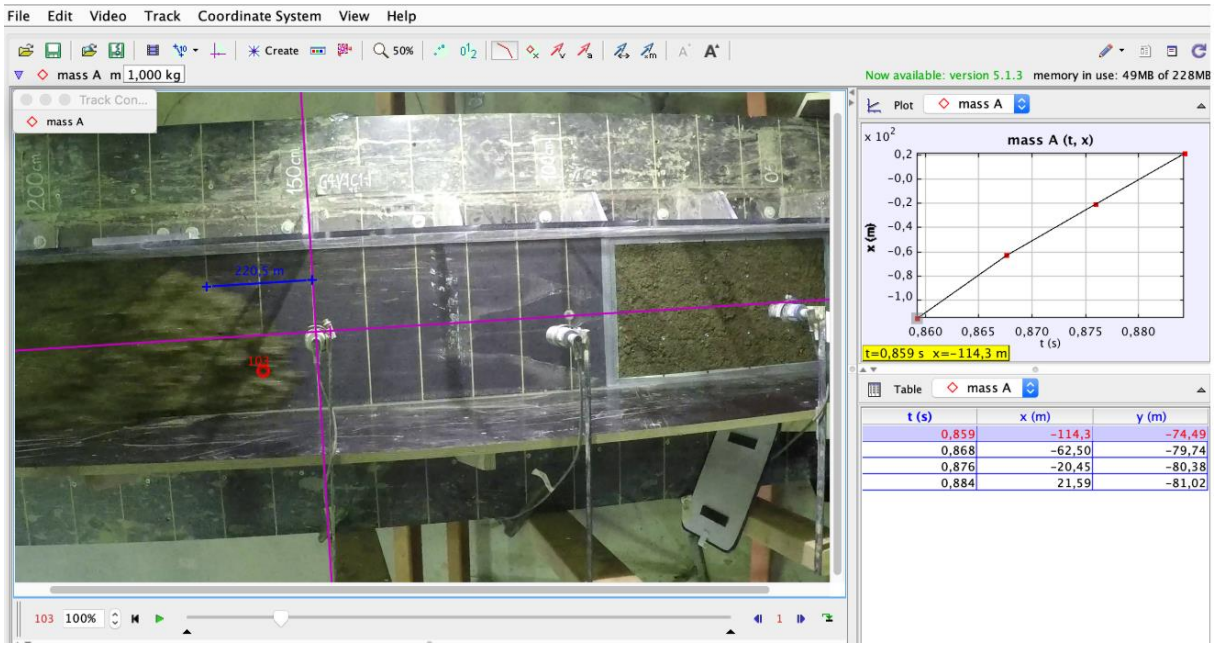

Figure 23 Setup of Tracker.

Figure 23 shows the tracking of the velocity for test done by Teetzmann and Shrestha (2019). These are also the tests that will be used as reference throughout this thesis.

The current model, and its dimensions are shown in Figure 24.

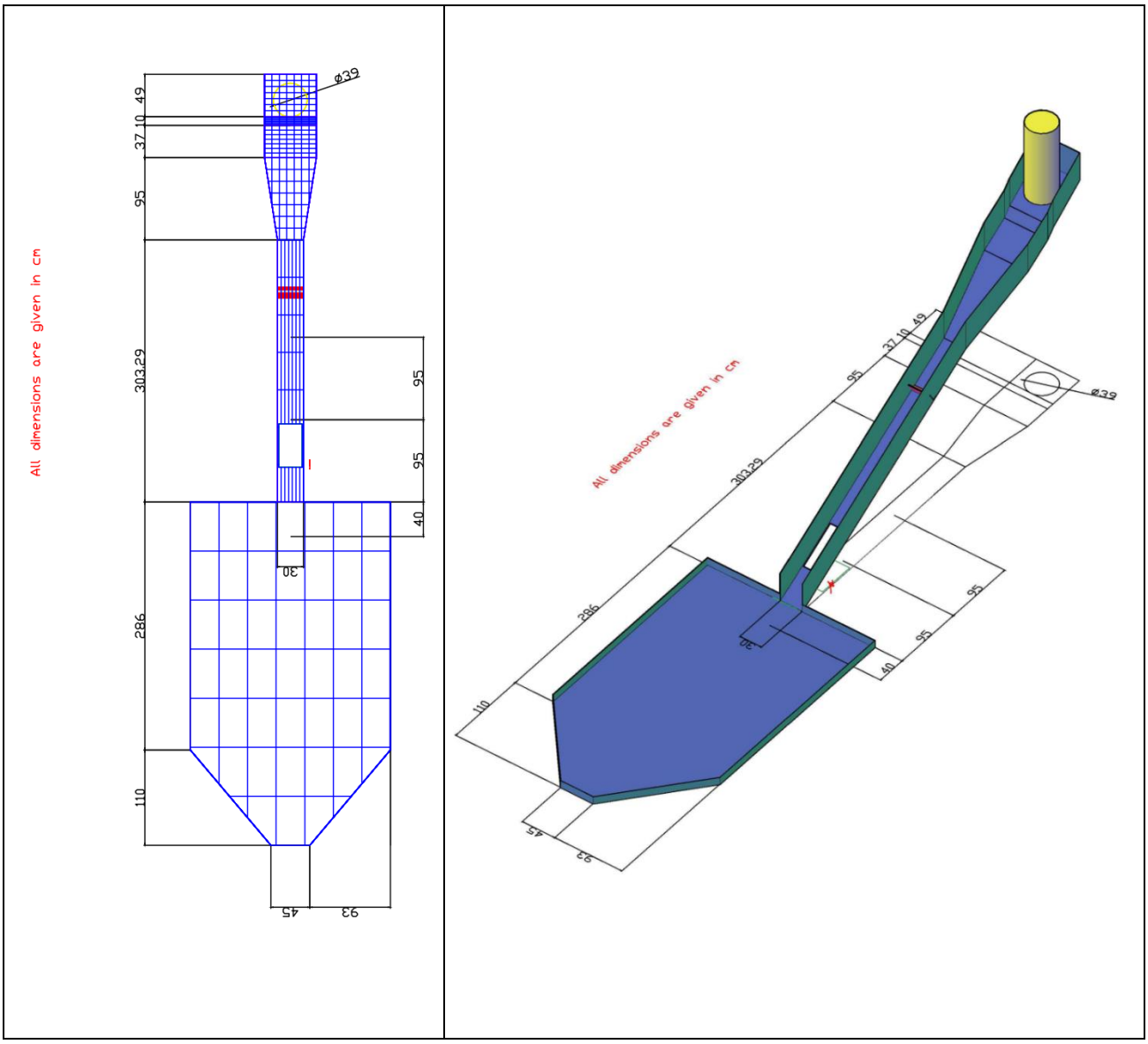

Figure 24 Dimensions of the current model shown from above and in 3D. The barrier is marked in red and the erosion box is seen as a hole in the channel. Barrier dimensions and erosion box dimensions are not given in this figure.

The test considered as reference has a release volume of 25 L and a slope angle of 30 °, the solid concentration is 60% and the debris material is the material G4 (Teetzmann & Shrestha, 2019). The test had four repetitions. The results of the reference tests are given in Teetzmann and Shrestha (2019) and key properties are repeated in Table 5.

Table 5 Key properties of reference test E7 (Teetzmann & Shrestha, 2019).

	x=-1.5 m			x=-1.1 m			x=-0.7 m		
Test number	Max flow height (mm)	Mean flow front velocity (m/s)	Froude number (-)	Max flow height (mm)	Mean flow front velocity (m/s)	Froude number (-)	Max flow height (mm)	Mean flow front velocity (m/s)	Froude number (-)
E7-r1	20.00	4.80	10.90	28.00	4.75	9.09	56.00	4.39	5.92
E7-r2	20.00	3.96	9.04	26.00	4.72	9.40	50.00	3.65	5.24
E7-r4	19.00	4.04	9.26	24.00	5.77	12.02	27.00	5.38	10.50
E7-r5	26.00	4.05	8.10	31.00	3.97	7.21	37.00	3.50	5.79

Flow heights in general are around 20-30 mm. Velocities are in general around 3-5 m/s. Froude numbers are quite high, but this is due to the small flow heights and large velocities. The flow heights increase again towards the end of the channel as material has been entrained.

3.2 Designing the barriers

In the design of the barrier for the model in section 3.1, the framework presented in section 2.4.2 is used (Koo et al., 2017; Kwan et al., 2015; Ng et al., 2019). For the design, different approaches of the flow interaction with the barrier were considered, using different flow velocities, impact reductions and angles of deposition.

The first model assumes that the first surge completely fills the dead zone behind the barrier and that the subsequent surges travel on this debris and launch into the ballistic flight, see Figure 25. The model also assumes that the deposition is entirely horizontal and thereby has a deposition angle, θ_d, of $30°$, which is equal to the slope angle. The apparent friction angle is assumed to be $10°$ for this material.

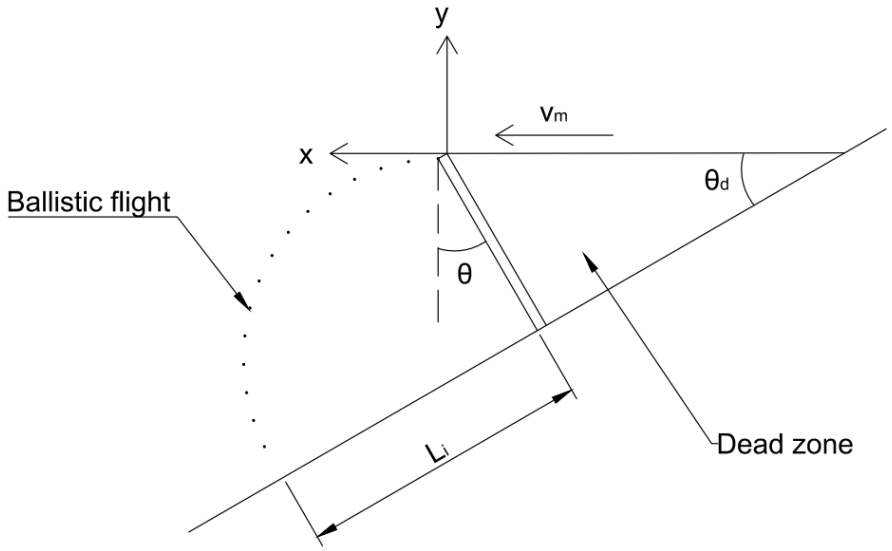

Figure 25 Filling of debris flow behind the barrier in the first model.

The second model uses the same assumption as the first one on the filling of the dead zone. The difference from this model to the one prior, is that it is here assumed that the deposition angle is equal to $40°$. This results in a net deposition angle, $\theta_d - \theta$, to be larger than zero ($10°$).

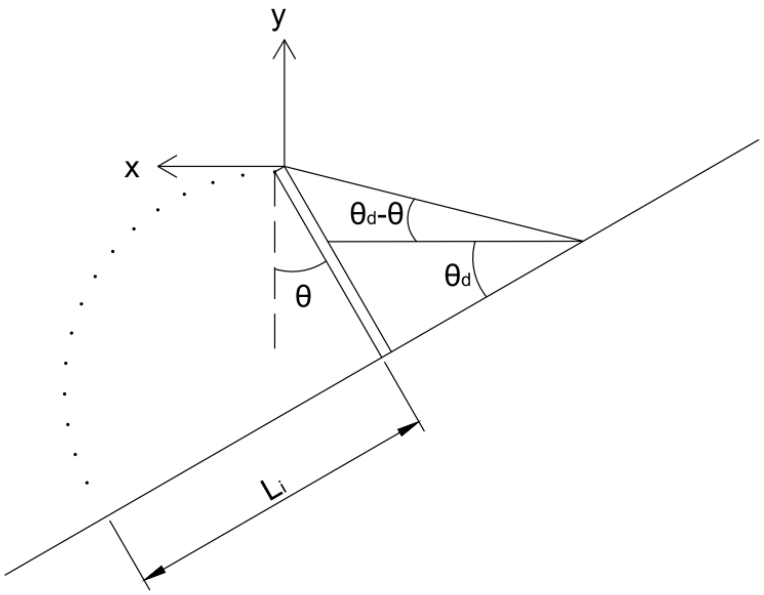

Figure 26 Filling of debris flow behind the barrier in the second model.

The third model is similar to the first as it uses one surge to fill the dead zone but uses a reduction factor to the initial velocity. The reduction factor is intended to cover the loss in velocity in different surges, due to two effects: the tail of the debris flow having a lower velocity, and the dissipation of energy during impact. The deposition angle and apparent friction angle are the same for this model as for the first.

The fourth model can be compared to the second one, since it uses the same deposition of debris and thereby the same net deposition angle. This model also includes the effect of velocity reduction due to flow characteristics and dissipation of energy during impact. Hence, the net deposition angle is set to $10°$ and the velocity of the second surge is reduced by 30 %.

Lastly, the dead zone was investigated to be filled incrementally. This process was looked at by an incremental procedure using MATLAB and letting the flow fill up the barrier incrementally while still using a reduction factor to the velocity. In this case, the barrier was filled after a set of surges.

Table 6 The table gives the different variations used in each approach.

Model	**Reduction factor of free-flow velocity**	**Apparent friction angle, φ_a**	**Slope angle. θ**	**Attenuation angle, θ_d**	**Net deposition angle, $\theta_d - \theta$**
1	1.0	10	30	30	0
2	1.0	10	30	40	10
3	0.7	10	30	30	0
4	0.7	10	30	40	10

After considering all options, model 4 seemed as the most plausible method for estimating the run-up velocity. It took account for a deviation from the horizontal for the deposition in the dead zone, while at the same time taking account for the reduction in velocity due to variations in the flow and impact of the barrier. Based on the chosen model, the parameters were used in the framework presented earlier and the dimensions were set to the dimensions shown in Figure 22 in section 3.1.

4 Numerical simulations

This chapter explains how the numerical model is set up and how the simulations are performed. This includes the definition of the earth pressure coefficients by using different approaches. The reference case presented from the physical experiments of Teetzmann and Shrestha (2019) serves as indications on expected values for the flow height, velocity and Froude number for this kind of model.

4.1 Setup of the simulations

The RAMMS setup is established based on the real laboratory model described in section 3.1. One of the tests performed by Teetzmann and Shrestha (2019) is used as the reference case for the simulations. The reference case considers an erosion bed which is not modelled here but will be discussed more in detail later in this section. Tabulated data for the reference test is obtained in Table 5 in section 3.1.

RAMMS processes topographical data through a digital elevation model (DEM). This terrain model is made in Excel in an ESRI ASCII format. The different cells in this grid represent different heights at corresponding x and y coordinates, see Figure 27. The points in the grid all have 1 cm to the next point, but the grid cells are converted to meters as this is the operational unit of RAMMS. The top of the DEM file contains a header defining the properties of the file.

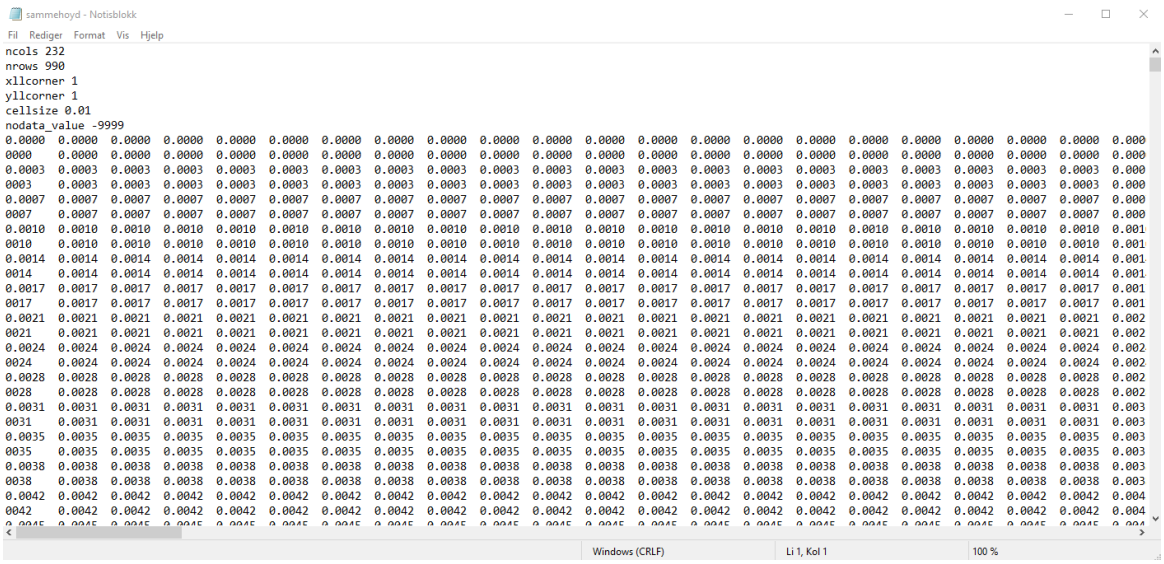

Figure 27 An excerpt from the DEM as an ESRI ASCII grid.

Once the DEM is imported into RAMMS, the outer walls of the model are made with the dam function in RAMMS. The walls that make out the edges of the model, are easiest produced with help of the module that lets the user draw a polygon shape file. The geometry of the walls is approximately drawn in RAMMS and opened in QGIS (version 3.12.1-Bucuresti), where the polygon is modified to the exact shape of the flume, see Figure 28. This shapefile is then imported back into RAMMS and added to the terrain model with a height of 40 cm in the simulations and used as a dam file modelling the side of the flume. Some important notes on this dam file are:

- A simplification on the shape at the end of the runout zone is made, as can be seen from comparing Figure 24 in the previous section and Figure 28. The shape of the end of the runout zone is not inclined in the xy- direction as in the true model but made with perpendicular edges.
- The end of the runout zone has in the physical model an opening where the leftover debris that is not deposited can flow into a box but in the numerical model, this edge is enclosed. This makes the debris flow crash into the wall if runout is too large.

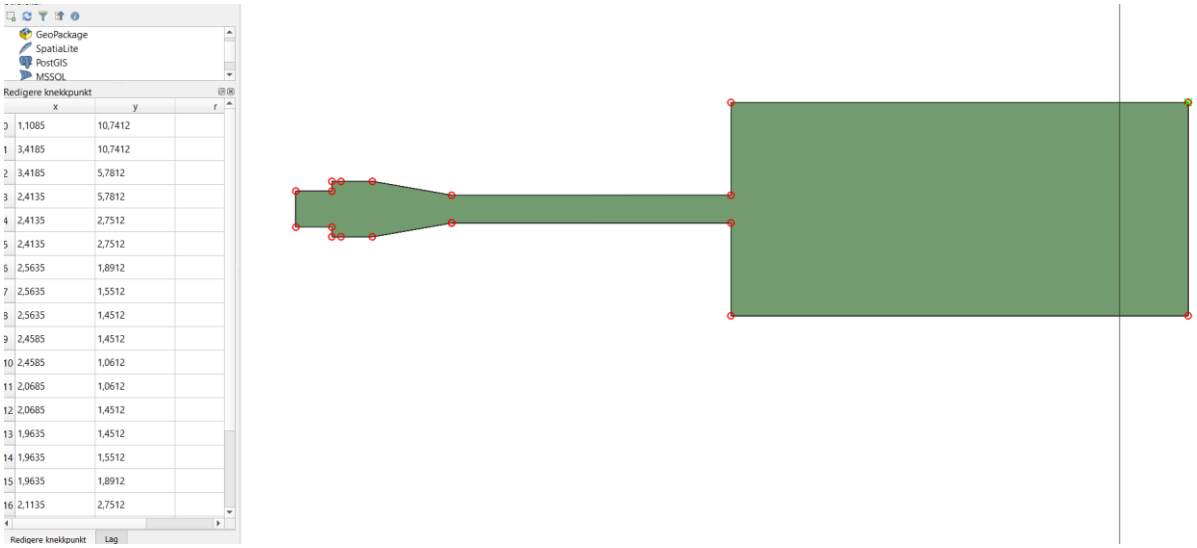

Figure 28 The modelling of the dam file in QGIS.

RAMMS also needs input on the release mechanisms of the debris flows. The release information is set to a block release or release area. This will then illustrate the area where the debris flow is leaving the mixer of the lab tests (Teetzmann & Shrestha, 2019; Vicari, 2018). The true mechanism of the release from the mixer is not possible to model with RAMMS, and there are hence made simplifications to the real model first described in Vicari (2018).

The first simplification is that the released volume is dropped from a given height. RAMMS will simulate the release as a collapse of the entire debris flow volume, resulting in all the material starting to flow at once and not by moving its way through the cylindrical mixer. When the material is dropped from a height, the same assumption is made as in Vicari (2018), that this will lead to a loss of energy upon impact with the flume, and that the effect of this is negligible. The flow itself will have the same volume and behavior when it is fully developed and will not be influenced by the block release.

The second simplification is that the area of release is simplified to have a square shape. The release area is hence set to be a square with sides equal to 39 cm. This is not consistent with the circular form of the cylinder. As stated in the prior, the release mechanism will lead to energy loss, and the effect of the shape of the release area is considered minor. To ensure that there is sufficient spacing between the dam walls at the top and the release, the real square area that gives the release volume is set to 37 by 37 cm. Also, too large spacing between dam walls and the square block release is not wanted as it will result in a large splash at the top, dissipating a lot of energy in the release mechanism, which is not consistent with the mixer cylinder release mechanism in the physical model.

In the reference test in section 3.1, the release volume is 25 L (0.025 m^3) on the $30°$ flume. As RAMMS uses the inclined area of the block release on the slope and multiplies this with the release height to obtain release volume in the modelling (Vicari, 2018), the release height can be calculated based on a wanted release volume:

$$h_{release} = \frac{V_{release}}{A_{release}}$$

The inclined release area is given as 37 cm by 37/(cos(35.5°)=45.45 m, which results in an area of approximately 1682 cm^2. For a release volume of 0.025 m^3 and an inclined area of release of 0,168 m^2, the release height turns out to be 0.149 m. RAMMS considers only two decimal numbers, so the release height is hence set to 0.15 m.

The final outline of the model in RAMMS can be seen from Figure 29. In the figure the outer walls, together with the release volume is modelled. The outer walls on the top are made narrower to reduce the splashing and energy dissipation as there is less room. As the debris flow is then forced to travel down, more energy is transferred to the flow itself.

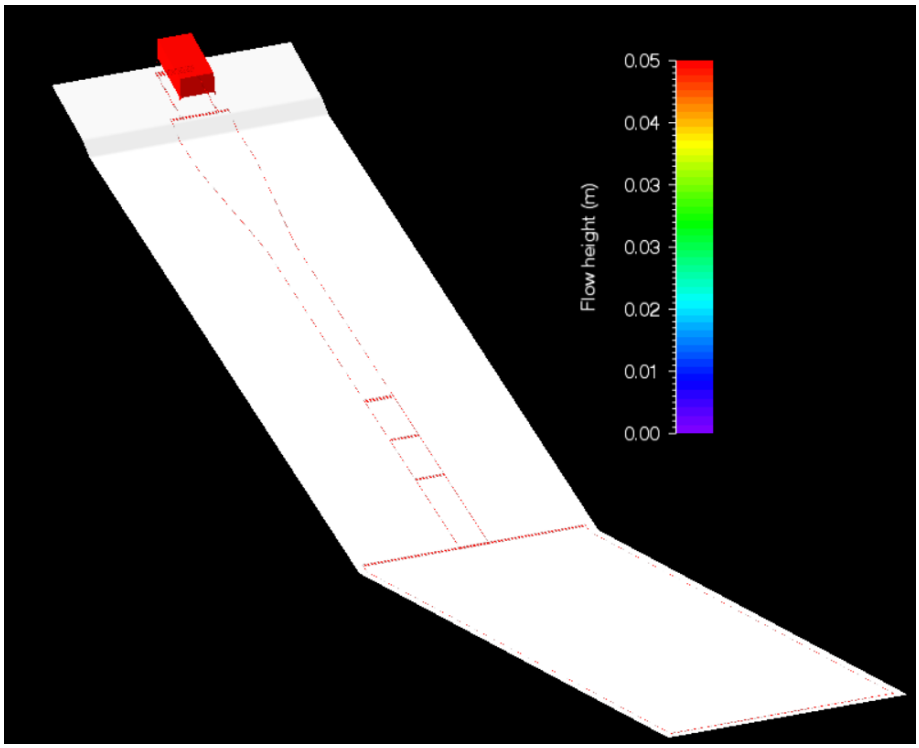

Figure 29 3D view of the model in RAMMS with the 39 by 39 cm release square at the top.

The erosion box which is put into the real physical model is not considered for the numerical modelling. The effect of erosion in the box of bed material is considered small for the numerical simulations, since amount of bed material is small. Therefore, it is assumed that the contribution of the bed material of the box is negligible to flow height and velocity in the simulations. Also, all values prior to the box are unaffected by the erosion. Values obtained in the experiments of Teetzmann and Shrestha (2019) may hence still be used to compare results of the numerical simulations.

The runout part of this numerical model is made one meter longer than the true model and prior numerical models. This is because when investigating the runout shapes the

runout of the flow is not wanted to interact with the end wall. This way it is wanted to prevent that the deposit is not hindered by the walls at the end of the flume.

4.2 Simulation input parameters

When running the RAMMS simulation, several different parameters are required. The parameters are given in Table 7 below, with a short description.

Table 7 RAMMS input parameters

Parameter	Value	Description
Simulation parameters		
Simulation resolution (m)	0.01 m	The 1 cm grid is given from DEM.
End time (s)	Default value of 1000 s	End time of simulation. Is not changed since simulation time is way less (10 s).
Dump-step (s)	0.1 s	Gives the definition of the resolution of the animation of the results. Need to have a small time steps for these tests. This has no effect on the simulation results.
Density (kg/m^3)	Default value of 2000 kg/m^3.	RAMMS suggests keeping the default value if no further information on the debris flow material is available.
Lambda (λ)	Varies	Modifies the pressure gradients that is driving the debris flow. If set equal to one the effect of this parameter is disabled. If different from one, 1st order numerical scheme must be used. It is not recommended to use a λ different from 1.
Numerical parameters		
Numerical scheme	1st /2nd order	The order of the numerical solver, where 2nd order provides more accurate solutions than 1st.
Null height cutoff (m)	0.000001 m	The unrealistically shallow flow heights are eliminated from the simulation in order to reduce numerical errors.
Voellmy friction parameters		

μ	Varies	A Coulomb type of friction parameter. Values normally range between 0.05 and 0.4. Can initially be set as tan(slope angle).
ξ	Varies	A turbulent drag friction parameter.

Yield stress is set to zero in these simulations as the effects of this parameter is not wanted to investigate. The entire area is set for one value of μ and one value of ξ.

The simulations stopping criteria in RAMMS is based on the momentum. For each dump-step, the momentum of all cells in the grid is summarized and compared with the sum of the maximum momentum. A user defined stop parameter giving a percentage of total momentum is used to compare to the maximum momentum. When the maximum momentum is less than the threshold value, RAMMS considers the debris flow as stopped. According to information given in the program, a reasonable value of this stop parameter is 1-10 % of the total momentum. In the simulations the stopping criteria was set to 5 %.

Even though it is recommended by RAMMS to leave the active-passive earth pressure coefficient, λ, equal to the default value of 1, it is possible to change the value of this parameter. The results of the simulations are greatly influenced by the change of λ (Bartelt et al., 2017). RAMMS lets the user define a constant value of lambda throughout a simulation. Behavior can both be dilatant or compressive dependent on the gradient of the velocity. When $\lambda < 1$, the earth pressure coefficient is active, which would correspond with a dilatant flow behavior. For $\lambda > 1$ the earth pressure coefficient is passive which in turn corresponds to a compressive flow behavior. To model the same event with a different λ, it is often required to recalibrate the two Voellmy parameters, μ and ξ. When λ is different from 1, numerical instabilities can occur. These instabilities can become visible as oscillations of velocities from one cell to the next or unforeseen changes in the debris flow volume over a simulation. In order to use a λ different from 1, RAMMS recommends using first order numerical scheme which are found to cause more stable solutions. The software automatically locks to a first order numerical scheme as $\lambda \neq 1.0$.

The Voellmy friction parameters, μ and ξ, need to be calibrated to ensure that they are back calculating the event of interest. The values of μ and ξ are kept constant through a simulation but can be changed between simulations.

4.3 Earth pressure coefficients

In these tests, there was no possibility of obtaining the basal friction angle (δ_1) and the internal friction angle (φ), by experimental testing due to the ongoing Covid-19 crisis. Therefore, values for the parameters given in Gray et al. (1999) and Iverson and Denlinger (2001) have been used to be able to calculate the earth pressure coefficients for the simulations.

Two values of the internal friction angle and one bed friction angle are used. The basal friction angle, $\delta_1 = 30°$, and the internal friction angles, $\varphi = 30°$ or $\varphi = 40°$, are used to calculate the earth pressure coefficients. The value of the internal friction angle also fit into the range of common values presented by Iverson (1997b) given in section 2.3.5

and match the value of the internal friction angle in the USGS flume experiments also mentioned in section 2.3.5. One could also argue to use a lower value for the friction angles considering the effects of a very smooth surface on which the debris flow slides. Based on the values provided by Gray et al. (1999) the values remain as stated.

Based on these friction angles, the earth pressure coefficients are calculated as described in section 2.6 for both classical Rankine theory (only requires the internal friction angle) and formulas proposed by Savage and Hutter (1989) (requires both internal and basal friction angle). RAMMS is only able to take one constant λ in the longitudinal and cross-slope direction. Hence, the active and passive coefficients in the x- and y-direction are given simultaneously. The coefficients are presented in Table 8. One additional coefficient of $\lambda = 2.0$ is added, to better understand the trends of the effects of the earth pressure coefficients.

Table 8 Earth pressure coefficients for the simulations in RAMMS, with $\delta = 30°$ and $\varphi = 40°$. Rankine theory is addition tested for internal friction angle $\varphi = 40°$.

Earth pressure coefficient, λ	**Value**	φ	δ_1	**Stress state**	**Calculation method**
K	1.00	-	-	Isotropic	(Savage & Hutter, 1989)
K_a	0.22	40°	-	Active	Rankine theory, given in Schraml et al. (2015)
K_a	0.33	30°	-	Active	Rankine theory, given in Schraml et al. (2015)
K_a	0.82	40°	30°	Active	(Savage & Hutter, 1989)
K_p	2.0	-	-	Passive	-
K_p	3.0	30°	-	Passive	Rankine theory, given in Schraml et al. (2015)
K_p	4.0	40°	30°	Passive	(Savage & Hutter, 1989)
K_p	4.60	40°	-	Passive	Rankine theory, given in Schraml et al. (2015)

4.4 Simulation procedure

Several simulations are run to establish a basis for scrutinizing the effect of the earth pressure coefficient on the debris flow runout shape, runout length, velocity, flow height and stresses. The simulation scheme is shown in Table 9. For each value of μ and ξ a simulation is run for every active, passive and isotropic earth pressure coefficient, λ, in Table 8. This results in 81 numerical simulations in total. With investigating different values of μ and ξ, it is possible to check if the variations in behavior of the debris flow due to of λ are consistent with changing μ and ξ. Values set for λ remain constant in time and direction throughout the entire simulation domain. In addition, some extra simulations are run on a $17.5°$ slope to look at the differences in the effect of λ on runout shape of a steeper or gentler slope.

Table 9 Simulation scheme.

	1	**2**	**3**	**4**	**5**	**6**	**7**	**8**	**9**
μ **(-)**	0.03	0.03	0.03	0.05	0.05	0.05	0.08	0.08	0.08
ξ **(m/s²)**	500	1000	1500	500	1000	1500	500	1000	1500

In each test, flow height, velocity, runout shape and runout distance are recorded. The same procedure is followed for all numerical simulations to obtain comparable results. Results for flow height and velocity are logged for three different key locations: x = -0.7 m, x = -1.1 m and x = -1.5 m. This is because these key locations are logged in the physical tests of Teetzmann and Shrestha (2019) which are used as the reference case of these numerical simulations. In addition to the flow heights and velocities at these locations, the runout length and shape is considered. Examples of how the results are logged for each simulation are shown in Figure 30 to Figure 32.

The flow heights at the different locations are logged as maximum flow heights at the given location and as a time plot of the flow heights at this location. An example of this time plot is given in Figure 30.

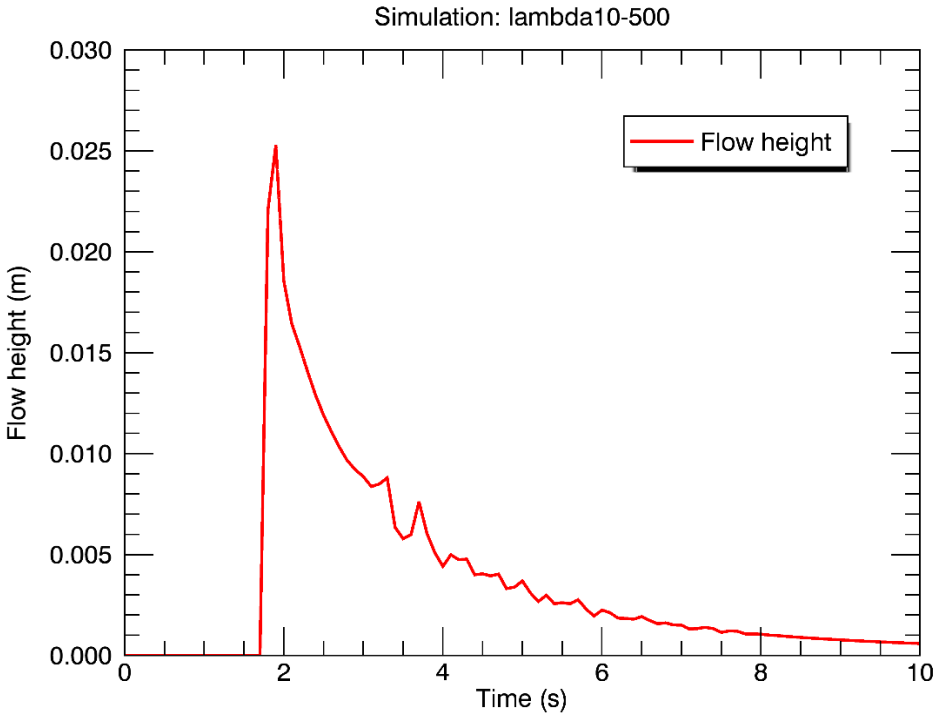

Figure 30 Time plot of the flow heights for x = -0.7 m when λ = 1.0 and parameters μ = 0.08 and ξ = 500 m/s². Numerical scheme is second order.

The velocities of each simulation are also logged at each location as a max velocity value at a given time and a time plot of the velocities at the location. Figure 31 shows an example of the time plot of the velocities of a simulation.

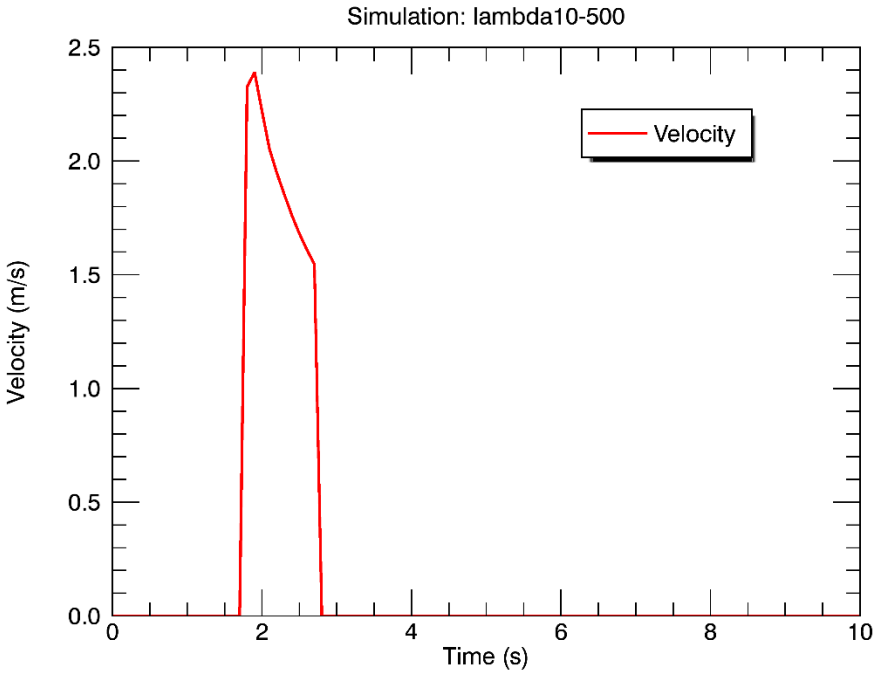

Figure 31 Time plot of velocities at x = -0.7 m for λ = 1.0 and a second order numerical scheme. The values of μ and ξ are set to 0.08 and 500 respectively for this simulation.

The plot in Figure 32 is used to estimate the runout length for each simulation. The plot is calculated by RAMMS as a result of drawing a line profile through the runout zone from the start of the deposition zone past the end of the debris flow runout.

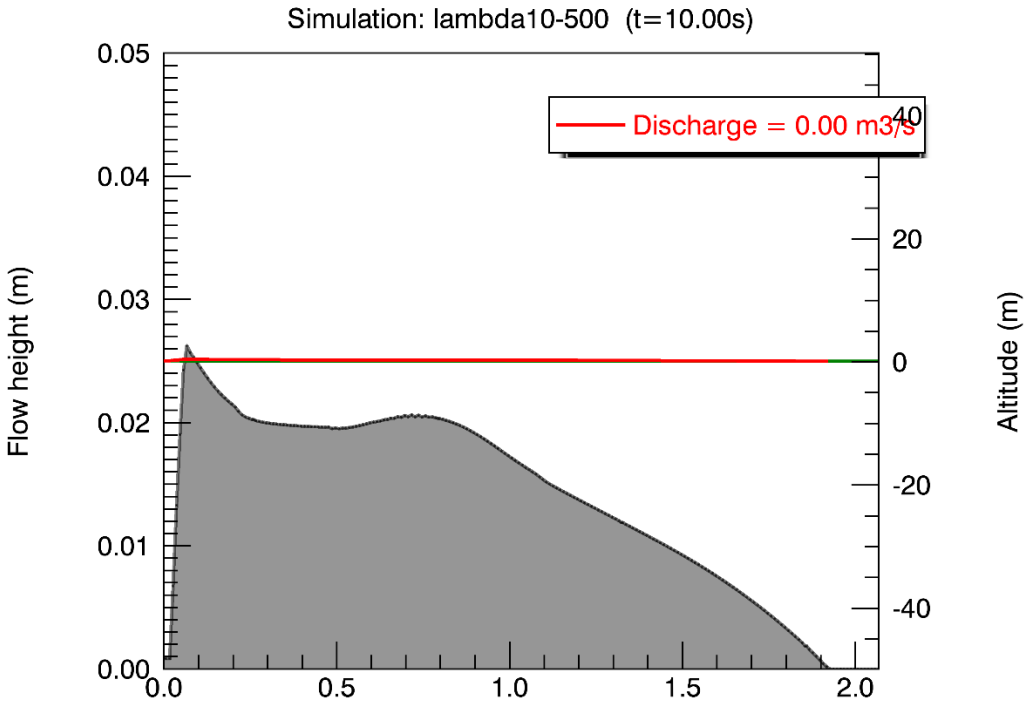

Figure 32 Line plot through the runout showing the runout length and flow height. The λ value is 1.0 and Voellemy friction parameters are set μ = 0.08 and ξ = 500. In this simulation a second order numerical scheme is used.

Deposition shape is exported as a polygon file to QGIS and then compared by adding different layers on top of each other for the simulations with different λ. An example of this is shown in Figure 33 for the active and passive values of the Savage and Hutter theory (Savage & Hutter, 1989).

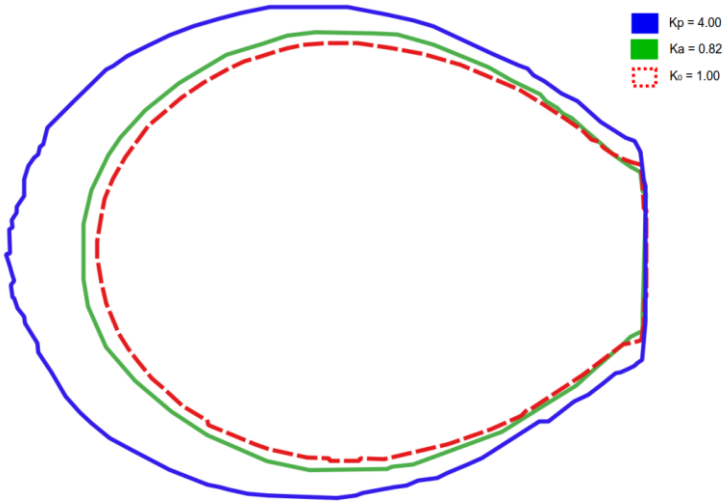

Figure 33 Outline of deposition for earth pressure values of Savage and Hutter theory (1989), $\mu = 0.05$ *and* $\xi = 500\, m/s^2$.

How the flow behavior changes based on the different earth pressure coefficients in the flume can be investigated by looking at the Froude numbers. The Froude number is given in section 2.3.4. The velocities and heights used to calculate the Froude number, are the maximum velocities and heights in the middle of the channel at x=-1.1 m and x=-1.5 m.

A crucial concern when picking the points for flow height and velocity values at the points of interests is that: animation quality gets poorer as a result of using $\lambda \neq 1.0$. This is especially the case for the active pressure coefficients. As animation quality gets poorer, the deviations in velocity and flow height from one point to the adjoining one can be large, due to numerical instabilities. Hence, great care should be taken when picking this point in simulation. It was here tried to do all measurements of this in the middle of the channel, but if the animation produced large oscillations, the point was moved only slightly to the right or left of the mid-point of the channel to obtain more consistent results.

The Voellmy friction parameters need to be recalibrated for a change of earth pressure coefficient. Hence, if the aim is to model the best fit parameters, μ and ξ need to be recalibrated for each value of λ.

5 Results

This section presents the results obtained from numerical modelling. The focus in this section is to scrutinize the effects of the earth pressure coefficient on debris flow behavior. This is done by looking at the debris flow height, velocity, runout distance and shape, and in addition at the Froude number. Flow height, velocity and Froude number are investigated in the channel. Runout distance and runout shape is investigated by assessing the debris flow deposition area. The aim of this chapter is to describe the obtained results. Chapter 6 discusses the results more in detail.

The difference in first and second order numerical scheme was looked at for every simulation, but only first order simulation scheme is presented for the isotropic earth pressure coefficient of $\lambda = 1.0$. This is because any earth pressure coefficient $\lambda \neq 1.0$ can only be run on a first order numerical scheme. For some simulations the effects of changing the numerical scheme are small, while for others the deviations are larger. Flow heights and velocities are larger for first order numerical scheme except for a few cases. For the most of these cases where the difference is small, results for the flow heights are around the same values, meaning that there is not much difference in results depending on the first and second order scheme. This hence shows that that first order numerical scheme may overestimate the results.

Results are discussed for the location x=-1.1 m and x=-1.5 m as these locations are unaffected by the erosion in the physical experiments and flow heights, velocities and Froude numbers are comparable for this location for the numerical simulation. Velocities and flow heights are also investigated for a later point in the channel, x=-0.7 m, but the effect of this position is considered solely for the effect on the runout. The graphs of these are presented in the Appendix. In all cases, the variations in the effect due to $\lambda \neq 1.0$ may change a lot depending on the different rheology parameters μ and ξ. Therefore, different configurations of these Voellmy rheology parameters are investigated.

5.1 Flow heights

The plots in Figure 34 to Figure 45, show the results of the flow heights from the simulations. Results of the flow height are considered for the earth pressure coefficient λ associated with the active, passive and isotropic stress state in the flume. The simulation scheme in Table 9 is followed and run for all values of λ for every combination of μ and ξ. Both μ and ξ are kept constant in turn to investigate if effects of the earth pressure coefficients on the behavior remain the same when changing the rheology parameters. The results in Figure 34 to Figure 36 and Figure 40 to Figure 42 below are shown for a constant μ while ξ varies at x=-1.1 m and x=-1.5 m respectively. Results in Figure 37 to Figure 39 and Figure 43 to Figure 45 are shown for a constant value of ξ while μ is varied.

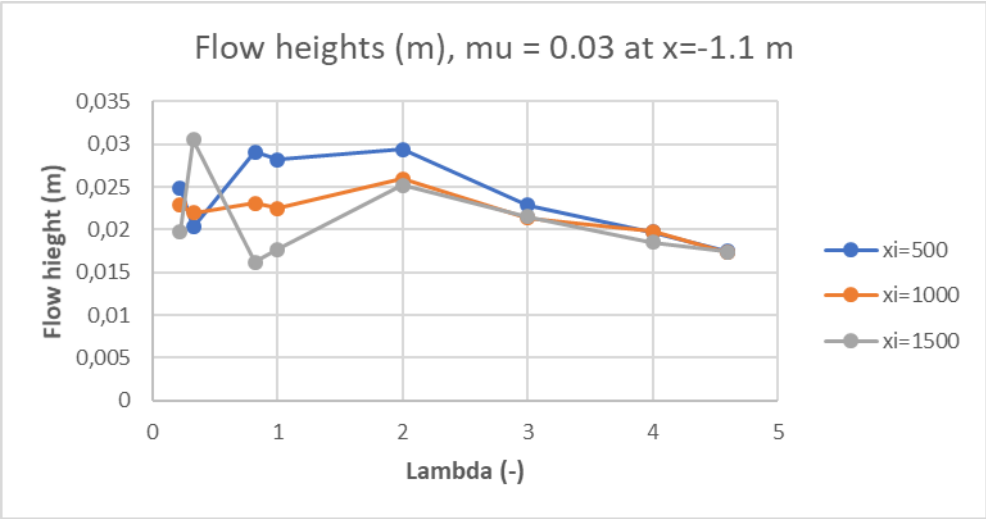

Figure 34 Flow heights at x=-1.1 m when $\mu = 0.03$ *and* ξ *is varied between* 500 *and* $1500\ m/s^2$.

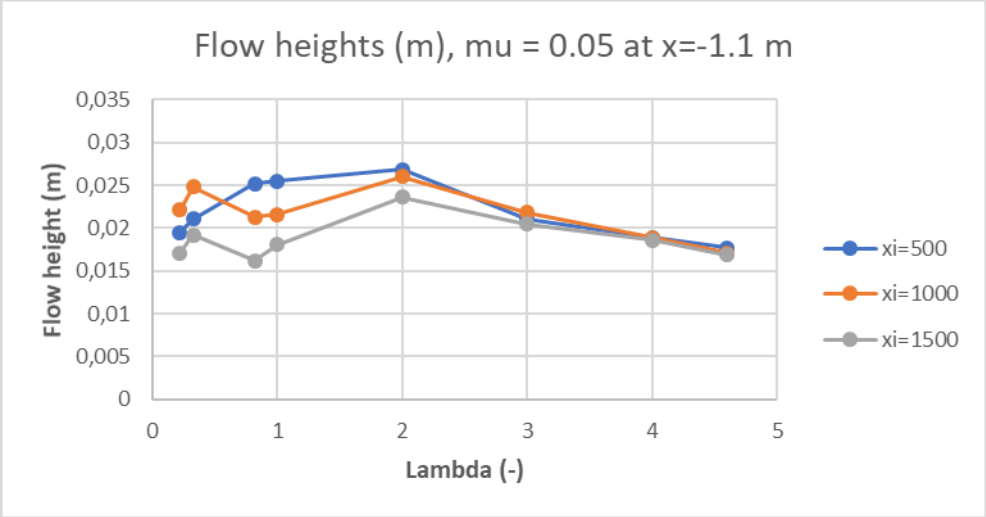

Figure 35 Flow heights at x=-1.1 m when $\mu = 0.05$ *and* ξ *is varied between* 500 *and* $1500\ m/s^2$.

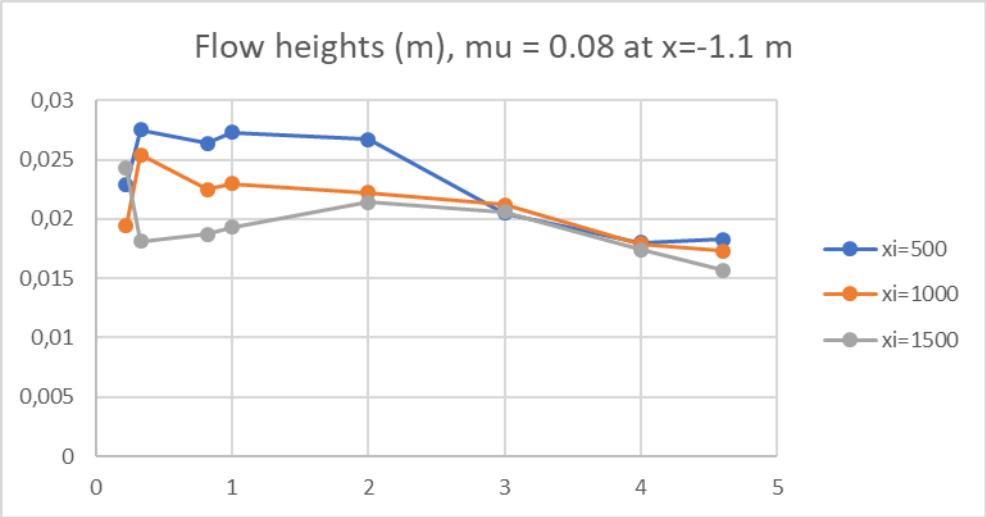

Figure 36 Flow heights at x=-1.1 m when $\mu = 0.08$ *and* ξ *is varied between* 500 *and* $1500\ m/s^2$.

The different values of the turbulence parameter ξ cause the flow heights to shift slightly for every value of μ at x = -1.1 m when the earth pressure coefficient, λ, is equal to 1.0 and flow is isotropic, see Figure 34 to Figure 36. Hence, increasing the value of ξ results in a slight decrease of the flow heights for the isotropic stress state. From Figure 37 to Figure 39 it can be obtained that there is little change in the flow heights dependent on different μ for $\lambda = 1.0$ at x = -1.1 m.

As the value of the λ increases to a passive value of $\lambda > 1.0$, the effect of the turbulent friction parameter ξ on the flow heights is reduced. And as the earth pressure coefficient increases beyond $\lambda = 2.0$, the flow heights at different values of ξ start to approach one another. From $\lambda = 3.0$, flow heights are near to independent of ξ. The curves of the flow heights are relatively close all the way from $\lambda = 1.0$ to the highest passive value in Figure 37 to Figure 39, showing that μ has little impact on flow heights and that this is little affected by the passive earth pressure coefficient. Largest deviations for the flow heights as μ varies is found at $\lambda = 2.0$.

The overall effect of the passive earth pressure coefficient $\lambda > 1.0$, is that flow heights are decreased as a result of λ increasing. This overall decrease happens independent of the values of both μ and ξ. Initially, the flow heights increase slightly compared with the isotropic state as λ turns passive. However, from $\lambda = 2.0$, flow heights are reduced at a steady rate. For the highest value of λ simulated here, the curve gives little indication of flattening out. The reduction is therefore assumed prolonged with an increasing value of λ-passive. This behavior can be seen for all positions in the channel.

When the values of the earth pressure coefficient become active, $\lambda < 1.0$, the trend on the flow height is not as clearly defined as for the passive case. The behavior changes for the different locations in the channel and for different values of ξ and μ. Different locations in the channel exhibit different patterns of the flow height dependent on the variation of the active λ.

From Figure 37 to Figure 39 it is obtained that at x = -1.1 m, when $\xi = 500\, m/s^2$, the overall effect on the active earth pressure coefficients as λ gets smaller, is a reduction of the flow heights. The reduction becomes steeper for lower values of μ. For $\xi = 1000\, m/s^2$, the effect of λ-active is less and the curves of the flow heights in Figure 38 are flatter. As ξ is increased to $1500\, m/s^2$ in Figure 39 however, the effect of the active earth pressure coefficient, as λ gets smaller, looks to increase the flow heights.

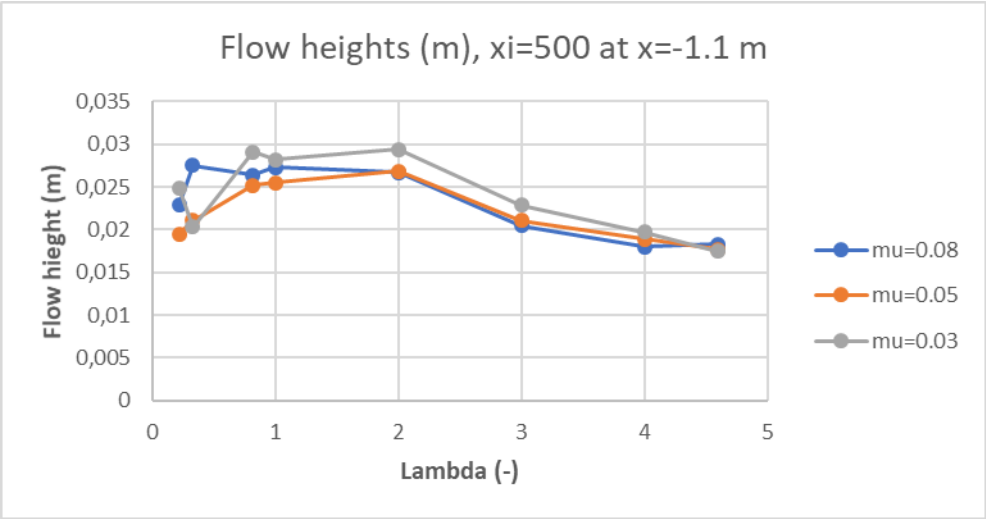

Figure 37 Flow heights at x=-1.1 m when $\xi = 500\, m/s^2$ and μ is varied between 0.03 and 0.08.

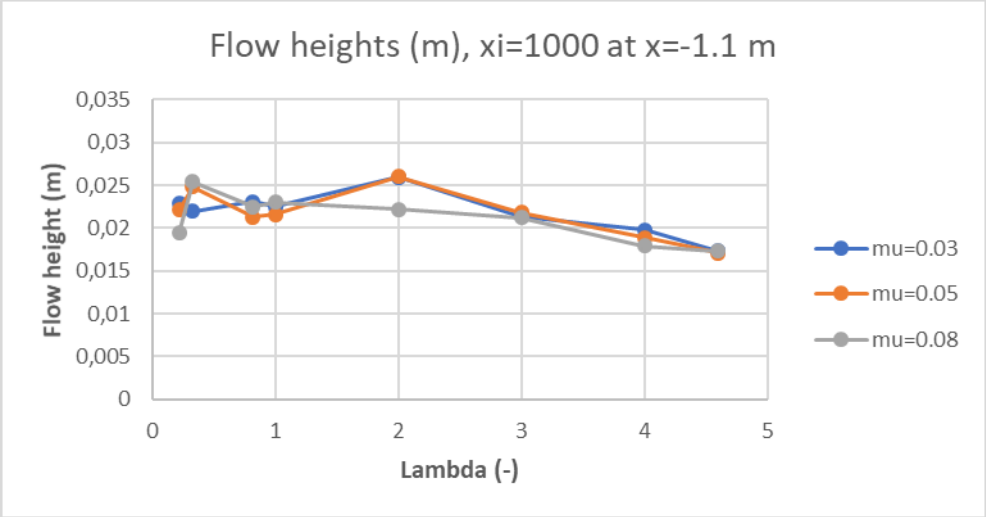

Figure 38 Flow heights at x=-1.1 m when $\xi = 1000\, m/s^2$ and μ is varied between 0.03 and 0.08.

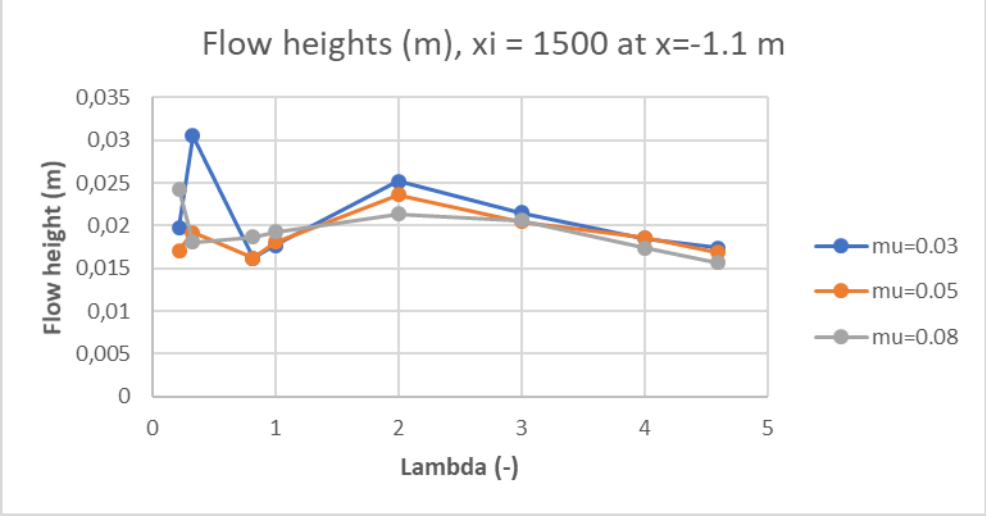

Figure 39 Flow heights at x=-1.1 m when $\xi = 1500\, m/s^2$ and μ is varied between 0.03 and 0.08.

Earlier in the channel, at x = -1.5 m, the same behavior can be spotted for the passive values as for x = -1.1 m. From the passive earth pressure coefficient, $\lambda = 3.0$, there is little effect of changing values of the parameter ξ. The effects of λ however seem to get smaller with an increasing μ, see Figure 40 to Figure 42. As μ is increased, the gap between the curves of changing ξ values is enlarged. The strong convergence effect induced by passive values of λ shown for x = -1.1 m in the figures above, is somewhat reduced. The convergence of the flow heights due to the passive values is still obtained this early in the channel however, but to a lesser extent. Flow heights do also here decrease in general as a result of a passive earth pressure coefficient.

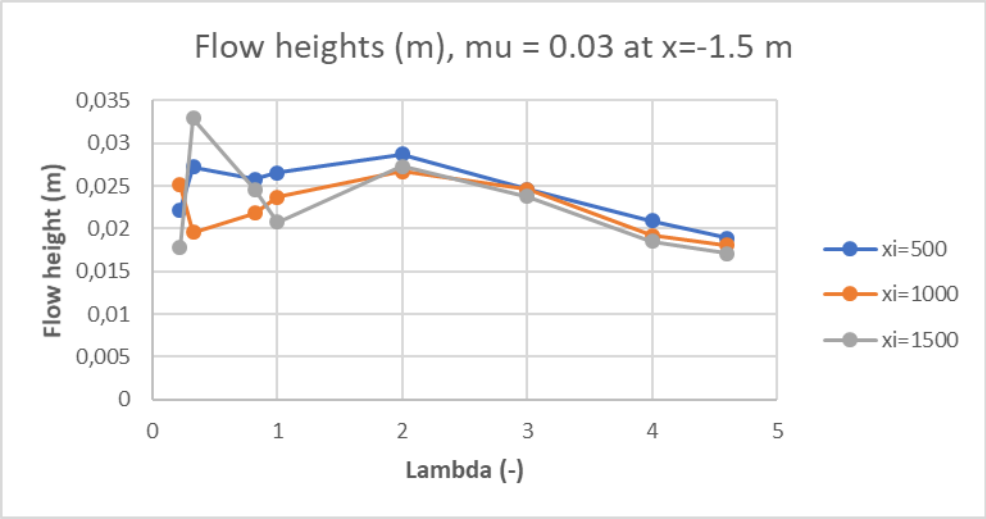

Figure 40 Flow heights at x=-1.5 m when $\mu = 0.03$ and ξ is varied between 500 and $1500\ m/s^2$.

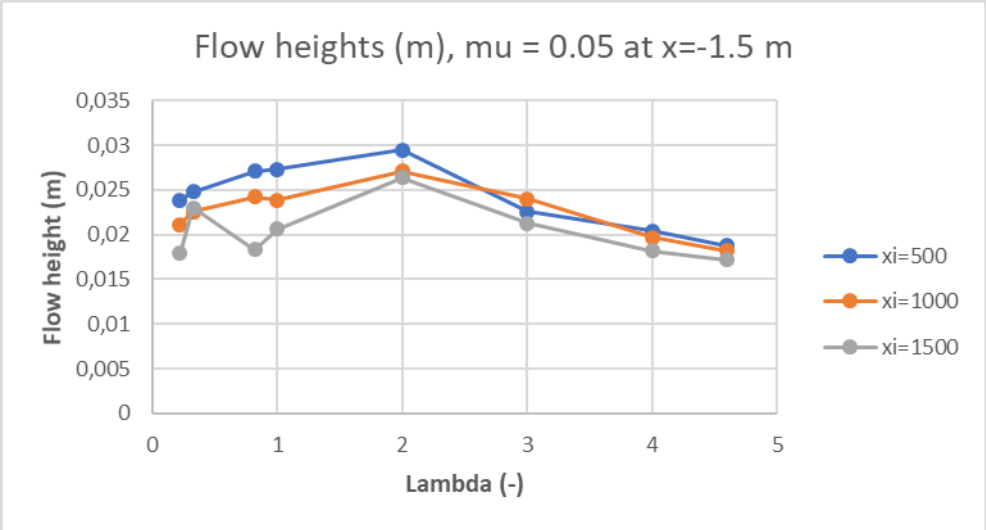

Figure 41 Flow heights at x=-1.5 m when $\mu = 0.05$ and ξ is varied between 500 and $1500\ m/s^2$.

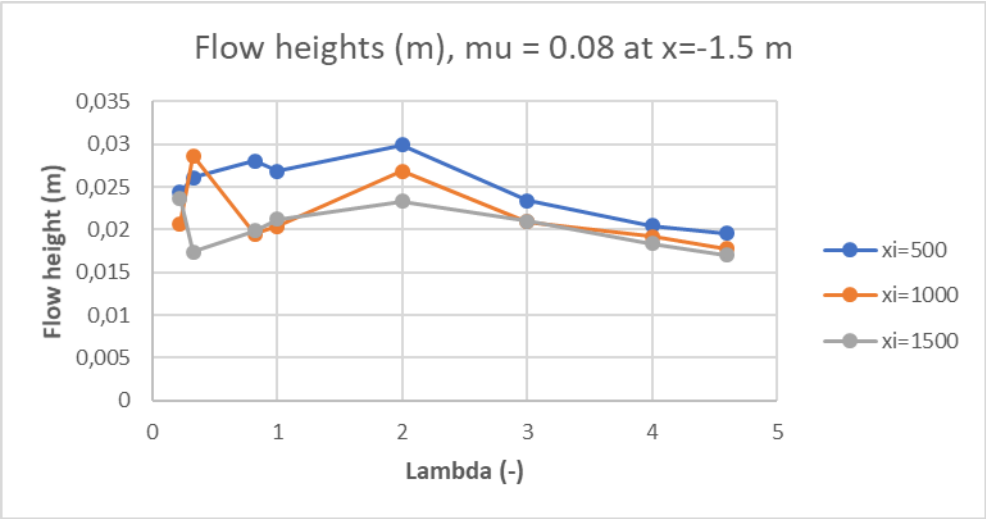

Figure 42 Flow heights at x=-1.5 m when $\mu = 0.08$ and ξ is varied between 500 and $1500\ m/s^2$.

The reduction in flow heights is little affected by a change in μ as is shown in Figure 43 to Figure 45. At x = -1.5 m, when $\xi = 500\ m/s^2$ in Figure 43, the overall effect on the active earth pressure coefficients as λ gets smaller, is a reduction of the flow heights. The reduction is approximately the same for every value of μ. For $\xi = 1000\ m/s^2$, the effect of λ-active is less and the curves of the flow heights in Figure 44 are flatter and in some of the cases start to increase. As ξ is increased to $1500\ m/s^2$ in Figure 45 however, the effect of the active earth pressure coefficient, when λ gets small, looks to increase the flow heights, as was the case at x = -1.1 m. There is a larger spread in the results of the flow heights depending on the active earth pressure coefficient as ξ gets larger.

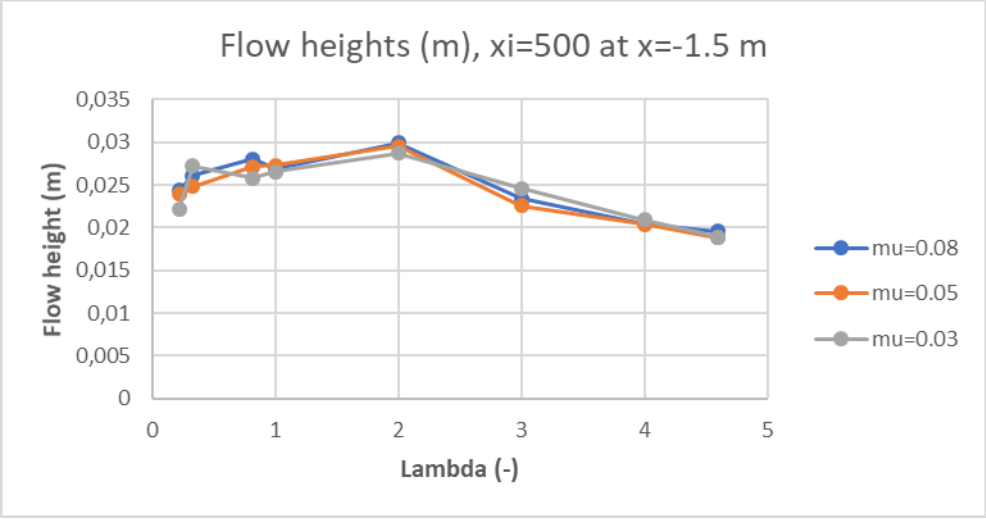

Figure 43 Flow heights at x=-1.5 m when $\xi = 500\ m/s^2$ and μ varies between 0.03 and 0.08.

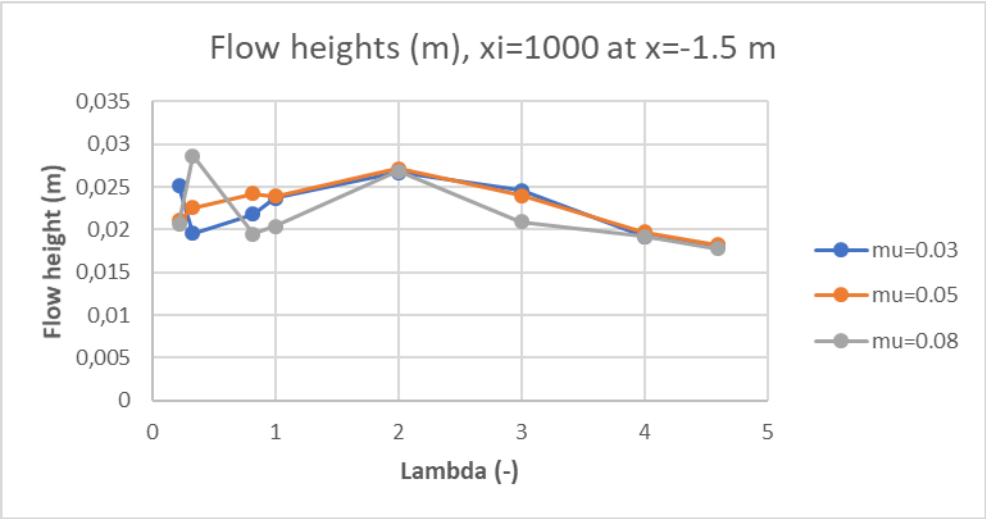

Figure 44 Flow heights at x=-1.5 m when $\xi = 1000\ m/s^2$ and μ varies between 0.03 and 0.08.

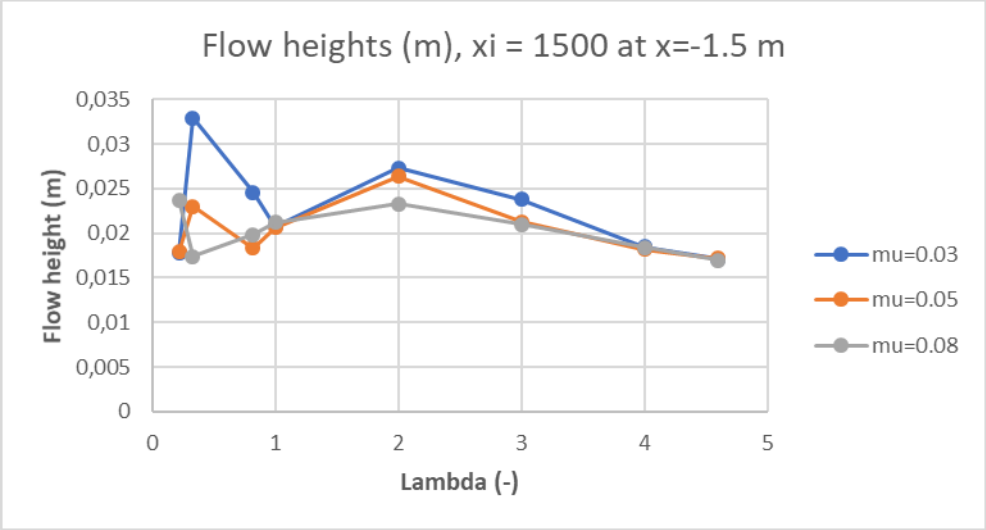

Figure 45 Flow heights at x=-1.5 m when $\xi = 1500\ m/s^2$ and μ varies between 0.03 and 0.08.

A lower value of μ leads to a greater reduction in flow heights as a result of the passive earth pressure coefficients. This means that for a higher value of μ, flow heights will decrease less for the passive coefficient, than if μ was lower. The reduction in flow heights at x = -1.1 m due to the passive λ, is around 31-40% when $\mu = 0.03$, 28-34% when $\mu = 0.05$ and 22-31% when $\mu = 0.08$. At x = -1.5 m the reductions yield 32-37% for $\mu = 0.03$, 32-36% for $\mu = 0.05$ and 27-34% for $\mu = 0.08$.

Flow heights of all simulations range between 15.7 mm and 30.5 mm at x=-1.1 m. Based on the reference case presented in section 3.1, flow heights are in fact ranging around the same values as for the physical experiments. Some values however are lower than the ones obtained by Teetzmann and Shrestha (2019).

5.2 Velocity

The velocities in the channel are scrutinized in the same way as the flow height, by varying λ for different μ and ξ and looking how the velocity is affected. The velocity for a

varying λ while μ is constant and ξ is changed is presented in Figure 46 to Figure 48 at x=-1.1 m and Figure 52 to Figure 54 at x=-1.5 m. Then trends are looked at for ξ being constant and varying μ in Figure 49 to Figure 51 when x=-1.1 m and Figure 55 to Figure 57 for x=-1.5 m. The velocities show different trends than the flow heights and are expected to be greatly influenced by ξ (Vicari, 2018).

The entire curve shifts upwards for an increase in the turbulent friction coefficient, ξ. This happens at any value of μ, shown in Figure 46, Figure 47 and Figure 48 . The change in ξ does not change the effect of the passive earth pressure coefficient on the velocity at x=-1.1 m. Curves remain parallel to each other independent of the value of ξ. The overall effect of introducing a passive earth pressure coefficient is a reduction of the velocities. When initially changing the earth pressure coefficient to a passive value of $\lambda = 2.0$, the reduction is small or in some cases not that different from the isotropic case. However, increasing the passive value beyond $\lambda = 2.0$, results in a steady reduction of the velocities as a function of the increasing value of λ.

The active coefficients produce slightly more stable results for the velocities as was the case for the flow heights. The effect of the active earth pressure coefficient changes only slightly with the different values of the turbulence friction coefficient ξ. Even though results are more stable for the velocities, the effects of the active coefficient still show more change for varying Voellmy friction parameters than the constant behavior for the passive coefficient. The effect of the active earth pressure coefficient on the velocities varies with ξ. As the value of the turbulence parameter is lowered, the effect of the active earth pressure coefficient is changed. For higher values of ξ the effect of λ seems larger than for the lower values. The effect of the active earth pressure coefficient on velocity of the debris flow is negative, meaning that in general, velocities are reduced for a smaller value of λ.

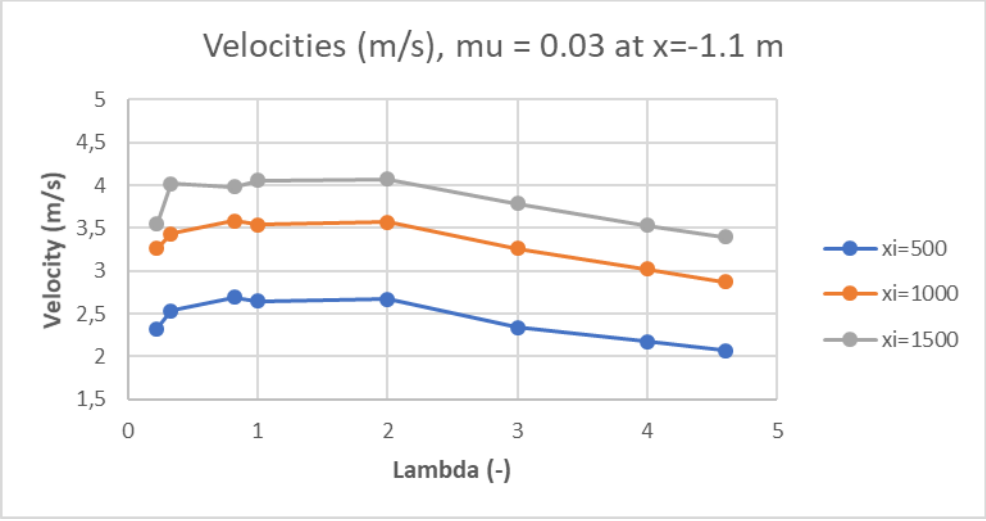

Figure 46 Velocities at x=-1.1 m when $\mu = 0.03$ and ξ varies.

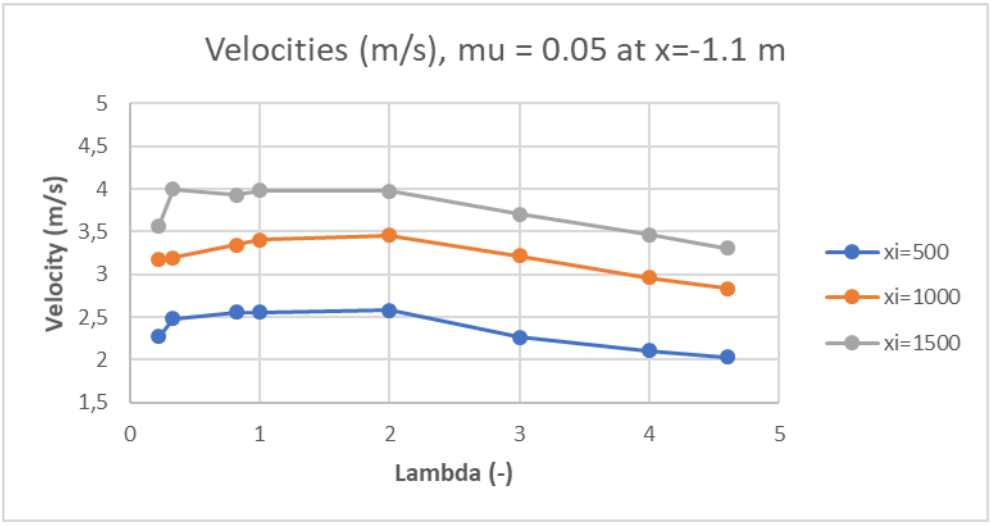

Figure 47 Velocities at x=-1.1 m when $\mu = 0.05$ and ξ varies.

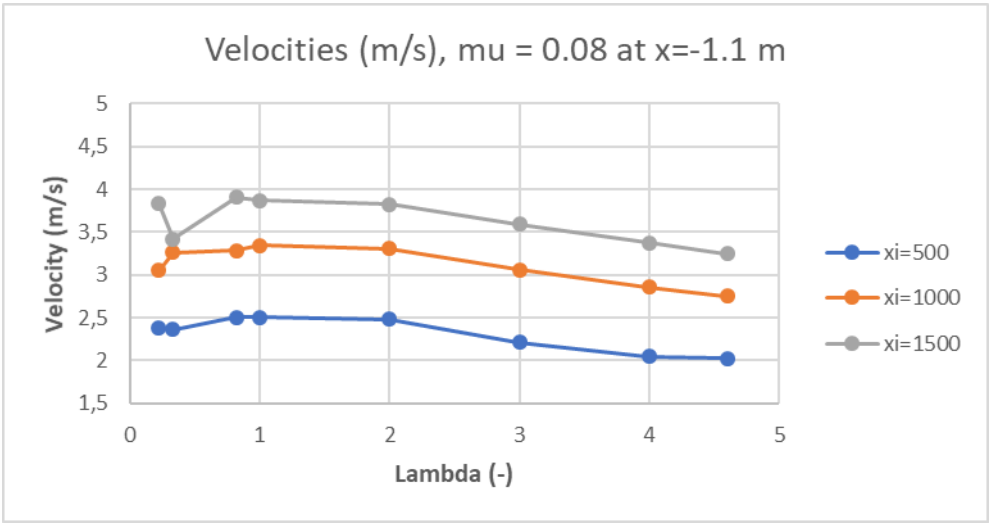

Figure 48 Velocities at x=-1.1 m when $\mu = 0.08$ and ξ varies.

Velocities change only somewhat for different friction coefficient μ at x=-1.1 m. This is seen from Figure 49, Figure 50 and Figure 51. The passive part of the curves matches well as they are on top of each other in the figures below. The effect of the active coefficients on the velocity changes more for the different values of μ than for the passive values. When the value of the turbulence coefficient ξ is small, the effect of the active earth pressure coefficient, λ, on velocity is small. As ξ increases, the active pressure coefficient has a larger influence on the velocities, shown by a steeper curve as λ gets smaller. The behavior of velocities for the active earth pressure coefficients seems little affected by a change in μ as curves remain mostly parallel. For the largest value of $\xi = 1500\, m/s^2$ and $\mu = 0.08$, a large deviation of the velocity is present.

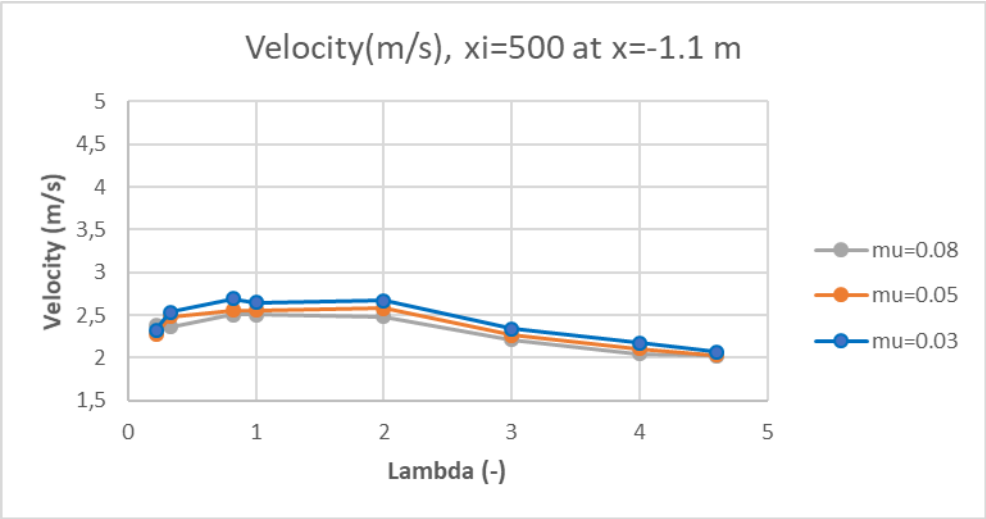

Figure 49 Velocities at x=-1.1 m when $\xi = 500\, m/s^2$ and μ varies.

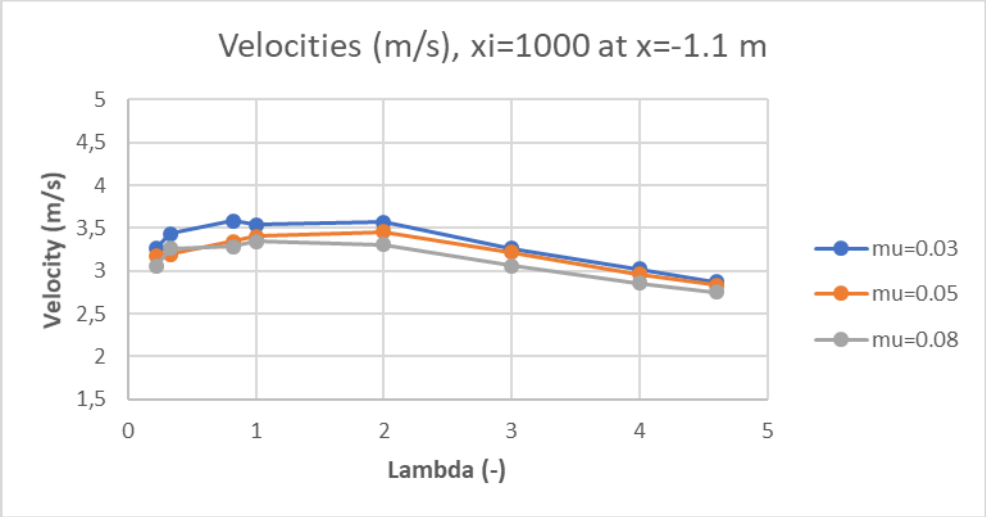

Figure 50 Velocities at x=-1.1 m when $\xi = 1000\, m/s^2$ and μ varies.

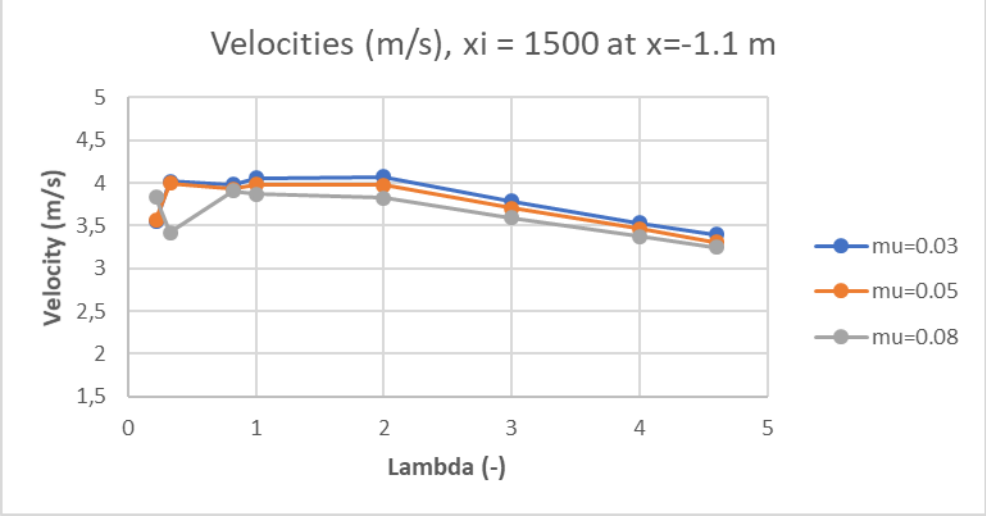

Figure 51 Velocities at x=-1.1 m when $\xi = 1500\, m/s^2$ and μ varies.

Further up in the channel for x=-1.5 m, behavior for the passive coefficients does not change much compared to behavior at x=-1.1 m. However, the initial decrease due to $\lambda = 2.0$ from the $\lambda = 1.0$, is larger. The slope of this initial decrease is dependent on the value of the turbulence coefficient ξ. As ξ is decreased, initial decrease is flattened.

The active values show the same effects dependent on ξ as was the case for x=-1.1 m. the behavior of the velocities due to the active earth pressure coefficient, λ is not changed due to the change of position.

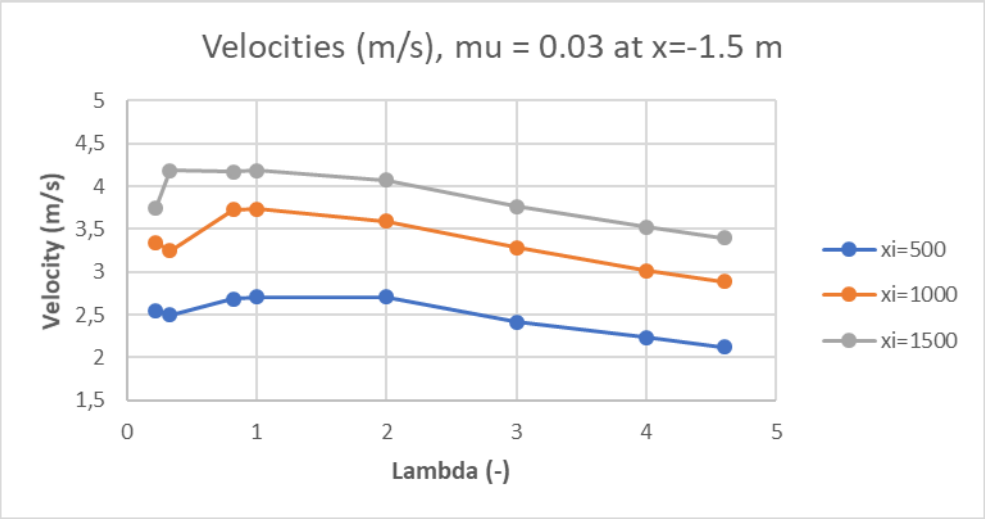

Figure 52 Velocities at -1.5 m when $\mu = 0.03$ and ξ varies.

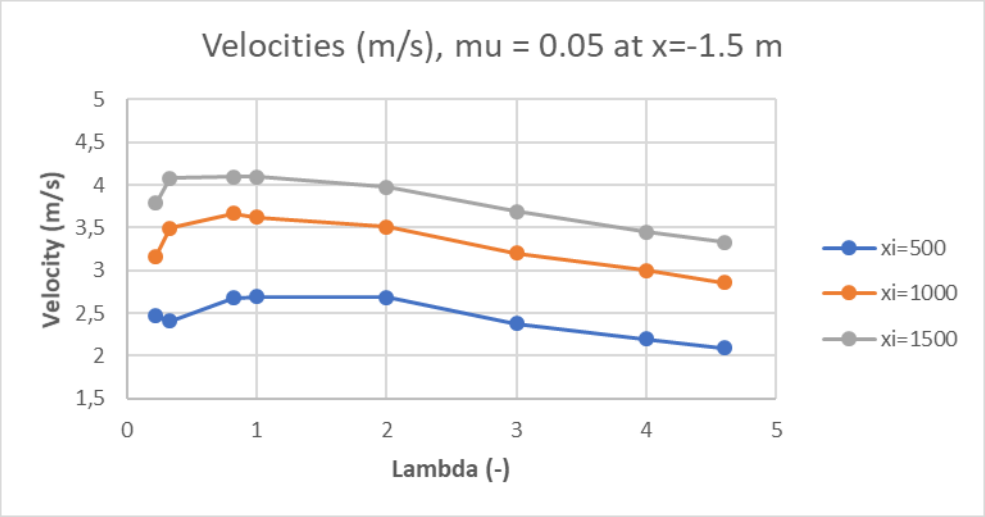

Figure 53 Velocities at -1.5 m when $\mu = 0.05$ and ξ varies.

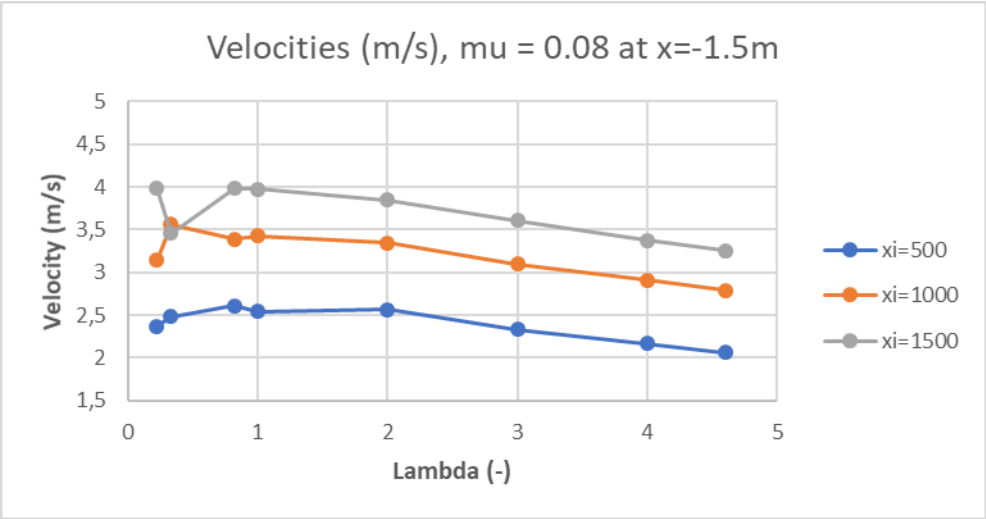

Figure 54 Velocities at -1.5 m when $\mu = 0.08$ and ξ varies.

As the value of the turbulence coefficient is kept constant and the friction coefficient μ is varied at x=-1.5 m, the velocities show little change in the effect of the passive λ. The effect due to the active coefficient discussed above is still present at x=-1.5 m. The change in behavior of the velocities due to the active earth pressure coefficient looks to be dependent on the turbulent friction coefficient, as it differs when increasing ξ in the figures above. The behavior of velocities for the active earth pressure coefficients looks independent on μ, as it changes little in the figures below. The large deviation for $\xi = 1500\ m/s^2$ and $\mu = 0.08$ is still present at x=-1.5 m.

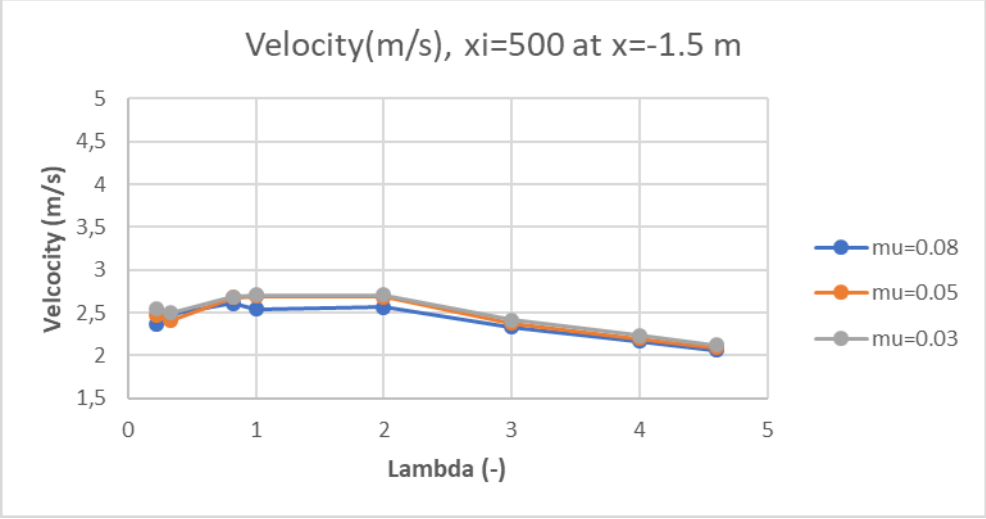

Figure 55 Velocities at -1.5 m when $\xi = 500\ m/s^2$ and μ varies.

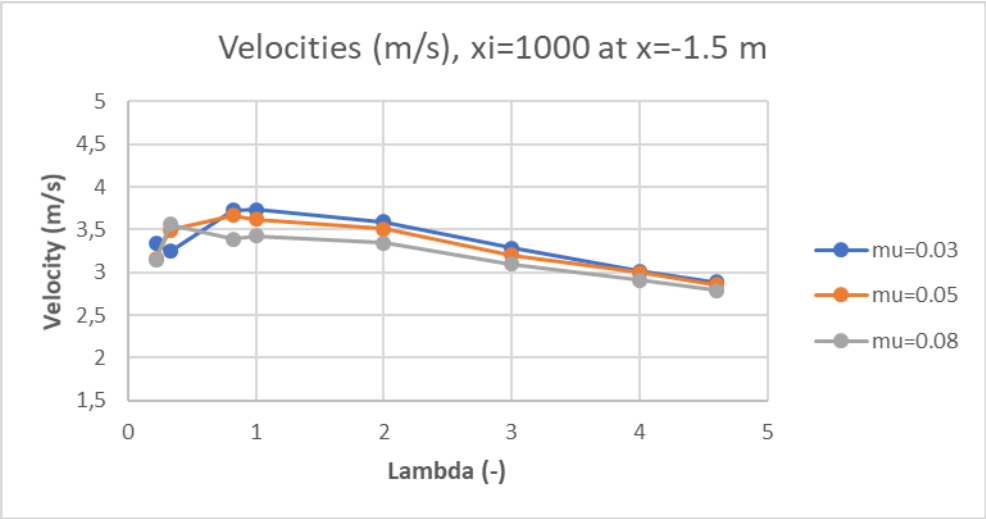

Figure 56 Velocities at -1.5 m when $\xi = 1000\, m/s^2$ and μ varies.

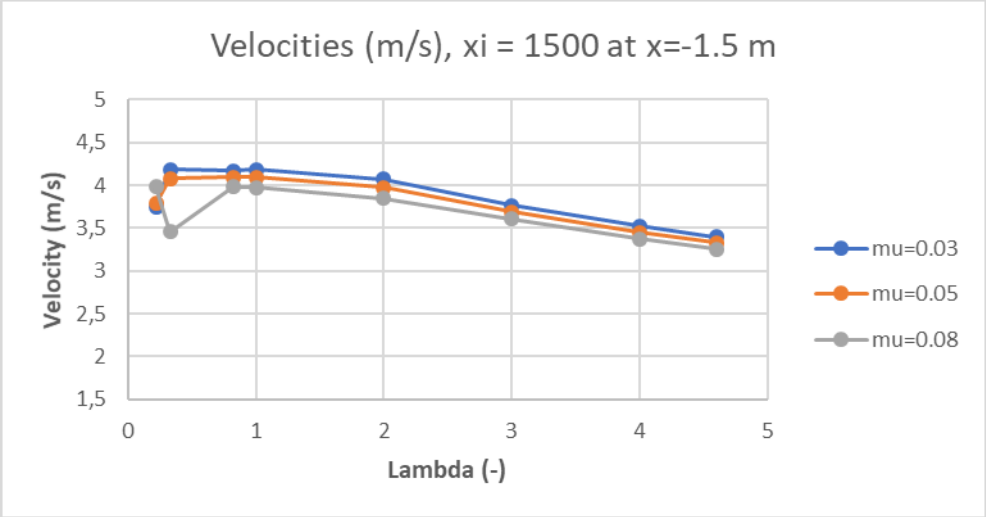

Figure 57 Velocities at -1.5 m when $\xi = 1500\, m/s^2$ and μ varies.

For both positions in the channel, the overall effect of the passive earth pressure coefficient is a reduction of flow velocities from the values for the isotropic earth pressure coefficient as λ is increased. The effect of the active coefficient is also a reduction in velocities, but smaller than for the passive values. The effect of the passive earth pressure coefficient, λ, changes little with respect to the Voellmy friction parameters, while the effect of the active λ changes more.

Investigations of the reductions of velocities for the passive coefficients, shows that the velocities at x=-1.1 m are slightly more reduced when μ is small compared to when μ is large. The same correlation is present for ξ. The largest reduction in the velocities for x=-1.5 m appears for the middle value of μ and ξ. In general, velocities are reduced 1.5-6.0% at x=-1.1 m and 1.0-6.0% at x=-1.5 m for the passive λ-values.

At x=-1.5 m, the velocities in the reference tests are in general between 3-5 m/s. Most of the repetitions are around 4 m/s. This is mostly obtained for the highest value of the turbulence friction coefficient ξ. Velocities at x=-1.1 m are in general a bit lower than for the reference test.

5.3 Runout shape and distance

5.3.1 Runout distance

The focus is first set to the runout distances and how they are affected by the different earth pressure coefficients. In general, the runout distance shows different effects of using the active and passive coefficient depending on the values of the Voellmy friction coefficients μ and ξ. Hence, configuration of these parameters will influence how the earth pressure coefficient affects runout distance. Figure 58 includes a scenario in which the debris flow crashes into the end wall, and the effect of λ on runout is hence difficult to evaluate. This is shown as a straight horizontal line at 4.96 m, which is equal to the total runout length of the numerical model.

When the friction parameter μ is set to 0.03 in Figure 58, using passive earth pressure coefficients results in stabilization of the runout distances at a higher value than runout distance resulting from the isotropic earth pressure coefficient, $\lambda = 1.0$. All values of ξ when $\mu = 0.03$ result in an initial increasing effect of the earth pressure coefficient λ on runout distances. There is little change in effect as λ is increased beyond the initial passive value, $\lambda = 2.0$. The overall effect of the passive values of λ is a spike to the runout distances. The active earth pressure coefficients cause a decrease in runout lengths as their values get lower. Hence the effect of the active earth pressure coefficient, λ, on runout lengths when μ is low is a reduction, independent of the value of ξ.

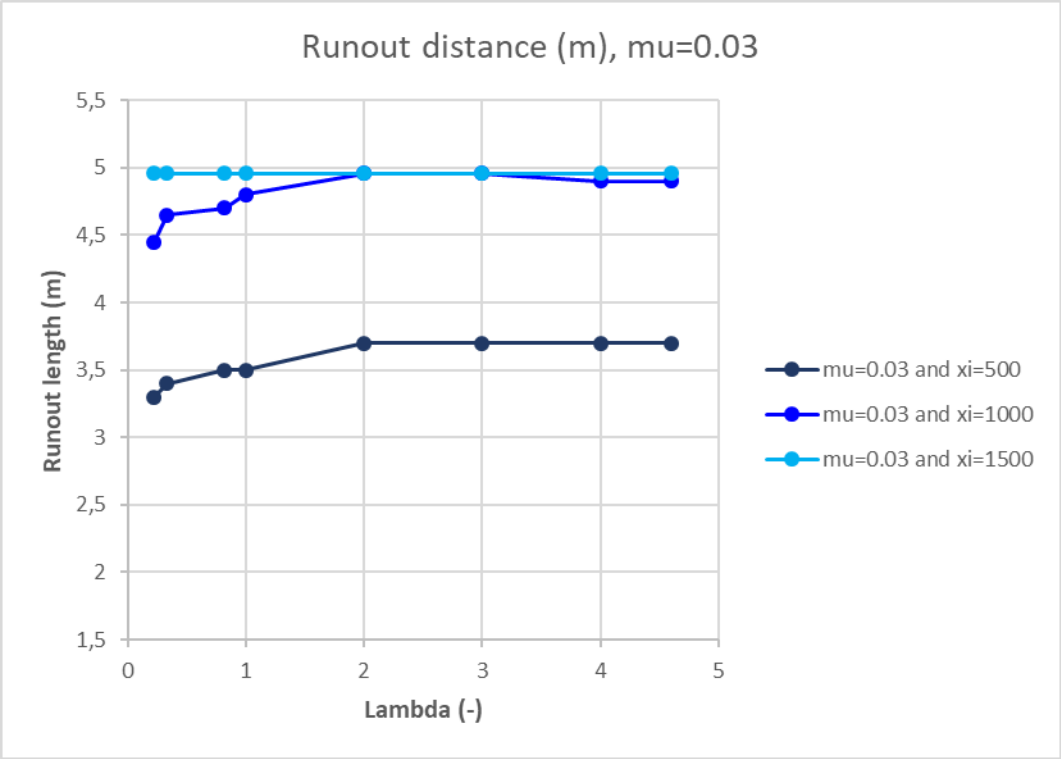

Figure 58 Variations in runout depending on λ when μ = 0.03.

As the value of the friction parameter μ is increased to $\mu = 0.05$ and $\mu = 0.08$ in Figure 59 and Figure 60, the variation of the runout lengths as a function of λ changes. When the value of the coefficient μ is low, it does not seem like ξ affects how λ influenced the runout lengths. When the earth pressure coefficient takes passive values, $\lambda > 1.0$, for higher values of μ, the initial increase in runout from the isotropic condition is still

present. The effect of λ-passive on the runout lengths however, changes as the earth pressure coefficient is increased further $\lambda > 2.0$. When $\xi = 500\ m/s^2$ the runout lengths continue to increase as a function of the increasing passive λ. For $\xi = 1000\ m/s^2$, the behavior is similar as described for $\mu = 0.03$, as runout lengths stabilize around 4 m. For the highest value of $\xi = 1500\ m/s^2$, the passive earth pressure coefficients, $\lambda > 2.0$, result in the runout lengths decreasing as λ continues to increase. The behavior of the runout based on the active coefficients is little affected by the variations in the turbulence coefficient ξ.

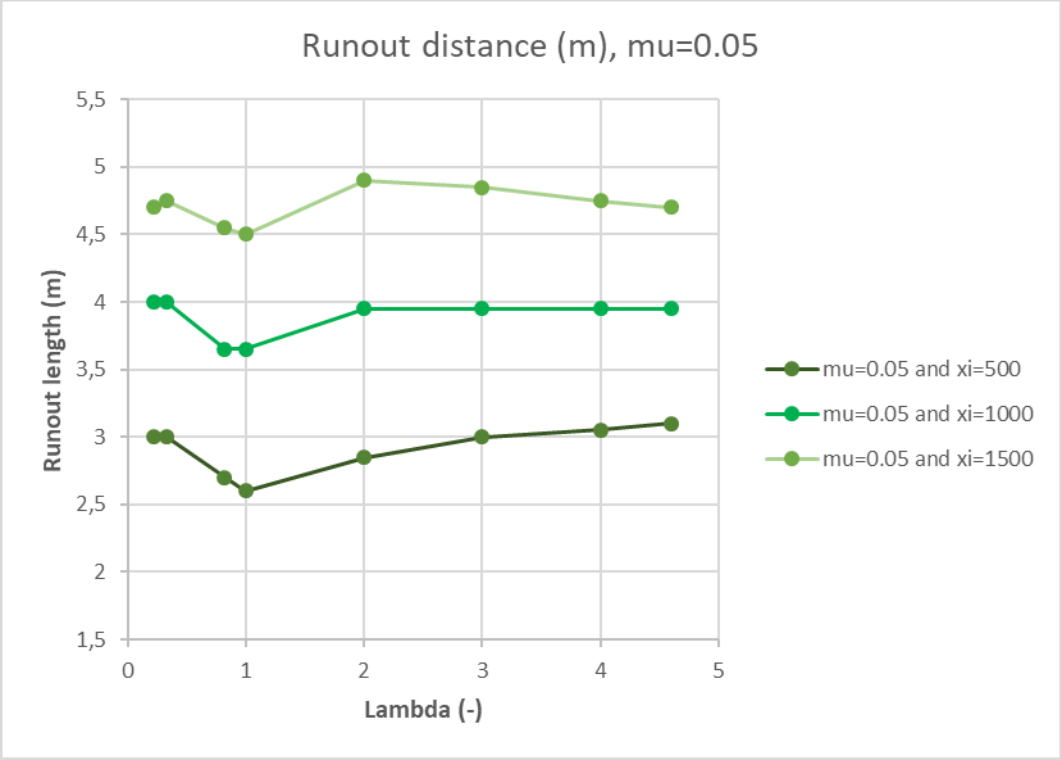

Figure 59 Variations in runout depending on λ when μ = 0.05.

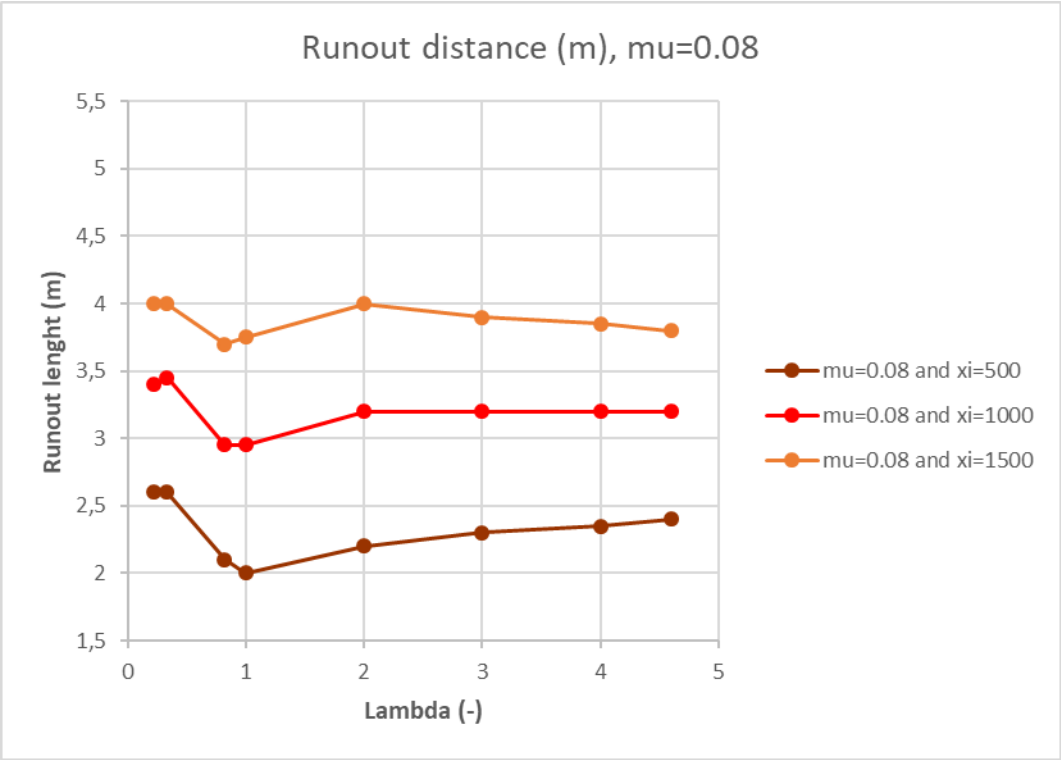

Figure 60 Variations in runout depending on λ when μ = 0.08.

The effect that changing the earth pressure coefficient has on the runout distance, also varies somewhat with the value of the friction parameter μ, as can be seen from Figure 61 to Figure 63.

The effect of the passive earth pressure coefficient changes little with μ when $\mu = 0.05$ and $\mu = 0.08$ for $\xi = 500\ m/s^2$. The main change in the effect of the passive λ appears when μ is reduced to a value of 0.03. As stated before, these runout distances stabilize for further increase of the passive earth pressure coefficient after an initial increase from the isotropic case.

For the active values of λ at $\xi = 500\ m/s^3$, $\mu = 0.05$ and $\mu = 0.08$, there is an increase in runout lengths as λ gets smaller, from the value of the runout lengths produced with an isotropic earth pressure coefficient $\lambda = 1.0$. The curve is steepest for $\mu = 0.08$ which shows that the effect of λ is the greatest for this value of μ. As μ reduces to 0.05, the effect of the active λ is slightly reduced as the slope of the curve gets less steep. When $\mu = 0.03$, the active behavior is changed considerably. Instead of the active behavior increasing runout lengths, they are now decreased for smaller values of λ.

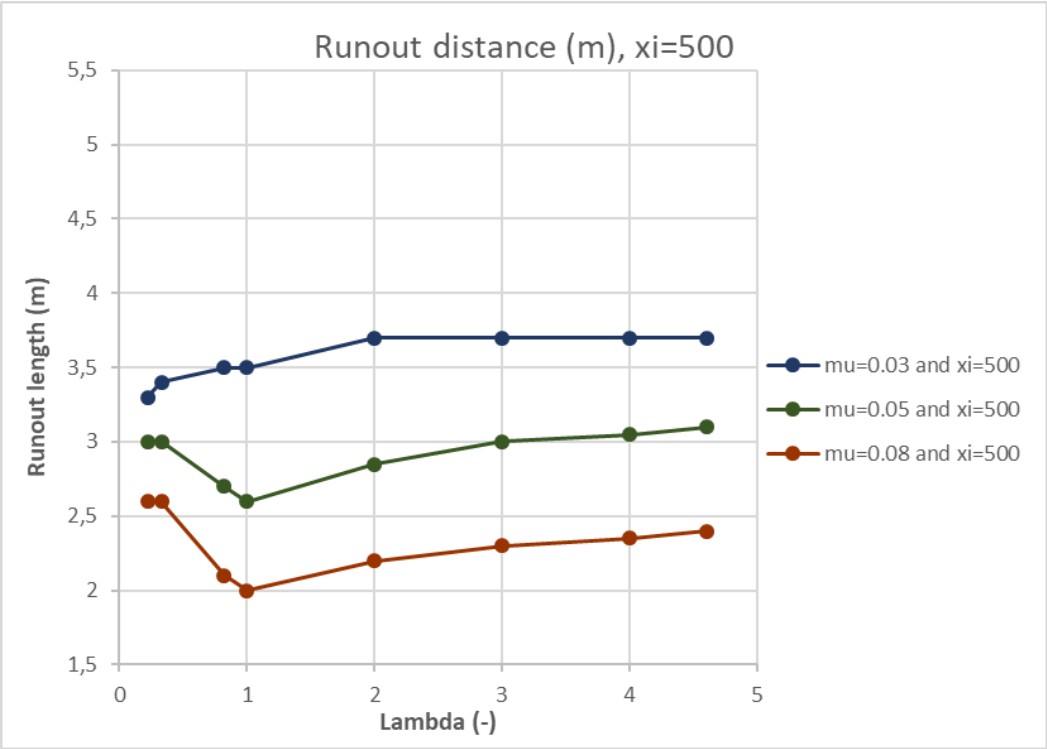

Figure 61 Variations in runout depending on λ when ξ=500 m/s².

For higher values of the turbulence parameter ξ, the variations of the runout distance dependent on the passive values of λ, don't change much with μ. The effect of the active coefficient still changes for the different values of μ, as $\xi = 1000\, m/s^2$. Effects of the active earth pressure coefficients on the runout distances remain the same as stated for $\xi = 500\, m/s^2$ when μ is changing.

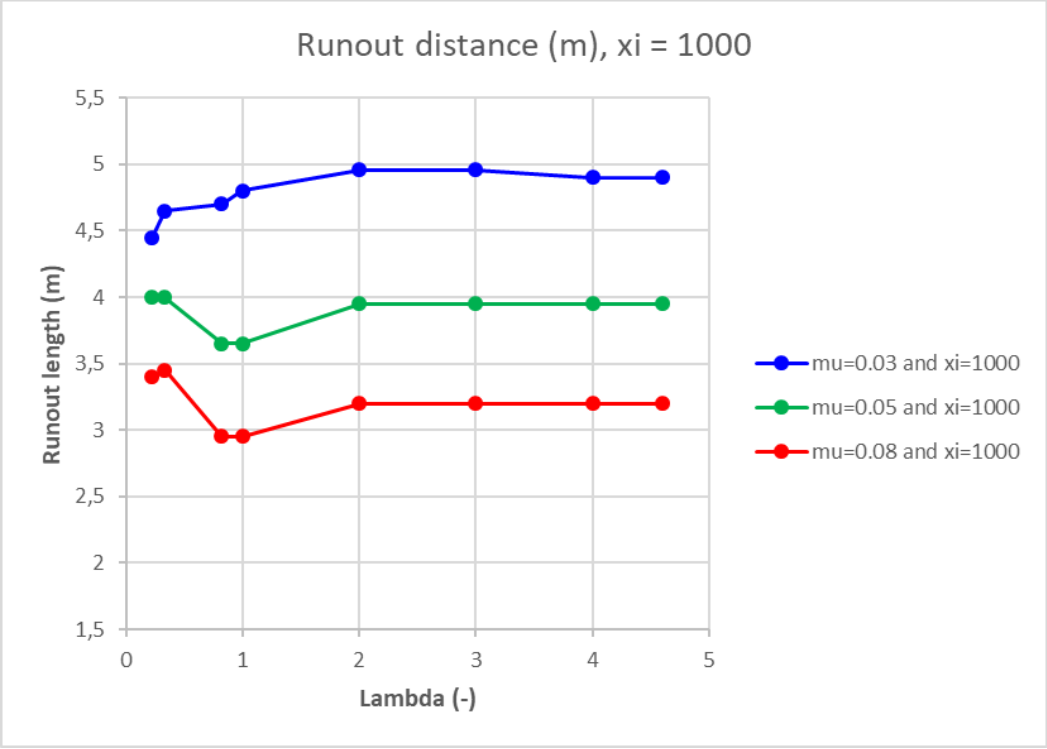

Figure 62 Variations in runout depending on λ when ξ=1000 m/s².

As $\xi = 1500\, m/s^2$, it is important to notice the special case for $\mu = 0.03$, when the flow crashed into the end wall which is discussed earlier in this section. The effect on the runout distance in this case is hence not considered for the following explanations.

The effect of the passive earth pressure coefficient on the runout distance is not altered for a changing value of μ, which corresponds well to the statements made for $\xi = 500\, m/s^2$ and $\xi = 1000\, m/s^2$. The runout distances decrease as a result of an increase in the passive earth pressure coefficients after the initial increase for this value of ξ. This effect does not change with μ.

The same yields for the effect of the active earth pressure coefficient on the runout distance. Both values of μ produce similar increase in runout distance due to λ getting smaller. Runout distances change little with the value of μ.

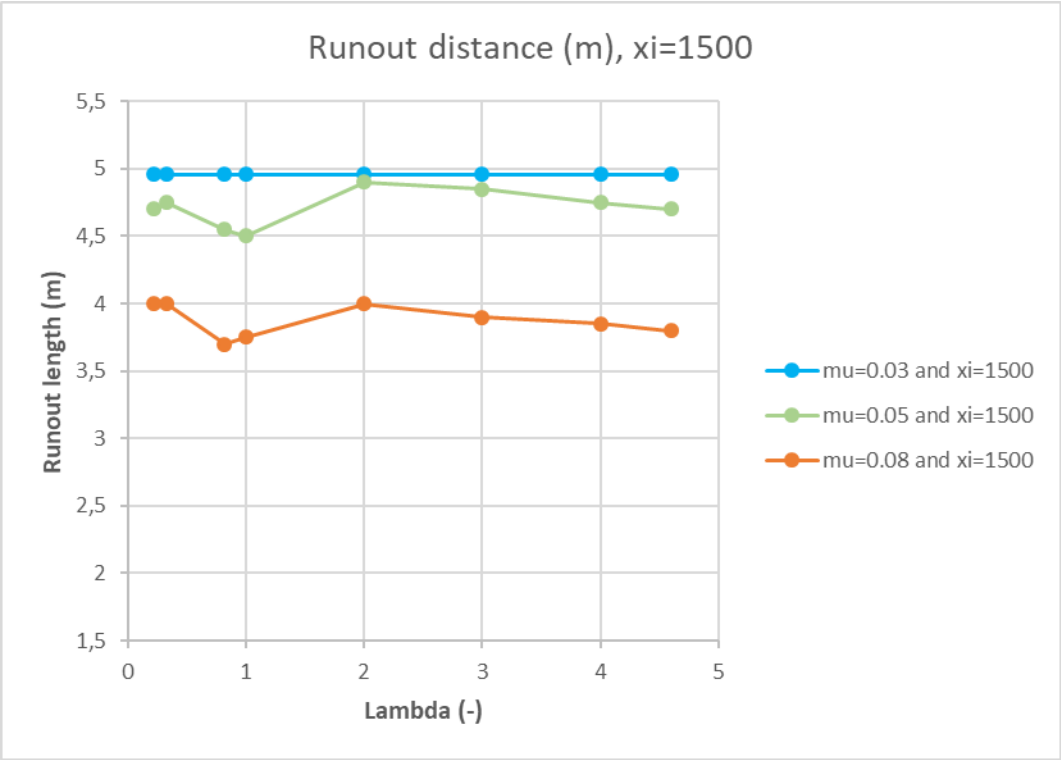

Figure 63 Variations in runout depending on λ when ξ=1500 m/s².

In all cases, passive value increases the runout distance initially, while runout distances for active coefficients initially are only increased for $\mu = 0.03$ or 0.05.

Additionally, the heights of the deposits in the runout zone are also decreased for the introduction of both the active and passive coefficients compared to the isotropic state as seen in Figure 64 to Figure 66.

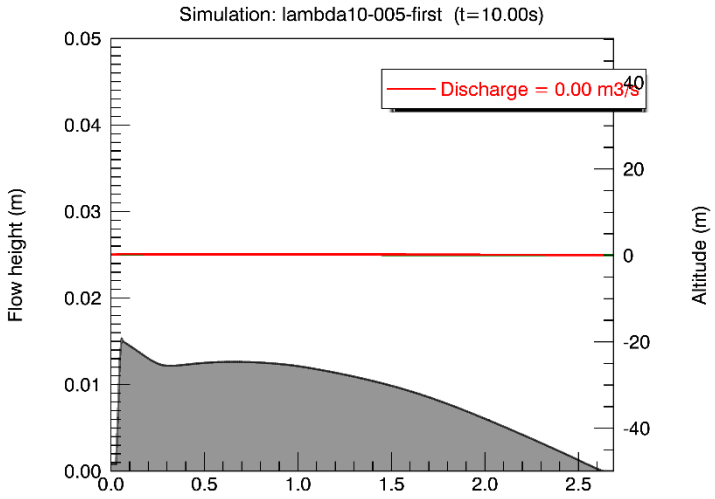

Figure 64 Height in deposited material when $\lambda = 1.0$. $\mu = 0.05$ *and* $\xi = 500m/s^2$.

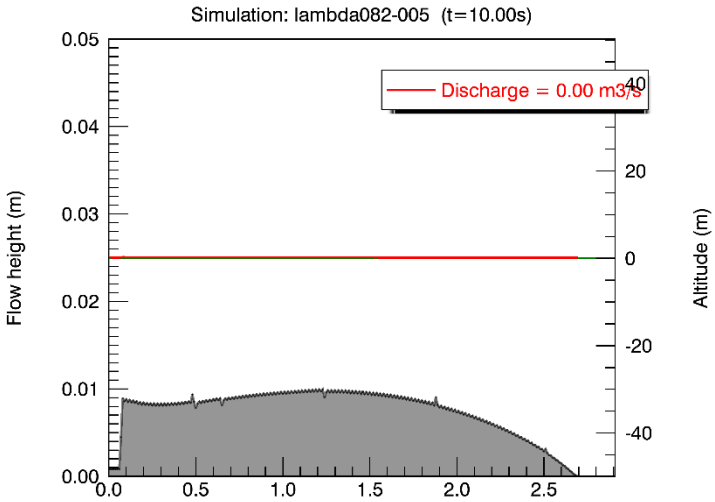

Figure 65 Height in deposited material when $\lambda = 0.82$. $\mu = 0.05$ *and* $\xi = 500m/s^2$.

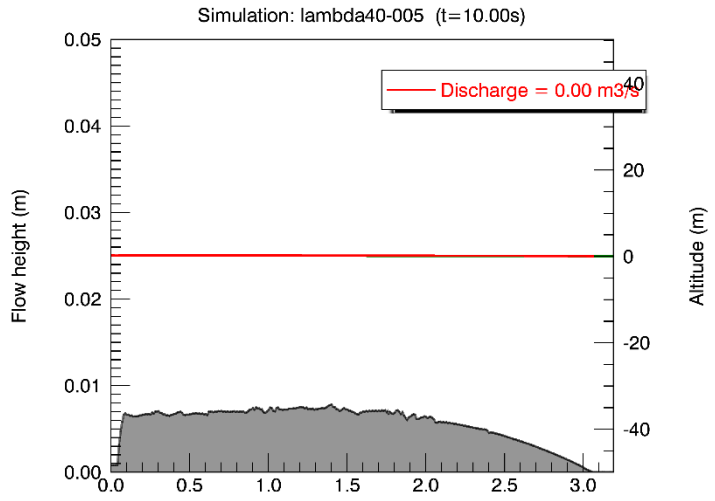

Figure 66 Height in deposited material when $\lambda = 4.0$. $\mu = 0.05$ *and* $\xi = 500m/s^2$.

5.3.2 Runout shape

The effects of the earth pressure coefficients on runout shapes are tested for two different slopes: $17.5°$ and $30°$ (Teetzmann & Shrestha, 2019; Vicari, 2018). Recalling the three different approaches for calculating the earth pressure coefficient from section 4.3:

1. Savage and Hutter (1989) with bed friction angle, $\delta_1 = 30°$ and internal friction angle, $\varphi = 40°$.
2. Rankine approach with internal friction angle, $\varphi = 40°$.
3. Rankine approach with internal friction angle, $\varphi = 30°$.

From the results of the steepest slope of $30°$, one can clearly see that the effect of the active and passive earth pressure coefficients results in both a wider and longer runout for all three approaches when $\mu = 0.05$ and $\xi = 500\, m/s^2$.

For the first approach shown in Figure 67, the runout is both elongated for the active and passive earth pressure coefficients. The longest and widest runout is obtained for the passive earth pressure coefficient. This shows that the increased passive pressure in the flow results in not only a longer runout but also a wider one. There is not too much of a difference between the active and isotropic earth pressure coefficients for this case, so the shape of the depositions is similar. The active case however is somewhat longer and wider and has a narrower runout at the start of the zone.

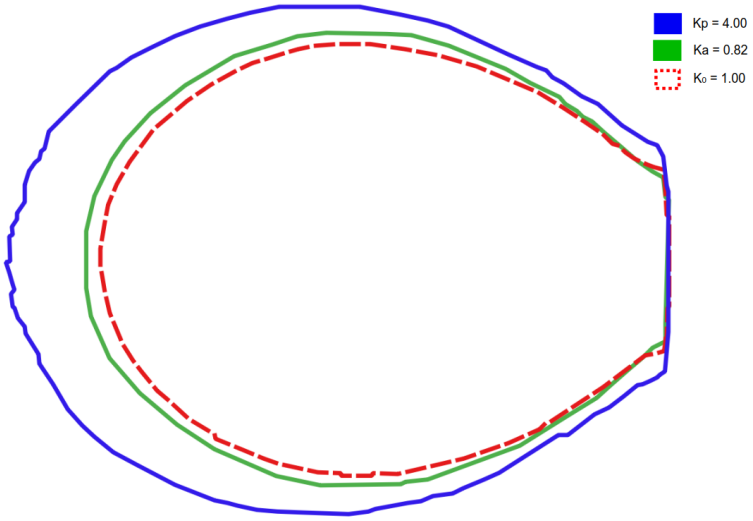

Figure 67 Runouts of approach 1 on a $30°$ slope, when $\mu = 0.05$ and $\xi = 500\, m/s^2$.

As the value of the active earth pressure coefficients gets very low, as for the Rankine approaches (approach 2 and 3), the shape of the runout becomes both longer for the active coefficient than for the passive and gets an odd shape. Instead of the runout having the expected round parabolic shape, the deposited shape becomes advanced along the edges as a result of large lateral spreading and the debris flow crashing into the side edges.

For the passive coefficients however, the above-mentioned effect on runout shape is not this large and deposit shape looks as expected. The runout of these two Rankine approaches is elongated as a result of using passive coefficients. The passive cases in both approaches are longer than the initial case of isotropic earth pressure coefficient. In

approach 3, the runout does not increase as much laterally as longitudinally, and it is hence more elongated than widened for the passive coefficient.

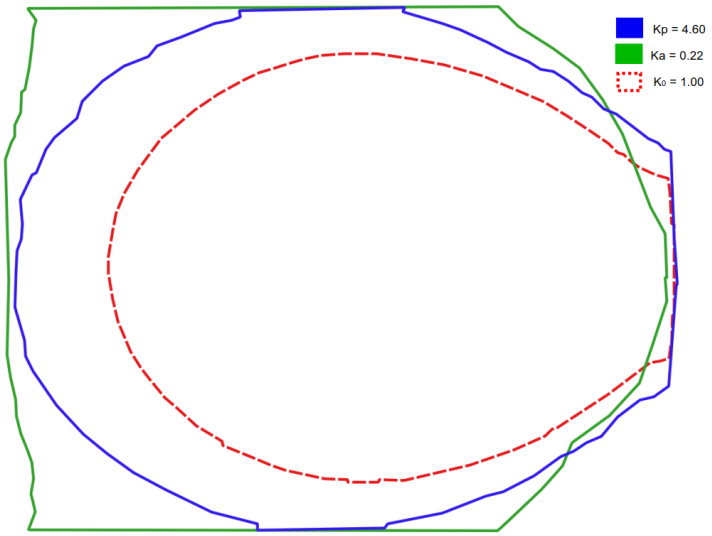

Figure 68 Runouts of approach 2 on a $30°$ *slope, when* $\mu = 0.05$ *and* $\xi = 500\, m/s^2$.

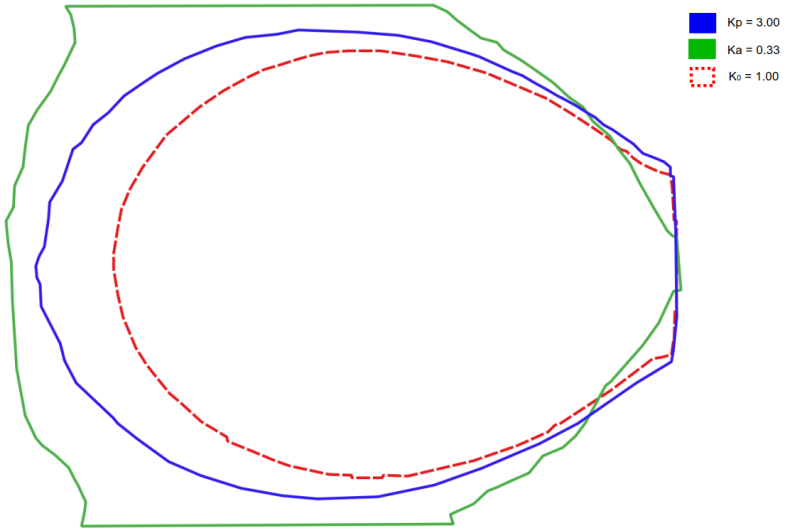

Figure 69 Runouts of approach 3 on a $30°$ *slope, when* $\mu = 0.05$ *and* $\xi = 500\, m/s^2$.

The results of the $17.5°$ are now compared to the results of the $30°$ slope. The most obvious difference between the $17.5°$ slope in Figure 70 to Figure 72 and the $30°$ slope in the figures above, is that the runout for the passive earth pressure coefficient is longer than the runout for the active coefficient in the second approach. The shape is still odd for the two Rankine approaches as was described earlier. Both passive and active earth pressure coefficients result in a wider and shorter runout than for the $30°$ slope. For the passive coefficient runout gets a more elongated shape than for the two other states of the coefficient for the slope angle of $17.5°$.

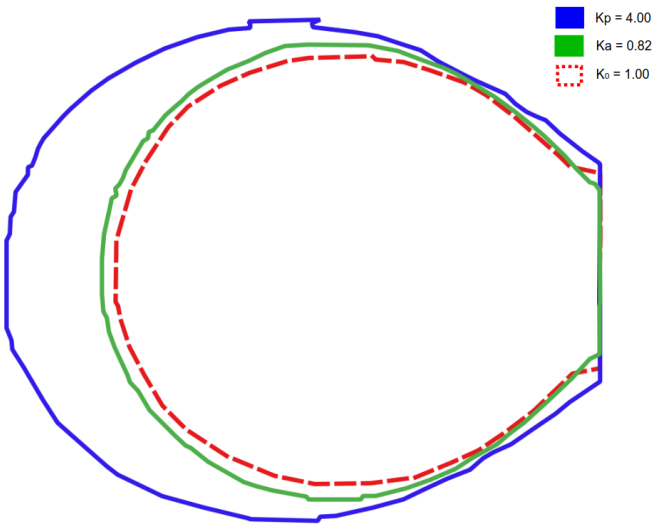

Figure 70 Runouts of approach 1 on a 17.5° slope, when $\mu = 0.05$ and $\xi = 500\, m/s^2$.

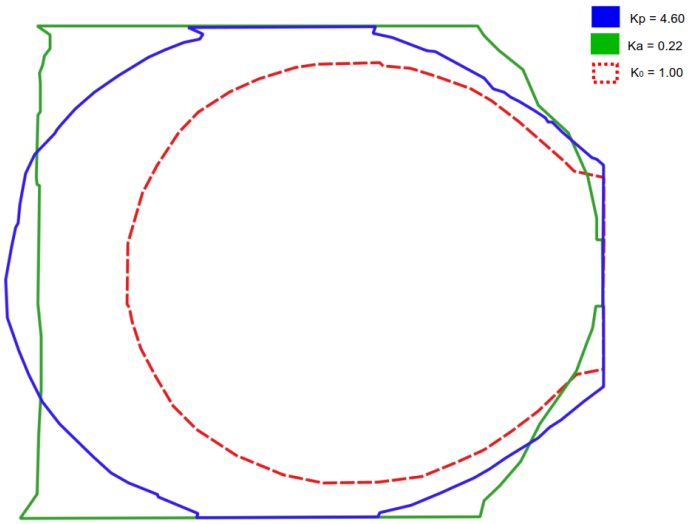

Figure 71 Runouts of approach 2 on a 17.5° slope, when $\mu = 0.05$ and $\xi = 500\, m/s^2$.

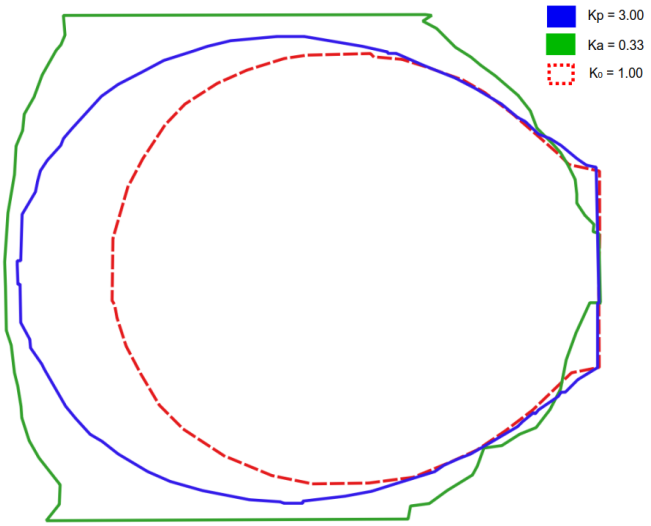

Figure 72 Runouts of approach 3 on a 17.5° slope, when $\mu = 0.05$ and $\xi = 500\, m/s^2$.

For higher values of ξ, the runout travels longer and there is less widening in the runout for both active and passive parameters in the lateral direction. This causes the passive earth pressure coefficients to give an elongated effect on the runout distances. See the Appendix for examples these shapes when ξ is high for $\mu = 0.05$ and $\mu = 0.08$ for the first approach when the slope angle is set to $30°$ and runout is not influenced by hitting the walls.

5.4 Froude number

The effects of the earth pressure coefficients on the Froude number can be seen from locations x=-1.1 m and x=-1.5 m. The plots are shown in Figure 73. The results of variation of the Froude number vary little between different values of μ for a constant value of ξ. Hence, only plots for constant $\mu = 0.05$ and varying values of ξ are presented

The Froude number is reduced when introducing passive earth pressure coefficient values in the debris flow. After this initial reduction of the Froude number due to the introduction of passive coefficients, the Froude number does not change for an increasing value of the earth pressure coefficient but remains constant.

As the earth pressure coefficient becomes active and λ-values become less than 1.0, the Froude numbers show a decreasing tendency. This means that the active earth pressure coefficients give a decrease in the Froude number as λ gets lower. This effect varies with the value of ξ. The slope of the decrease for λ getting smaller, gets flatter by reducing ξ, and shows for the lowest value of ξ, a slight increase. This indicates that the effect of the active earth pressure coefficient λ decreases with ξ.

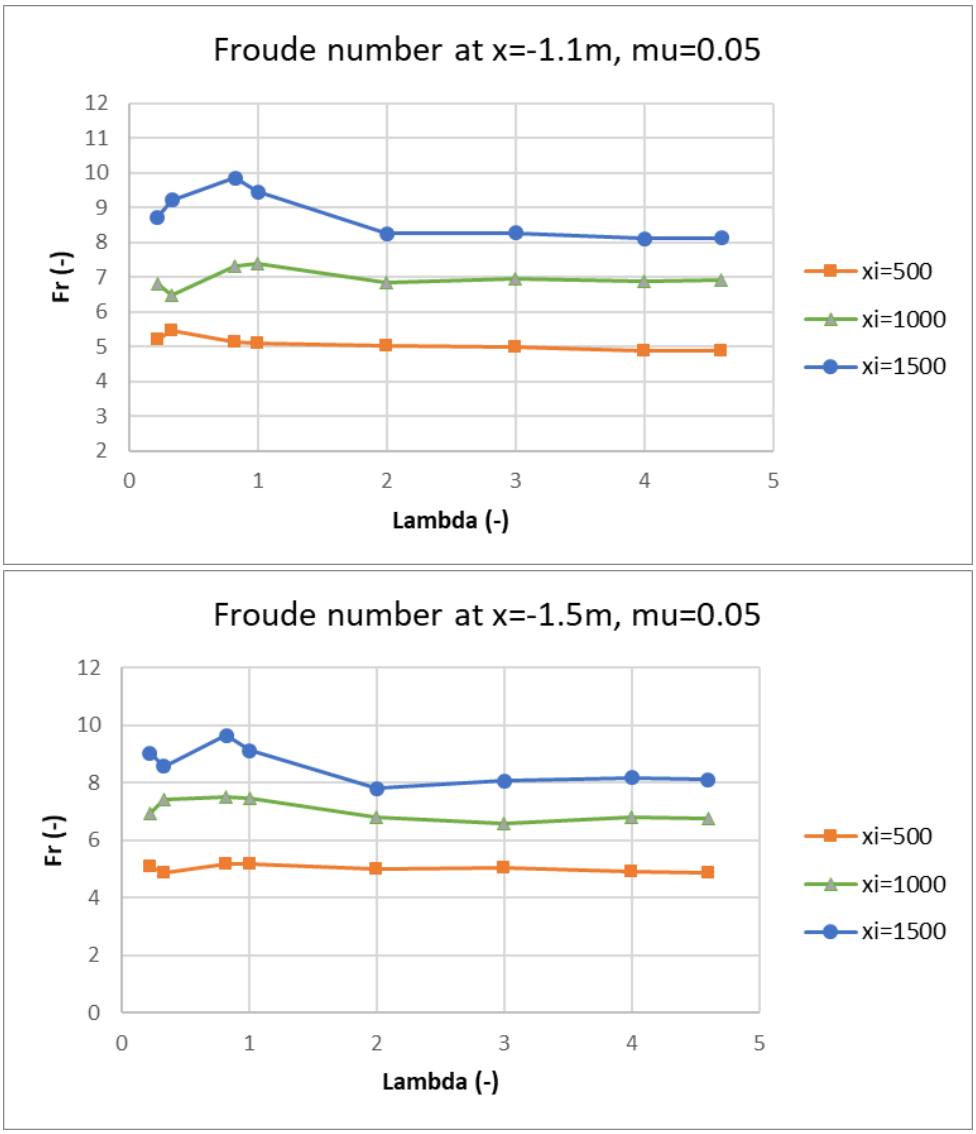

Figure 73 Variation of the Froude number for changing the earth pressure coefficient λ when $\mu =$ 0.05 and $\xi = 500, 1000$ and 1500 at x=-1.1 m and x=-1.5 m

6 Discussion

The aim of this chapter is to discuss the debris flow behavior based on the results obtained from the simulations presented in the previous chapter. The influence of the earth pressure coefficient resulted in trends for the properties measured in the channel such as flow height and velocity. The influence of the active and passive earth pressure coefficient is seen for both runout shape and distance. The runout shape shows more clearly the effects of the earth pressure coefficients, as the runout zone allows for wider spread of motion.

6.1 Flow heights and velocity

The behavior of flow velocity and height is compared with the experiments of Gray et al. (1999). In section 2.6, it is explained how the active and passive coefficients are introduced as a result of dilative or compressive behavior, respectively. This dilative or compressive behavior was dependent on the velocity gradient being either positive or negative. A positive velocity gradient gives the motion a dilative behavior which introduced active pressure coefficients. A negative velocity gradient expressed a compressive motion and hence introduced passive coefficients. At the points x=-1.1 m and x=-1.5 m, the behavior in the slope of these experiments can be compared with what happens on the slope in the experiments of Gray et al. (1999). Early in the flow, the flow will experience a dilative motion in the longitudinal direction at these positions. This introduces the active earth pressure coefficients in this direction. The cross-slope behavior is first divergent but turns convergent due to a curved slope in Gray et al. (1999). Later, the behavior on the slope is still divergent in the longitudinal direction and converging in the lateral direction. Hence, using the active pressure coefficients in the slope should give a realistic behavior in the longitudinal direction of the flow. Using active or passive coefficients in the cross-slope direction may modify the width of the flowing masses. Although the motion is not correspondent to a passive state longitudinally, the lateral walls in the numerical model of this thesis might introduce a compression laterally which associates with the use of passive earth pressure coefficients. RAMMS however, only allows to set the earth pressure coefficient either active or passive, and this value will be constant for the entire simulation and does not change with the velocity gradient.

The earth pressure coefficient λ significantly affects the value of the flow heights. Using a passive earth pressure coefficient, the value of the flow height is initially increased from the isotropic state, but flow heights are decreased as a function of λ from this initial value. The effect of the active earth pressure coefficients is highly dependent on location in the flume and ξ. Flow heights increase with high values of ξ and decrease as ξ gets low when the earth pressure coefficient is active, meaning that λ gets smaller. The velocities become smaller for the introduction of any earth pressure coefficient.

The use of the active or passive earth pressure coefficients laterally can help to change the width of the mass along a slope depending on the gradient of the velocity in this direction. However, the narrow flume in these simulations used to simulate the debris flow, makes it hard to determine the effect on the width of the mass, as one does not see lateral expansions or compressions well. The flow heights become smaller in the channel as a result of using both active and passive coefficients compared to the isotropic state.

This effect also becomes difficult to explain due to the large interaction with the side walls during the flume which could influence the magnitude of the flow heights.

One may expect that debris flow velocities get higher using increased passive coefficients due to a higher earth pressures in the longitudinal direction when looking at the momentum equation (2.16) in section 2.5.4. Velocities are however decreased due to the increased passive coefficients. A possible explanation for this could be the interaction with the sidewalls, as the passive coefficients that associate with a lateral compression, might widen a flow if they are increased due to higher earth pressure and can hence induce more interaction with the walls. As discussed earlier this effect is difficult to assess in the channel. The active coefficient is associated with the dilatational behavior which happens in the longitudinal direction. A lower value of the active coefficient in this direction will introduce a negative effect on momentum in the longitudinal direction which might lead to a negative effect on the change in velocities. RAMMS will use the same coefficient in both directions and introduce this laterally also, hence, this might lead to less interaction along the walls.

Since the difference between flow heights of different values of ξ get smaller as a result of increasing passive coefficients, the turbulence friction effects become smaller in the flow. This friction parameter, hence, becomes less important for higher values of the passive earth pressure coefficient. Since the velocities are also reduced for a larger value of the passive earth pressure coefficient, this could explain why the importance of the turbulence friction is reduced. When velocity is reduced, the contribution of the term including the turbulence friction in equation (2.18) in section 2.5.4 becomes smaller and the total friction term is reduced in the channel becoming mostly dependent on μ. Change in velocity might have a larger influence on the acting forces than a change in ξ, resulting in the value of ξ becoming less important. A reduction in velocity will mean a deceleration having a negative effect on the momentum in the flow. At the same time a positive effect is exhibited on the momentum by the decrease in turbulence friction. The overall effect on momentum is however considered negative.

6.2 Runout shape and distance

The behavior of the simulated debris flow runout zone can be associated with the behavior of the horizontal zone of the experiments of Gray et al. (1999). When the flow first hits this section, the front is somewhat compressed at first but continues to diverge at the front through the runout zone. At the end of the flow however, when the flow comes to an end and the flow decelerates, the entire behavior is compressional in the downslope direction as the tail of the flow gets a chance to catch up with the front. The magnitude of the gradient in the longitudinal direction is greater than the magnitude of the velocity gradient laterally. If one introduces an active earth pressure coefficient in the lateral direction, the width of the runout could be reduced (Gray et al., 1999).

When a debris flow enters the runout zone, the channel walls disappear, and debris flow is free to move within the confinement of the runout zone. In many of the simulations, the runout never hits either the lateral walls or the end wall. As the flow slows down due to the gentler slope of the runout zone and the debris material is compressed, the earth pressure coefficients for this motion should be passive longitudinally according to the definitions (Savage & Hutter, 1989). In the case of these numerical simulations, it was expected that increasing passive coefficients might lead to greater flow heights as flow was more compacted. However, smaller flow heights occurred in the runout for both active and passive earth pressure coefficients. For the passive coefficients, this might be

a result of increased earth pressures with the higher passive coefficient resulting in a longer runout. The reduction in flow heights due to the active coefficients might also be a result of longer runout distance. The larger runout distances are discussed in a later paragraph.

The results show that the values of the Voellmy friction parameters also play an important role in how the earth pressure coefficients affect the runout distance. It turns out that if the value of the turbulence parameter is low, the runout increases as a result of increased passive coefficient. By increasing ξ runout distances are increased from the initial isotropic value but are neither increased nor decreased as a result of an increased passive behavior. The effect of the passive coefficient when values of $\xi = 1500\, m/s^2$ result in decreased runout distances. The magnitude of the influence of the passive earth pressure coefficients seems unaffected by a change in the friction parameter μ. It is assumed that the runout is a result of the momentum of the flow.

As the debris flow reaches the runout zone, gravitational force greatly is reduced. As the passive earth pressure coefficient increases, the velocity going into the channel is decreased, as shown from the figures in the Appendix. A lower velocity going into the channel will result in a smaller momentum of the flow hitting the runout zone. An increased passive coefficient will however have a positive effect on the momentum of the flow resulting in a longer runout. This is because the increased coefficient leads to higher earth pressures in the runout. Why runout becomes smaller as a result of increased passive coefficients for the runout when ξ becomes larger is unsure. It could be discussed that an increase in ξ shows to result in higher velocities than for lower ξ values and may in such a way introduce more basal resistance through the turbulent friction term. However higher velocities will also lead to a positive effect on the momentum.

Active earth pressure coefficients show to increase runout distance as λ becomes smaller, if the friction coefficient μ is large enough. For $\mu = 0.05$ and $\mu = 0.08$, the runout distance is increased as a function of λ becoming smaller. The active coefficients are stated to be able to control the lateral spread, but when used in RAMMS they are also applied in the longitudinal direction simultaneously. The use of an active coefficient in the longitudinal direction does not represent the compressive motion happening in this direction.

The active and passive earth pressure coefficients both relate the stresses parallel to the slope in the flow to the given perpendicular stress developed as a function of the height of the flow. However, since the passive earth pressure coefficients are larger than the active earth pressure coefficients, the pressures mobilized by the passive coefficients are larger than the pressures mobilized by the active coefficient. The isotropic coefficient also produces stresses higher than the active coefficients. Hence, runout lengths should in theory become larger for the increased stresses occurring in the longitudinal direction of a debris flow. This does not seem to be as simple as first suggested.

The isotropic earth pressure coefficients result in the lowest runout distances in all of the simulations. The longer runout lengths of the active coefficients are produced as a result of the active coefficients in the Rankine theory becoming too small. Due to the lateral expansions with these coefficients, the runout hits the side walls. As a result of this, the flow continues to spread laterally in the runout zone until there is no more room to expand the flow. As the flow continues to spread even when hitting the side walls, the deposited material is pushed forwards along the edges and runout is increased as the confinement does not allow for greater lateral expansion. This is seen as an odd shape of the deposit in the results. With a higher value of the active coefficient such as provided

by the Savage and Hutter (1989) the lateral spread is more contained and debris flow does not hit the side walls or at least to a lesser extent. Another reason for the longer runout distance of the active state compared to the passive and isotropic is that this might happen due to numerical diffiusion associated with the RAMMS stopping criteria, since the stopping criteria is based on percentage of the total momentum. As flow is quite wide-spread due to the active earth pressure coefficient, it can continue to spread as flow hits side walls in runout, and the stopping criteria is never met. Velocities measured at x=-0.7 m in the channel are lower for both using active and passive earth pressure coefficients, than if λ is set to an isotropic value. A higher velocity going into the runout zone could hence not be the reason for a longer runout distance of the active state here.

However, the debris flow still travels slightly longer than the isotropic case when the flow is not interacting with the side walls as for the Savage and Hutter (1989) theory. The isotropic state produces higher stresses due to a higher earth pressure coefficient, however the active case that does not crash into the side walls still travels longer. A simple explanation for this could be due to the numerical instabilities associated with the active coefficient in the simulations, and that they do not occur for the isotropic coefficient. As simulation quality gets poorer with the use of the active pressure coefficient, the outline of the runout might be somewhat longer due to difficulties in defining the outer edges of runout.

The reason for a narrower spread in the beginning of the runout zone for the final deposition of the active coefficient compared to the passive, might be due to higher velocities obtained for the active coefficient compared to the passive state. Although velocities are reduced compared to the isotropic case for both active and passive coefficients, the active coefficients seem to have less of a reduction in velocities than passive. When velocities going into the runout zones are larger, the effect of the earth pressure coefficient is smaller. As flow velocities decreases, the effect becomes more dominant. Hence, the lower velocities in the passive case allow for a larger spread early in the runout zone, while the effect of the active coefficients requires reduction in velocities before the effects of active coefficients become dominant.

The narrower spread in the beginning of the runout zone for the final deposition of the active state compared to the isotropic can be explained by the deposition mechanism and runout distances. If one used an isotropic coefficient in the simulations, runout was shorter than for the active coefficient as described earlier. In the isotropic simulations the material for hence came to rest at an earlier point for the isotropic coefficient. The debris in the simulations is deposited first at the front and moves retrogressively towards the opening in the channel. The deposit hence moves closer to the channel as more material is deposited. In the isotropic state, the deposit reaches the channel opening before a large portion of the tail of the flow has settled. The material in the tail is hence laterally pushed outwards somewhat when hitting the deposit as the mass is much smaller than the already deposited debris. The deposit hence acts like a wall. In the active case, the debris flow travels longer before it is deposited allowing a greater space for the tail to deposit. Hence, less material is pushed out laterally. Debris flow runout length also is larger for the passive coefficient compared to the isotropic. However, the lateral spread is greater for the passive coefficients in the beginning of the runout zone as explained above. This might also be to a larger pressure in the longitudinal and lateral direction due to the increased earth pressure coefficient.

In the case of the runout hitting the end wall, a reason for the runout distances being too long, might be a result of a too high turbulence parameter ξ combined with a low friction parameter μ, which in this model resulted in a too large runout length. When total basal friction became too low a large amount of the released volume crashed into the end wall of the runout path. This splash of the runout volume onto the end wall, lead to trouble for the simulations to fulfill the end criteria for loss of percentage of momentum. It therefore took long time to fulfill the criteria as material needed to dissipate over the runout part.

When the slope is made less steep, changing the slope angle from a $30°$ slope to a $17.5°$ slope, runout distance becomes shorter and wider as a result of smaller gravity forces acting on the mass in the longitudinal slope direction. The change in runout shapes depending on the different earth pressure coefficients shows to be the same. When velocities are lower however, the effects of the earth pressure coefficients become somewhat larger.

This shows that the effect of the earth pressure coefficient not directly solves the problems with the large lateral spread in the runout when ξ is small. However, using a larger passive coefficient creates a more elongated shape compared to the active on both slope configurations. Also, when the turbulence friction becomes high, the runout becomes longer, and lateral spread is less for the different values of the earth pressure coefficient.

6.3 Froude number

The Froude numbers that are obtained in the numerical simulations are quite high. The large Froude numbers in small-scale experiments occur due to small flow heights while low friction in the models at the same time allows for velocities to obtain high values (Iverson, 1997b; Teetzmann & Shrestha, 2019; Vicari, 2018). This is also the case in the numerical simulations performed in RAMMS, as it simulates the small-scale experiments. The smaller flow heights in the small-scale flows produce less pore pressures which in theory should increase the Coulomb shear stress. Because of the smooth channel base however, the friction coefficient is low in these experiments.

The passive earth pressure coefficients λ produce a drop in the Froude number. The Froude number, however, does not change based on a further increase in the passive earth pressure coefficient. Active earth pressure coefficients also show decreasing values of the Froude number compare to the isotropic state. Even though the Froude number is reduced, the values are still well above the limit of the critical flow. However, a debris flow is expected to exhibit a higher value than for the critical flow due to its highly turbulent nature being consistent with a supercritical flow.

6.4 Parameter selection

Looking at which parameters should be used to simulate the behavior of the debris flow the results of the $30°$ slope are considered. Based on behavior in the runout, the active and passive coefficient did not present the correct elongated shape when values of the turbulence parameters were low. For higher values of the turbulence parameter, the runout became more elongated and showed less spread laterally. As a result, an increasing value of the passive and active coefficient, showed more of an elongation of the runout without making it much wider laterally. The passive coefficient showed the greatest effect.

For the back calculation of the results, the repetition of the reference test called E7-r4 is used to compare the numerical simulation results to the reference test. Runout distance shows to be around 303 cm for these tests and the shape can be seen from Figure 74. The best match of the behavior is considered for both the runout distance and the channel behavior. The effect of the passive and active earth pressure coefficient on runout shape is also considered.

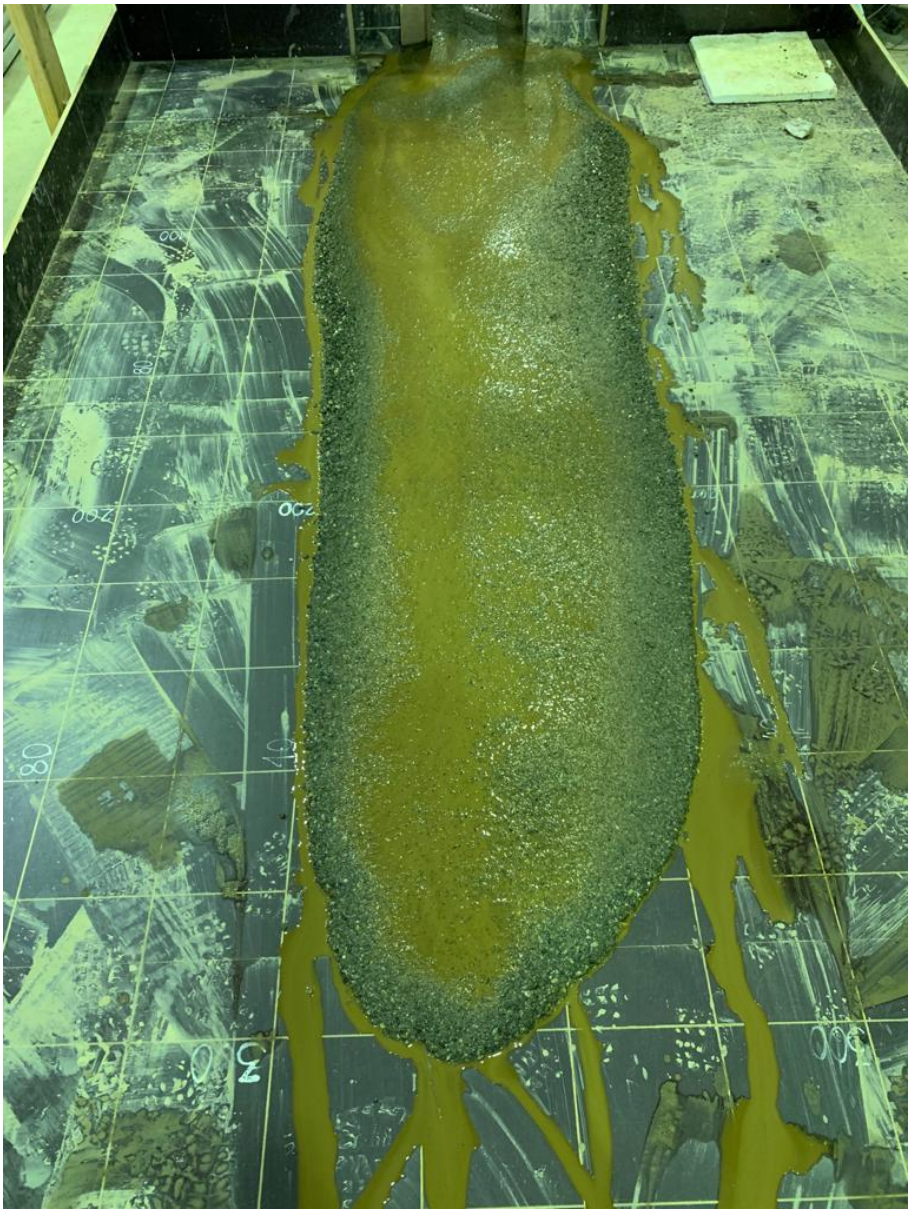

Figure 74 Runout of test E7-r4 in experiments of Teetzmann and Shrestha (2019).

Based on the final statements in the section describing the runout shapes, the elongated shape is obtained for the channel of $30°$ by setting a high value of the turbulence coefficient ξ. A high value of the turbulence friction coefficient, also shows to match the channel behavior well with the experiments of Teetzmann and Shrestha (2019). Comparing the results of the simulations using the different earth pressure coefficient values with the results from the reference test, it is obtained that values for channel behavior fit well with the reference case when $\mu = 0.05$ and $\mu = 0.08$, shown in Table 10 and Table 11.

From Table 10 and Table 11, it can be seen that the runout distances are less overpredicted when $\mu = 0.08$ compared with $\mu = 0.05$. Simulation results of the runout shape for both $\mu = 0.05$ and $\mu = 0.08$ can be seen from Figure 75 and Figure 76.

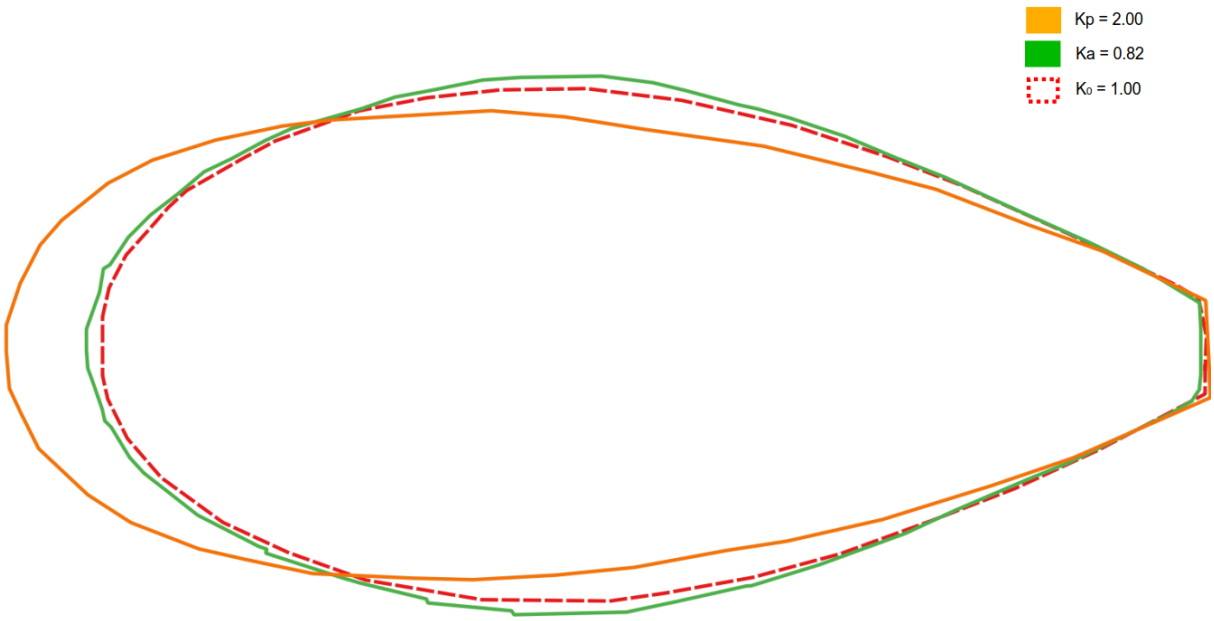

Figure 75 Runout shapes for the proposed earth pressure coefficients at $\mu = 0.05$.

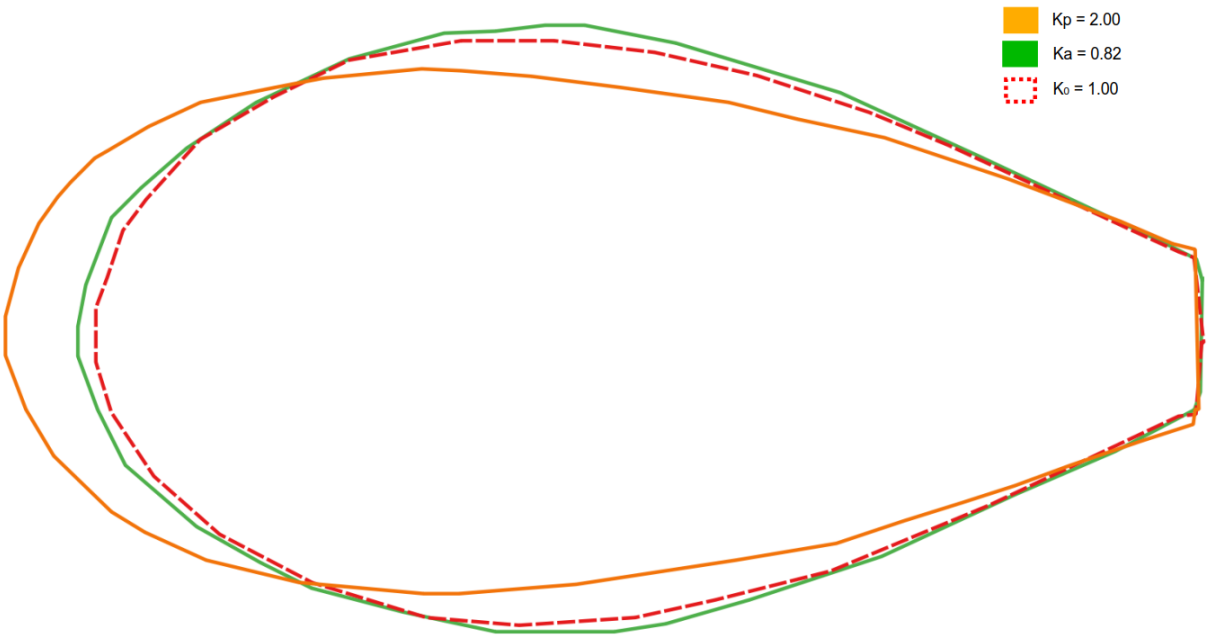

Figure 76 Runout shapes for the proposed earth pressure coefficients at $\mu = 0.08$.

The highest percentage of match for the channel behavior is found for the active and isotropic earth pressure coefficient in Table 10 and Table 11. Also, the runout distances are fitted best to the values of the reference test when the active earth pressure coefficient of $\lambda = 0.82$ is used for both $\mu = 0.05$ and $\mu = 0.08$. However, runout the elongated runout shapes are best represented by the passive coefficient $\lambda = 2.0$. This can be seen by comparing the figures of the simulations and picture of runout in E7-r4

above. Using a passive λ equal to 2.0 also shows good correlation between results in E7-r4 and simulation values in the channel. Based on both the channel behavior of the flow, and runout shape and distances, the best-fit behavior based on these simulations is found for $\mu = 0.08$ and $\xi = 1500\ m/s^2$ when $\lambda = 2.0$.

Table 10 Match of solution to reference case at x=-1.5 m

Voellmy parameters	**Earth pressure coefficient**	**% match in flow height**	**% match in velocity**	**%match in Fr**	**%match in runout distance**
$\boldsymbol{\mu = 0.05}$ $\boldsymbol{\xi = 1500\frac{m}{s^2}}$	$\lambda = 1.00$	103.00	103.50	100.81	156.80
	$\lambda = 0.82$	91.50	103.33	106.833	156.77
	$\lambda = 2.00$	132.00	100.28	86.32	161.72
$\boldsymbol{\mu = 0.08}$ $\boldsymbol{\xi = 1500\frac{m}{s^2}}$	$\lambda = 1.00$	106.00	100.35	96.39	123.76
	$\lambda = 0.82$	99.25	100.45	99.72	122.11
	$\lambda = 2.00$	116.50	97.17	89.03	132.01

Table 11 Match of solution to reference case at x=-1.1 m

Voellmy parameters	**Earth pressure coefficient**	**% match in flow height**	**% match in velocity**	**%match in Fr**	**%match in runout distance**
$\boldsymbol{\mu = 0.05}$ $\boldsymbol{\xi = 1500\frac{m}{s^2}}$	$\lambda = 1.00$	69.62	84.41	100.58	156.80
	$\lambda = 0.82$	62.31	83.20	104.80	156.77
	$\lambda = 2.00$	90.77	84.13	87.80	161.72
$\boldsymbol{\mu = 0.08}$ $\boldsymbol{\xi = 1500\frac{m}{s^2}}$	$\lambda = 1.00$	74.23	81.93	94.54	123.76
	$\lambda = 0.82$	71.92	82.80	97.07	122.11
	$\lambda = 2.00$	82.31	80.97	88.74	132.01

7 Conclusions

The main conclusions can be made based on the effect of the earth pressure coefficient on the runout of the debris flow. The effects of earth pressure coefficients on the lateral behavior in the channel is difficult to determine. The results in the runout zone provide a better basis for determining the effects of the active and passive earth pressure states in the flow.

A problem in RAMMS is that the earth pressure coefficient will not change depending on the motion being dilatational or compressional. The earth pressure coefficient remains constant throughout a simulation. Since RAMMS applies the earth pressure coefficient in the longitudinal and lateral direction simultaneously, the lateral and longitudinal behavior will both be prone to the same constant coefficient either active or passive, independent of the velocity gradient. Hence, the flow behavior will not be associated with the correct earth pressure coefficient over the entire flow.

Another issue with the earth pressure coefficient in RAMMS is that the flow behavior varies to a large extent when the earth pressure coefficient becomes active due to numerical instabilities. In addition, for some cases of the active earth pressure coefficient, numerical diffusion occurs in the runout zone when the flow hits either the end wall or the sidewalls. The numerical instabilities show to be less for the passive earth pressure coefficients, and the flow behavior varies less. It is a great concern is that the active coefficients show these large oscillations in the results, as it makes it harder to obtain good values.

Ideally, one wants to use a passive earth pressure coefficient on the compressional motion in the longitudinal direction and an active earth pressure coefficient for the dilatational behavior in the lateral direction of the runout zone. If one could have introduced the anisotropic stress state using different earth pressure coefficients in different directions based on the velocity gradient as proposed in Gray et al. (1999) and Pirulli (2005), it would have been possible to a larger extent to produce a desired shape of the runout. This could be done by controlling the spread in the lateral direction with an active coefficient while at the same time controlling the wanted compressive motion in the longitudinal direction by using a passive earth pressure coefficient. The use of another software could make this possible. It is seen through the simulations in RAMMS however, that the flow spread can to some extent be controlled by the simultaneous use of a constant active earth pressure coefficient longitudinally and laterally even though there occur some questions about the flow behavior. The passive coefficient can also increase the elongation of the runout. Lastly, the friction parameters of the Voellmy rheology need to be recalibrated for the use of the wanted earth pressure coefficient, to ensure that the numerical simulations model a best fit behavior.

Referanser

Bagnold, R. A. (1954). Experiments on a gravity-free dispersion of large solid spheres in a Newtonian fluid under shear. *Proceedings of the Royal Society of London. Series A. Mathematical and Physical Sciences*, *225*(1160), 49–63. https://doi.org/10.1098/rspa.1954.0186

Bagnold, R. A. (1966). The shearing and dilatation of dry sand and the 'singing' mechanism. *Proceedings of the Royal Society of London. Series A. Mathematical and Physical Sciences*, *295*(1442), 219–232. https://doi.org/10.1098/rspa.1966.0236

Bartelt, P., Bieler, C., Bühler, Y., Christen, M., Deubelbeiss, Y., Graf, C., McArdell, B. W., Salz, M., & Schneider, M. (2017). *Manual RAMMS - rapid mass movements simulation* (pp. 1–116).

Bartelt, P., Salm, B., & Gruber, U. (1999). Calculating dense-snow avalanche runout using a Voellmy-fluid model with active/passive longitudinal straining. *Journal of Glaciology*, *45*(150), 242–254. https://doi.org/10.3189/s002214300000174x

Berger, C., McArdell, B. W., & Schlunegger, F. (2011). Direct measurement of channel erosion by debris flows, Illgraben, Switzerland. *Journal of Geophysical Research: Earth Surface*, *116*(1), 1–18. https://doi.org/10.1029/2010JF001722

Christen, M., Kowalski, J., & Bartelt, P. (2010). RAMMS: Numerical simulation of dense snow avalanches in three-dimensional terrain. *Cold Regions Science and Technology*, *63*(1–2), 1–14. https://doi.org/10.1016/j.coldregions.2010.04.005

Christiansen, L. F. (2013). *Flomskred*.

Coe, J. A., Kinner, D. A., & Godt, J. W. (2008). Initiation conditions for debris flows generated by runoff at Chalk Cliffs, central Colorado. *Geomorphology*, *96*(3–4), 270–297. https://doi.org/10.1016/j.geomorph.2007.03.017

Crowe, C. T., Elger, D. F., Williams, B. C., & Roberson, J. A. (2009). *Engineering Fluid Mechanics*.

Cruden, D. M., & Varnes, D. J. (1996). Landslide types and processes. *Landslides: Investigation and Mitigation, Transportation Research Board Special Report 247, Washington D.C.*, *Bell 1992*, 36–75.

Davies, T. R. H. (1990). Debris-flow surges - experimental simulation. *Journal of Hydrology (N.Z.)*, *29*(1), 18–46.

Ellen, S. D., & Fleming, R. W. (1987). Mobilization of debris flows from soil slips, San Francisco Bay region, California. *Debris Flows/Avalanches: Process, Recognition, and Mitigation, Reviews in Engineeering Geology*, *7*, 31–35.

Fischer, J. T., Kowalski, J., & Pudasaini, S. P. (2012). Topographic curvature effects in applied avalanche modeling. *Cold Regions Science and Technology*, *74–75*, 21–30. https://doi.org/10.1016/j.coldregions.2012.01.005

Fiskum, E. (2012). *Flomskred Espen Fiskum*.

Gray, J. M. N. T., Wieland, M., & Hutter, K. (1999). *Gravity-driven free surface flow of granular*. *November*, 1841–1874. https://pdfs.semanticscholar.org/4802/b59b636ae74a03e819f32698054eac7dc519.pdf

Heller, P., & Jenssen, L. (2009). Modellforsøk med flomskred mot bruer. Virkning av bruåpning og ledevoller. *Teknologirapport Nr. 2582*, *2582*.

Hungr, O. (1995). A model for the runout analysis of rapid flow slides, debris flows, and avalanches. In *Canadian Geotechnical Journal* (Vol. 32, Issue 4, pp. 610–623). https://doi.org/10.1139/t95-063

Hungr, O., Evans, S. G., Bovis, M. J., & Hutchinson, J. N. (2001). A Review of the Classification of Landslides of the Flow type. *Environmental & Engineering Groscience*, *7*(3), 221–238.

Hungr, O., Leroueil, S., & Picarelli, L. (2014). The Varnes classification of landslide types, an update. *Landslides*, *11*(2), 167–194. https://doi.org/10.1007/s10346-013-0436-y

Hutter, K., Siegel, M., Savage, S. B., & Nohguchi, Y. (1993). Two-dimensional spreading of a granular avalanche down an inclined plane Part I. theory. *Acta Mechanica*, *100*(1–2), 37–68. https://doi.org/10.1007/BF01176861

Iverson, R. M. (1997a). Hydraulic modeling of unsteady debris-flow surges with solid-fluid interactions. *International Conference on Debris-Flow Hazards Mitigation: Mechanics, Prediction, and Assessment, Proceedings*, 550–561.

Iverson, R. M. (1997b). The Physics of Debris Flows. *Reviews of Geophysics*, *35*(3), 245–296. https://doi.org/10.1029/97RG00426;

Iverson, R. M., & Denlinger, R. P. (2001). *Flow of variably fluidized granular masses across three-dimensional terrain: 1. Coulomb mixture theory*. *106*, 537–552.

Iverson, R. M., & LaHusen, R. G. (1989). Dynamic Pore-Pressure Fluctuations in Rapidly Shearing Granular Materials. *Science*, *246*(4931), 796–799. http://www.jstor.org/stable/1704725

Iverson, R. M., & LaHusen, R. G. (1993). Friction in debris flows: inferences from large-scale flume experiments. *Proceedings - National Conference on Hydraulic Engineering*, *pt 2*, 1604–1609.

Iverson, R. M., Reid, M. E., & Lahusen, R. G. (1997). Debris-flow mobilization from lanslides. *Annual Review of Earth and Planetary Sciences*, *25*, 85–138. https://doi.org/https://doi.org/10.1146/annurev.earth.25.1.85

Jakob, M., & Hungr, O. (2005). Debris flow hazards and Related phenomena. In *Journal of Chemical Information and Modeling* (Vol. 53, Issue 9). https://doi.org/10.1017/CBO9781107415324.004

Koo, R. C. H., Kwan, J. S. H., Ng, C. W. W., Lam, C., Choi, C. E., Song, D., & Pun, W. K. (2017). Velocity attenuation of debris flows and a new momentum-based load model for rigid barriers. *Landslides*, *14*(2), 617–629. https://doi.org/10.1007/s10346-016-0715-5

Kwan, J. S. H., Koo, R. C. H., & Ng, C. W. W. (2015). Landslide mobility analysis for design of multiple debris-resisting barriers. *Canadian Geotechnical Journal*, *52*(9), 1345–1359. https://doi.org/10.1139/cgj-2014-0152

Laache, E. (2016). *Model Testing of the Drainage Screen Type Debris Flow Breaker*. *June*.

Major, J. J. (1997). Depositional Processes in Large-Scale Debris-Flow Experiments. *The Journal of Geology*, *105*(3), 345–366. http://www.jstor.org/stable/10.1086/515930

Major, J. J., & Pierson, T. C. (1992). Debris Flow Rheology ' Experimental Analysis of Fine-Grained Slurries Any rotating of fI imposed on the rotor [Van Wazer and mat . he . matical models of deb . ris flows have ! n length to the. *Water Resources*, *28*(3), 841–857.

McDougall, S., & Hungr, O. (2005). Dynamic modelling of entrainment in rapid landslides. *Canadian Geotechnical Journal*, *42*(5), 1437–1448. https://doi.org/10.1139/t05-064

Meyer, G. A., & Wells, S. G. (1997). Fire-related sedimentation events on alluvial fans, Yellowstone National Park, U.S.A. *Journal of Sedimentary Research*, *67*(5), 776–791. https://doi.org/10.1306/D426863A-2B26-11D7-8648000102C1865D

Mitchell, J. K., & Soga, K. (1994). Fundamentals of Soil Behavior. In *Soil Science* (Third, Vol. 158, Issue 1). John Wiley & Sons, Inc. https://doi.org/10.1097/00010694-199407000-00009

Ng, C. W. W., Choi, C. E., Koo, R. C. H., Goodwin, G. R., Song, D., & Kwan, J. S. H. (2018). Dry granular flow interaction with dual-barrier systems. *Geotechnique*, *68*(5), 386–399. https://doi.org/10.1680/jgeot.16.P.273

Ng, C. W. W., Choi, C. E., Majeed, U., Poudyal, S., & De Silva, W. A. R. K. (2019). Fundamental framework to design multiple rigid barriers for resisting debris flows. *Procds. of 16th Asian Regional Conference on Soil Mechanics and Geotechnical Engineering, October 14-18, 2019, Taipei, Taiwan*, 1–11.

NVE. (n.d.). *NVE Aktsomhetskart for jord- og flomskred*. Retrieved March 16, 2020, from https://gis3.nve.no/link/?link=jordflomskredaktsomhet

Pierson, T. C. (1986). Flow behavior of channelized debris flows, Mount St. Helens, Washington. In A. D. Abrahams (Ed.), *Hillslope processes* (pp. 269–296). Allen & Unwin.

Pierson, T. C., & Costa, J. E. (1987). A rhéologie classification of subaerial sediment-water flows. *GSA Reviews in Engineering Geology*, *7*(January 1987), 1–12. https://doi.org/10.1130/REG7-p1

Pirulli, M. (2005). Numerical Modelling of Landslides Runout. A continuum mechanics approach. *PhD Thesis*.

Pradhan, R. N. (2017). *Physical Modeling of Debris Flow by Varying Sediment Concentration* (Issue June). https://brage.bibsys.no/xmlui/handle/11250/2458154

Proske, D., Suda, J., & Hübl, J. (2011). Debris flow impact estimation for breakers. *Georisk*, *5*(2), 143–155. https://doi.org/10.1080/17499518.2010.516227

Quan, B. R. (2012). Dynamic numerical run out modeling for quantitative landslide risk assessment. In *Thesis of University of Twente, ITC*. http://www.academia.edu/download/31071636/quan.pdf

Salm, B. (1993). Flow, flow transition and runout distances of flowing avalanches. *Annals of Glaciology*, *18*, 221–226. https://doi.org/10.3189/s0260305500011551

Sassa, K. (1985). *The mechanism of debris flow*. 1173–1176.

Savage, S. B., & Hutter, K. (1989). The motion of a finite mass of granular material down a rough incline. *Journal of Fluid Mechanics*, *199*(2697), 177–215. https://doi.org/10.1017/S0022112089000340

Scheidl, C., Chiari, M., Kaitna, R., Müllegger, M., Krawtschuk, A., Zimmermann, T., & Proske, D. (2013). Analysing Debris-Flow Impact Models, Based on a Small Scale Modelling Approach. *Surveys in Geophysics*, *34*(1), 121–140. https://doi.org/10.1007/s10712-012-9199-6

Schraml, K., Thomschitz, B., McArdell, B. W., Graf, C., & Kaitna, R. (2015). Modeling debris-flow runout patterns on two alpine fans with different dynamic simulation models. *Natural Hazards and Earth System Sciences*, *15*(7), 1483–1492. https://doi.org/10.5194/nhess-15-1483-2015

Skempton, A. W. (1964). Long-Term Stability of Clay Slopes. *Géotechnique*, *14*(2), 77–102. https://doi.org/10.1680/geot.1964.14.2.77

Takahashi, T. (2007). *Debris Flow: Mechanics, Prediction and Countermeasures*. Taylor & Francis Group.

Teetzmann, A., & Shrestha, S. (2019). *Physical modeling of debris flow and entrainment of bed sediments*. *December*.

Varnes, D. (1978). Slope Movement Types and Processes. *Transportation Research Board Special Report*, *176*.

Vicari, H. (2018). *Physical and numerical modelling of debris flows*.

Voellmy, A. (1955). Über die Zerstörungskraft von Lawinen. *Schweizerische Bauzeitung*, *73*(12), 159–165.

Wendeler, C. (2016). *Debris-Flow Protection Systems for Mountain Torrents*. 267.

Yifru, A. L. (2014). *Assessment of Rheological Models for Run-out Distance Modeling of Sensitive Clay Slides, Focusing on Voellmy*. 130.

Yifru, A. L., Laache, E., Norem, H. A., Nordal, S., & Thakur, V. K. S. (2018). *Laboratory investigation of performance of a screen type debris-flow countermeasure*.

8 Appendix

8.1 Flow heights at x=-0.7 m

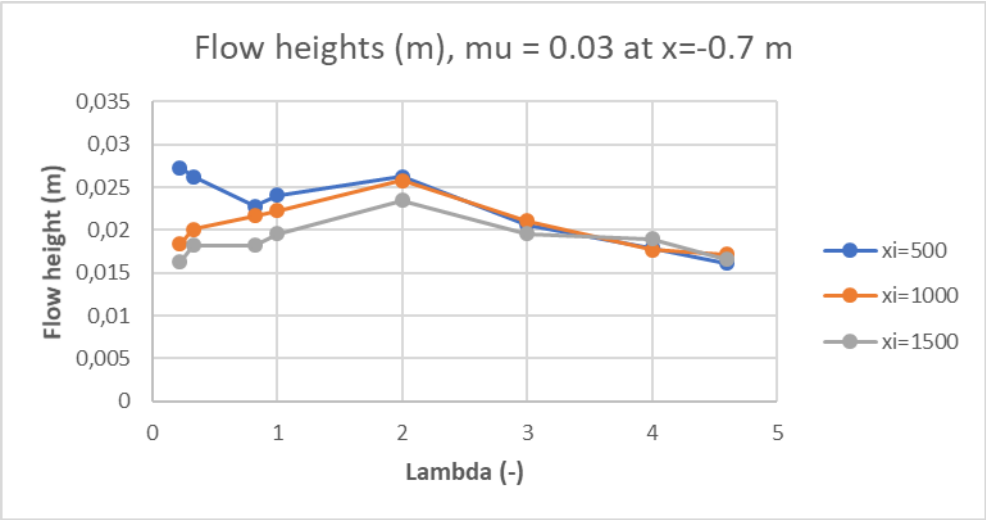

Figure 77 Flow heights at x=-0.7 m, when $\mu = 0.03$ and ξ varies.

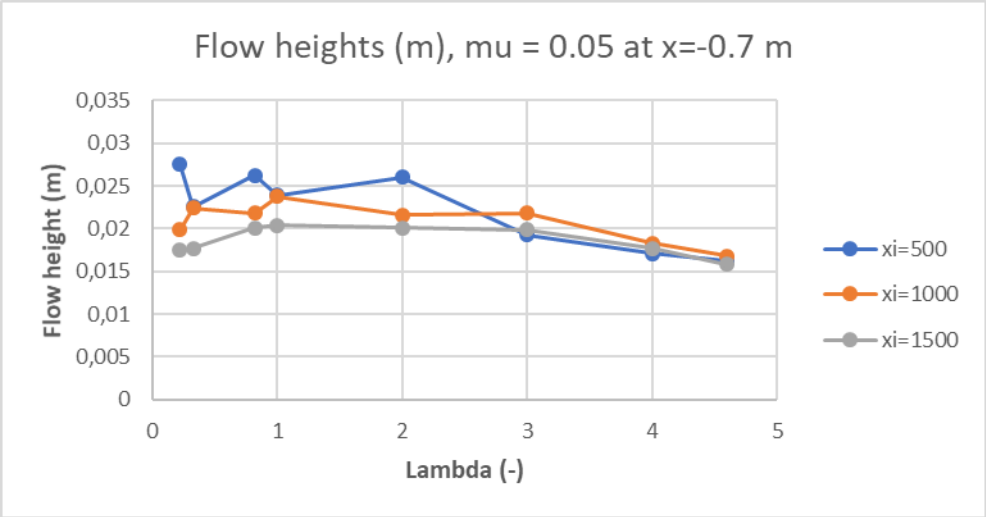

Figure 78 Flow heights at x=-0.7 m, when $\mu = 0.05$ and ξ varies.

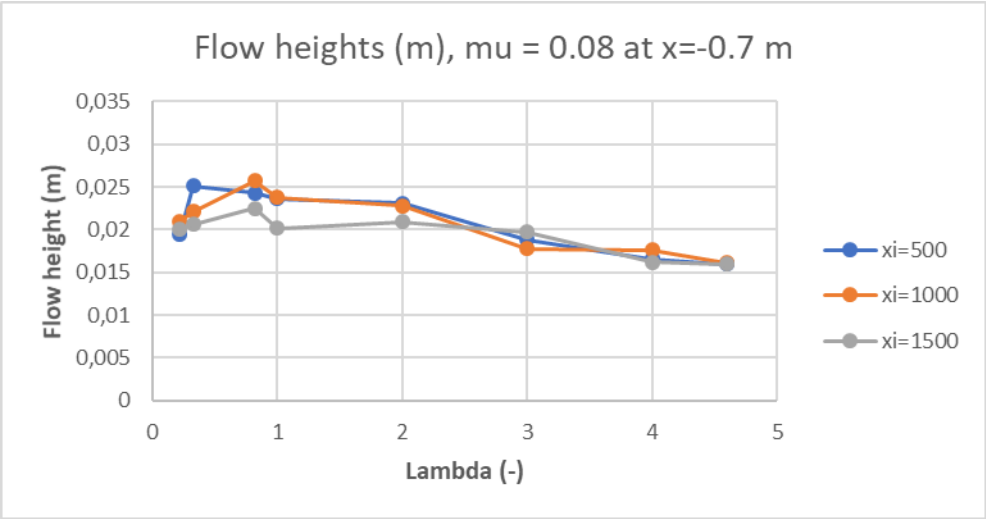

Figure 79 Flow heights at x=-0.7 m, when $\mu = 0.08$ and ξ varies.

8.2 Velocities at x=-0.7 m

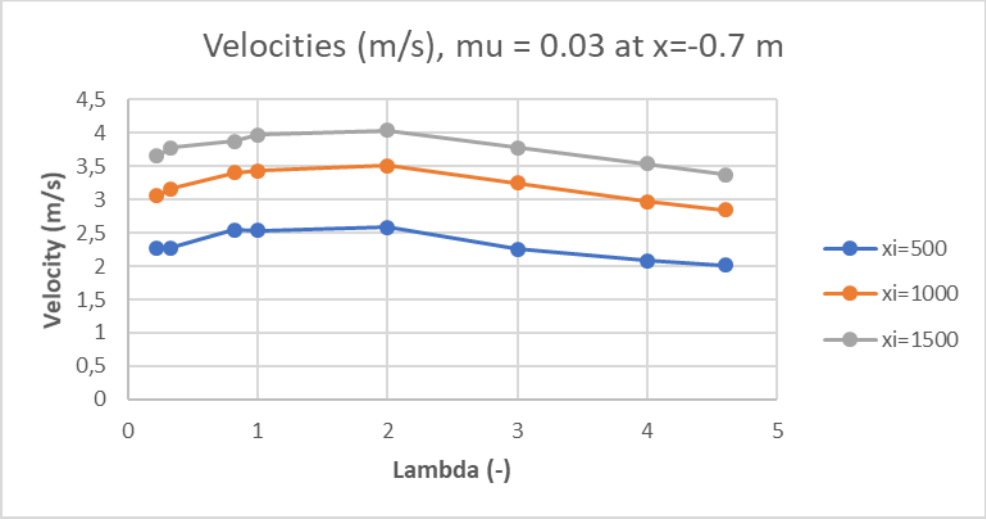

Figure 80 Velocities at x=-0.7 m, when $\mu = 0.03$ and ξ varies.

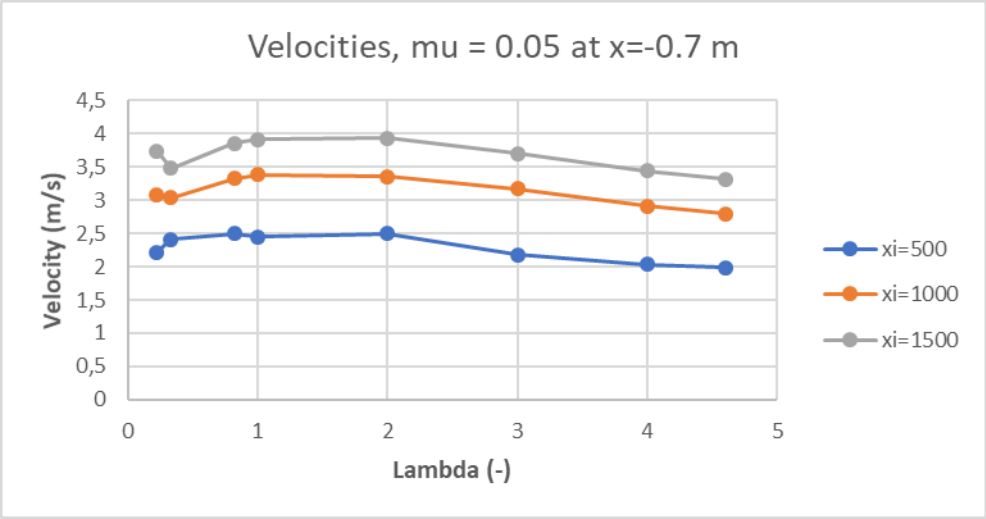

Figure 81 Velocities at x=-0.7 m, when $\mu = 0.05$ and ξ varies.

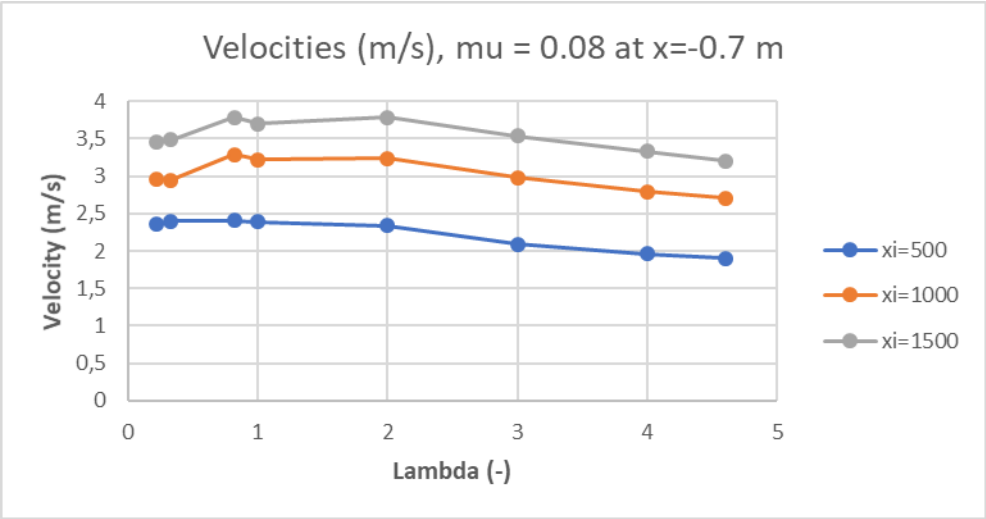

Figure 82 Velocities at x=-0.7 m, when $\mu = 0.08$ and ξ varies.

8.3 Runout shapes for $\xi = 1500\ m/s^2$

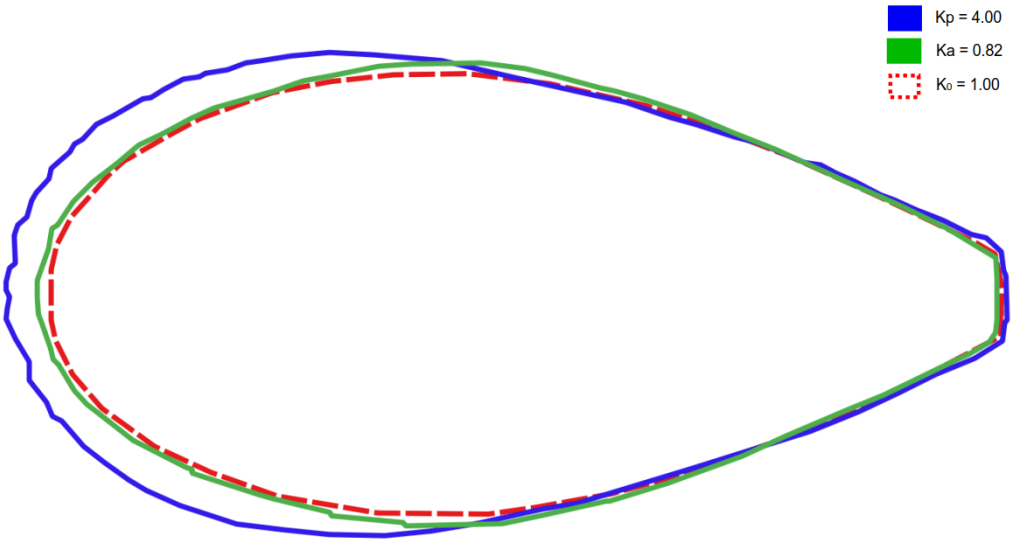

Figure 83 Runout for approach 1 with Savage and Hutter theory (1989) *when $\mu = 0.05$ and $\xi = 1500\ m/s^2$ on a $30°$ slope.*

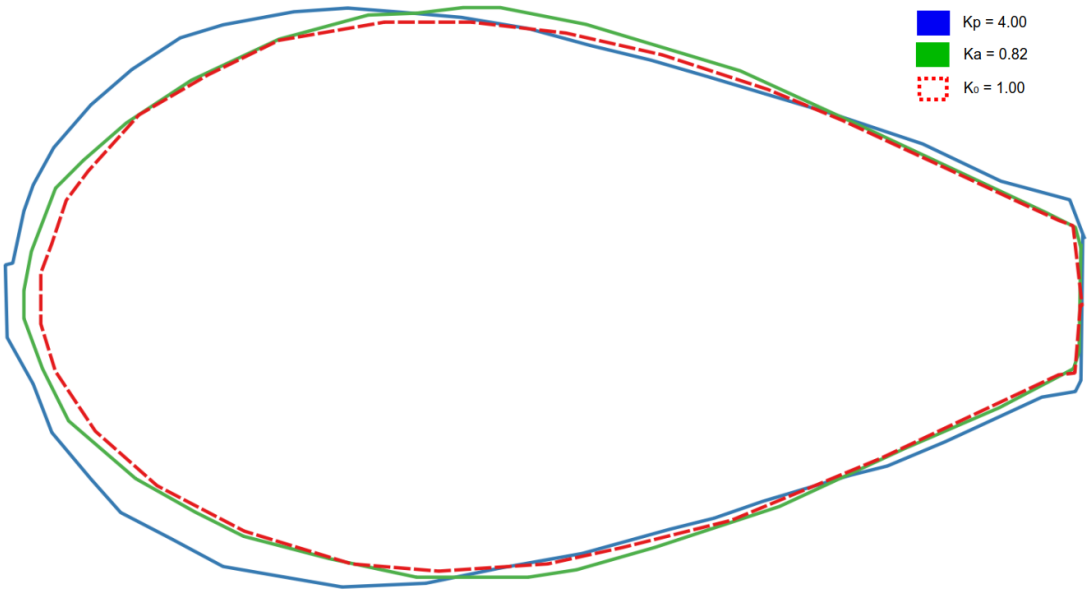

Figure 84 Runout for approach 1 with Savage and Hutter theory (1989) *when* $\mu = 0.08$ *and* $\xi = 1500\, m/s^2$ *on a* $30°$ *slope.*